

AD-A206 946

REPORT DOCUMENTATION PAGE

1. SECURITY CLASSIFICATION AUTHORITY & DATE 1989			10. RESTRICTIVE MARKINGS		
2. DECLASSIFICATION/CONTROLLING SCHEDULE			3. DISTRIBUTION/AVAILABILITY OF REPORT Approved for public release; distribution is unlimited		
4. PERFORMING ORGANIZATION REPORT NUMBER(S)			5. MONITORING ORGANIZATION REPORT NUMBER(S) AFOSR-TR-89-0406		
6a. NAME OF PERFORMING ORGANIZATION Princeton University		6b. OFFICE SYMBOL (If applicable)	7a. NAME OF MONITORING ORGANIZATION AFOSR/NA		
6c. ADDRESS (City, State and ZIP Code) Dept. of Mech. & Aero Eng Princeton, NJ 08544			7b. ADDRESS (City, State and ZIP Code) Building 410, Bolling AFB, DC 20332-6448		
8a. NAME OF FUNDING/SPONSORING ORGANIZATION AFOSR/NA		8b. OFFICE SYMBOL (If applicable) NA	9. PROCUREMENT INSTRUMENT IDENTIFICATION NUMBER AFOSR 86-00J3		
6c. ADDRESS (City, State and ZIP Code) Building 410, Bolling AFB, DC 20332-6448			10. SOURCE OF FUNDING NOS.		
			PROGRAM ELEMENT NO. 61102F	PROJECT NO. 2308	TASK NO. A2
11. TITLE (Include Security Classification) Charged Slurry Droplet Research					
12. PERSONAL AUTHOR(S) A.J. Kelly					
13a. TYPE OF REPORT Final		13b. TIME COVERED FROM 1/10/86 TO 30/9/88		14. DATE OF REPORT (Yr., Mo., Day) 1989 Feb 20	
15. PAGE COUNT 198					
16. SUPPLEMENTARY NOTATION					
17. DECATI CODES			18. SUBJECT TERMS (Continue on reverse if necessary and identify by block number)		
FIELD	GROUP	SUB. GR.	Charged Droplets, Charged Sprays, Rayleigh Bursting, Droplet Levitation, Droplet Charging Behavior, Quadrupole Mass Spectrometer.		
21	01				
21	02				
19. ABSTRACT (Continue on reverse if necessary and identify by block number) Rayleigh Bursting, wherein critically charged droplets explosively expel a number of micron sized "sibling" droplets, enhances atomization and combustion of all liquid fuels. Droplet surface charge is retained during evaporation, permitting multiple Rayleigh Bursts to occur. Moreover, the charge is available for the deagglomeration of residual particulate flocs from slurry droplet evaporation. To fill gaps in our knowledge of these processes, an experimental program involving the use of a charged droplet levitator and a quadrupole mass spectrometer, high speed electrometer (QMS/HSE) has been undertaken to observe the disruption and to measure quantitatively the debris. A charged droplet levitator based on a new video "frame grabber" technology to image transient events, is described. Sibling droplet size is ten microns or less and is close to, if not coincident with, the predicted phase transition in droplet charging level. The research effort has focused on the explanation of this transition and its implications. Octoil droplet charge and mass data, spanning a thirty fold range in the charge to mass ratio interval centered on the predicted					
20. DISTRIBUTION/AVAILABILITY OF ABSTRACT UNCLASSIFIED UNLIMITED <input checked="" type="checkbox"/> SAME AS RPT. <input checked="" type="checkbox"/> DTIC USERS <input checked="" type="checkbox"/>			21. ABSTRACT SECURITY CLASSIFICATION Unclassified		
22a. NAME OF RESPONSIBLE INDIVIDUAL Dr. J.M. Tishko			22b. TELEPHONE NUMBER (Include Area Code) (202) 767-0465		22c. OFFICE SYMBOL AFOSR/NA

DD FORM 1473, 83 APR

EDITION OF 1 JAN 73 IS OBSOLETE.

Unclassified
SECURITY CLASSIFICATION OF THIS PAGE

89

4

12

041

19. cont.

phase transition, verifies the existence of discontinuous behavior. In particular, the limiting droplet surface electric field (the emission limit) is found to differ by a factor of $5/3 \pm 8\%$ across the transition, with the charging distribution for droplets smaller than the transition having the higher limit and lower charge level. Droplets larger than the transition have a relative dielectric constant 2.1 ± 0.1 times that of the smaller droplet population and a minimum emission limit of 4.2 GV/m. The data are consistent with condensation of the surface electrons from a plasma state to a rigid electron "crystal" as the droplet size is increased through the transition. Electron crystallization is concluded to dominate both the Rayleigh Bursting process and electrostatic spraying.

Accession For	
NTIS GRA&I	<input checked="checked" type="checkbox"/>
DTIC TAB	<input type="checkbox"/>
Unannounced	<input type="checkbox"/>
Justification	
By _____	
Distribution/	
Availability Codes	
Dist	Avail and/or Special
A-1	



AFOSR-IR. 89-0406

MAE 1855

Final Report

CHARGED SLURRY DROPLET RESEARCH

AFOSR-86-0013

A. J. KELLY

School of Engineering and Applied Science
Department of Mechanical and Aerospace Engineering
Princeton University
Princeton, NJ 08544

FINAL REPORT
Charged Slurry Droplet Research
AFOSR-86-0013

Introduction —

The behavior of charged and uncharged sprays are markedly different. The unique characteristics of charged sprays, which provide options not available from conventional atomization, recommend their consideration for combustion systems involving difficult to atomize and burn fuels, such as the high solid content slurries of current interest.

All of the distinctive characteristics of charged sprays are directly traceable to the presence of free charge on the individual droplet surface. The fact that each droplet is unipolarly charged means that droplet dispersal will automatically occur, even under the most demanding fluid mechanical conditions. As a consequence, these sprays are inherently homogeneous and less susceptible to the formation of fuel rich striations. Moreover, droplet agglomeration will be suppressed or eliminated. Beyond these important attributes the presence of free charge on the droplet surface yields other advantages that cannot be offered by uncharged sprays. Two of these advantages involve the unique manner in which a charged droplet undergoes evaporation.

It is now well established [1-5] that droplet surface charge level will be uninfluenced by evaporation. In fact, all evidence shows that the charge is tenaciously bound to the surface and will not be released no matter how vigorous the evaporation. This is true for all conditions below the critical charging level, the so-called Rayleigh Limit [6] of droplet charging. As evaporation proceeds, and surface charge is conserved on a diminished surface, the stabilizing surface tension force is inexorably overtaken by the monotonically increasing, outwardly directed and repulsive electrostatic force. Although the charge induced force makes the droplet more susceptible to aerodynamic shattering than it ordinarily would be [7], even in the absence of motion, a critical condition is reached wherein the electrostatic and surface tension forces come into balance and the droplet becomes unstable.

What little is known concerning the subsequent behavior of the droplet is consistent with the explosive expulsion of several highly charged "sibling" droplets having a diameter of the order of ten microns. As a result of this "Rayleigh Bursting" process the "parent" droplet behaves like an insitu atomizer that is capable of repeatedly undergoing cycles of evaporation and bursting and thereby seeding the spray volume with vigorously dispersing

siblings. It should be noted that the siblings also undergo this forced fragmentation further adding to the mixing and dispersal process [1].

As charged slurry fuel droplets participate in this episodic bursting, a point is reached where the free surface charge will "plate out" on the residue of evaporatively dried particulates and provide a mechanism for deagglomeration. To the extent that neutralizing ions from the combustion zone fail to penetrate the outwardly streaming and insulating vapor cloud surrounding the evaporating and shattering droplet, the free charge is potentially capable of completely dispersing the slurry droplet and making it accessible for combustion. It is this promise of enhanced atomization and combustion that has provided the stimulus for the three year research program summarized in this report.

The Research Effort -

Rayleigh Bursting of charged droplets and the electrostatic deagglomeration of micron sized particulate flocculi are fundamental processes that are inadequately documented, poorly understood and are commonly accepted to involve the rapid dispersal of small (1 to 10 μ m) charged entities. This lack of fundamental knowledge can be placed in perspective by the realization that while there is little experimental or theoretical information concerning the episodic Rayleigh Bursting phenomena, and then only for rheologically simple Newtonian [8-11] fluids (no work has been undertaken on high solid contents liquids), nothing is known concerning the deagglomeration process. No quantitative data exist concerning the most elemental features of either of these processes. In fact, even for the more extensively studied Rayleigh Bursting process, the temporal development of the disruption, the number of particles generated and their mass, charge, velocity, spatial distribution and timing have yet to be observed. This research effort was specifically directed toward filling in gaps in our knowledge of these phenomena and thereby to provide insights into the larger concern of whether charged sprays and the use of electrostatic atomization can benefit slurry fuel combustion.

Overview -

In the absence of available diagnostic tools that are capable of making the types of measurements indicated, the research program has been concerned with the development and validation of the necessary instrumentation. This effort has involved the development of two new research instruments: a levitated droplet apparatus for imaging the disruption of isolated droplets/agglomerates and a high mass (10^{14} AMU) quadrupole mass spectrometer/high speed electrometer (QMS/HSE) to measure both the charge and the mass of the post disruption debris. These instruments are designed specifically to probe

the behavior of rheologically complex charged slurry fluids, provide essential insight into electrostatic particulate deagglomeration and to bolster our meager knowledge of charged fluid droplet dynamics.

Both the charged droplet levitator and the quadrupole mass spectrometer/high speed electrometer have been designed to be used individually or as a combined experiment. The charged droplet levitator, a modern version of the Millikan oil droplet experiment is capable of suspending single charged droplets to make them accessible for prolonged observation. By using active feedback control in conjunction with a precision optical imaging system, the evaporating droplet can be held stationary in the optical field of view by appropriate manipulation of the levitating electrode voltages. Although the optical system is used for the detailed control of the suspended droplet, its primary function is to image the breakup (bursting) and deagglomeration processes as they occur. Because these processes are estimated to occur on microsecond to millisecond time scales, which are orders of magnitude shorter than those required for levitation, it has been necessary to design the system to have comparable response characteristics. Consequently, considerable effort has been devoted to this aspect of the imaging system design. For convenience, the initial levitator experiment was designed to operate at atmospheric conditions. While this mode of operation will permit imaging of the disruption process and will permit additional data concerning the Rayleigh Limit to be collected, it is only when the levitator is used in conjunction with the QMS/HSE instrument operating at high vacuum that quantitative data concerning the Rayleigh Bursting and deagglomeration debris will be obtained.

As the primary instrument for the measurement of particle charge and mass, the development of the QMS/HSE has been the major focus of this effort. One of the most challenging aspects of this work has been the calibration of this instrument. Conventional quadrupole mass spectrometer devices designed for use in the 1 to 1000AMU can be calibrated using well characterized chemical species. Despite the comforting agreement between the theoretical and observed behavior of these instruments there is no guarantee that the device we fabricated would also exhibit predictable behavior when dealing with droplets and particulates in the 10^{14} AMU range. The disparity in mass and in charge to mass ratio is simply too large to warrant extrapolation. The substantial effort required to validate QMS/HSE operation at the extreme mass range associated with 10 micron sized particulates has been well rewarded by the fundamental insight this has provided into the behavior of charged droplets. This effort is summarized after first a discussion of the levitator work is presented.

Charged Droplet Levitator -

The charged droplet levitator apparatus depicted in the schematic of Figure 1 has been specifically designed to provide direct quantitative information concerning the behavior preceding disruption and a quantitative measure of the number of siblings produced. This apparatus, an extensively refined variant of the design first described by Rhim, et al. [11,12], is described fully in the research thesis in Appendix A. This document should be consulted for details of construction and operation.

As shown in the schematic a Compaq 386 computer is used to control all functions of the droplet levitation and manipulation processes. During operation, the Compaq computer issues a launch command to form and to elevate electrostatically a charged droplet from the capillary source that is centrally located within the lower electrode. Tap water, selected for convenience for all testing, is sufficiently conductive that the application of an appropriate voltage on the upper electrode will induce sufficient free charge to flow to the fluid at the tip of the grounded capillary to produce a charged droplet.

Rhim has demonstrated that the most important prerequisite for successful droplet formation and subsequent projection with the interelectrode, observation area is the form of the voltage (electric field) profile. The most reliable profile involves a rapid rise to an elevated voltage which is maintained for sufficient time for the droplet to form and detach from the capillary tip. Once free, the droplet is then subjected to a diminished electric field of sufficient magnitude to continue the upward trajectory but of insufficient strength to further accelerate the droplet and have it collide with the upper electrode. The computer then issues a command for a sharply defined retarding voltage pulse to be applied to the lower electrode. This serves to decelerate the droplet and to bring it within the field of view of the CCD camera optics that will then serve to provide position and velocity information for further control of the droplet position. As discussed in the appendix, the high speed, high voltage electrode voltage supplies are the most essential element of this first phase of the levitation process.

Once droplet stabilization has been achieved, the droplet is now maintained within the field of view of the CCD optics. During this "observation phase" the full capability of a real time "frame grabber" system is used. This function is performed by the Pyramid Tracker computer, a proprietary development of the GE/SRI David Sarnoff Laboratories [13,14]. The Pyramid Tracker is specifically designed to automatically analyze visual data from the CCD camera at any of six resolution levels ranging from level 1, the crudest and most easily and hence most rapidly processed image of 7×8 pixels, to the maximum resolution of the full 240×250 pixel image of level 6. By automatically adjusting the image resolution, the Pyramid Tracker can rapidly process the visual data to generate droplet

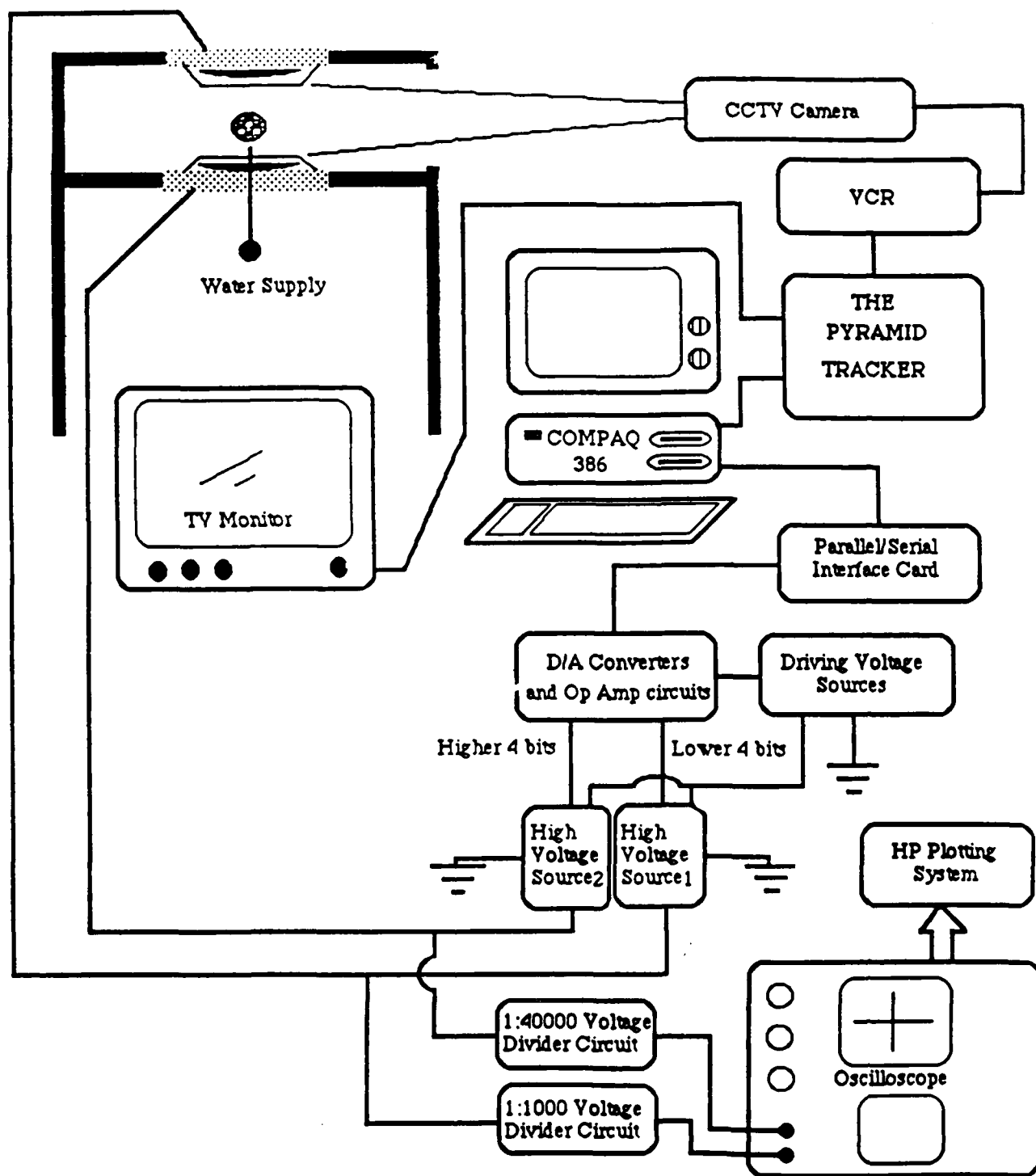


Figure 1: System Block Diagram

position control signals. This is typically accomplished using low resolution level 1 imaging. Once stabilized, the droplet/agglomerate is then imaged at level 6 in anticipation of the disruption process. In this way it is possible to use the same system to position the particle and to capture the disruption process. All of the necessary software has been written and all of the D/A interface electronics for levitation are now operational.

In a yet to be published paper, Elghazaly and Castle [15] describe the results of a droplet bursting study in which the charged droplet is immobilized or "tethered" at the end of a string. There are several reasons that recommended the use of this technique for the initial validation testing of the Pyramid Tracker system. First, the use of an immobilized droplet permits the Pyramid Tracker system to be tested independent of the dynamic levitator unit. Secondly, while the limited data on droplet description provided by this method do agree with Elghazaly's model, the data base is too sparse to establish the general validity of the model. Finally, if the Pyramid Tracker data demonstrates that the technique does permit a tethered droplet to Rayleigh burst in the same manner as a truly isolated levitated droplet, it would be far simpler to use with the QMS/HSE than the levitator, where the test droplet has to be remotely manipulated under high vacuum conditions.

Accordingly the tethered droplet experiment was implemented and tests were undertaken with the Pyramid Tracker. In these tests a water droplet is extruded from a $300\mu\text{m}$ OD, $250\mu\text{m}$ ID hypodermic tube sting, which served not only as a conduit for replenishment of the test fluid but also as the charging electrode. In all instances the charging voltage was adjusted to be within the range defined by Elghazaly [15] as being required for bursting rather than spraying or dripping to occur. As a result of these tests, a sample of which is included as Figure 2, the following conclusions have been drawn.

1. The Pyramid Tracker computer/optics system is capable of consistently sensing droplet breakup and can track the siblings as they are energetically repelled from the parent.
2. The sampling frequency of the Pyramid tracker is adequate for preliminary validation testing but will have to be improved by a factor of at least two if quantitative imaging of the bursting process is to be obtained.
3. The observed droplet breakup pattern is consistent with the results obtained by Elgazhaly. The sampling limitations imposed by the Pyramid Tracker system do not permit a more detailed validation to be made at this time. Nevertheless, bursting and sibling expulsion do occur and have been observed.

This graph represents data obtained for 50 bursts. The pulse used in these bursts had a magnitude of 14kV, a duration of 60ms and a transient time of 12ms.

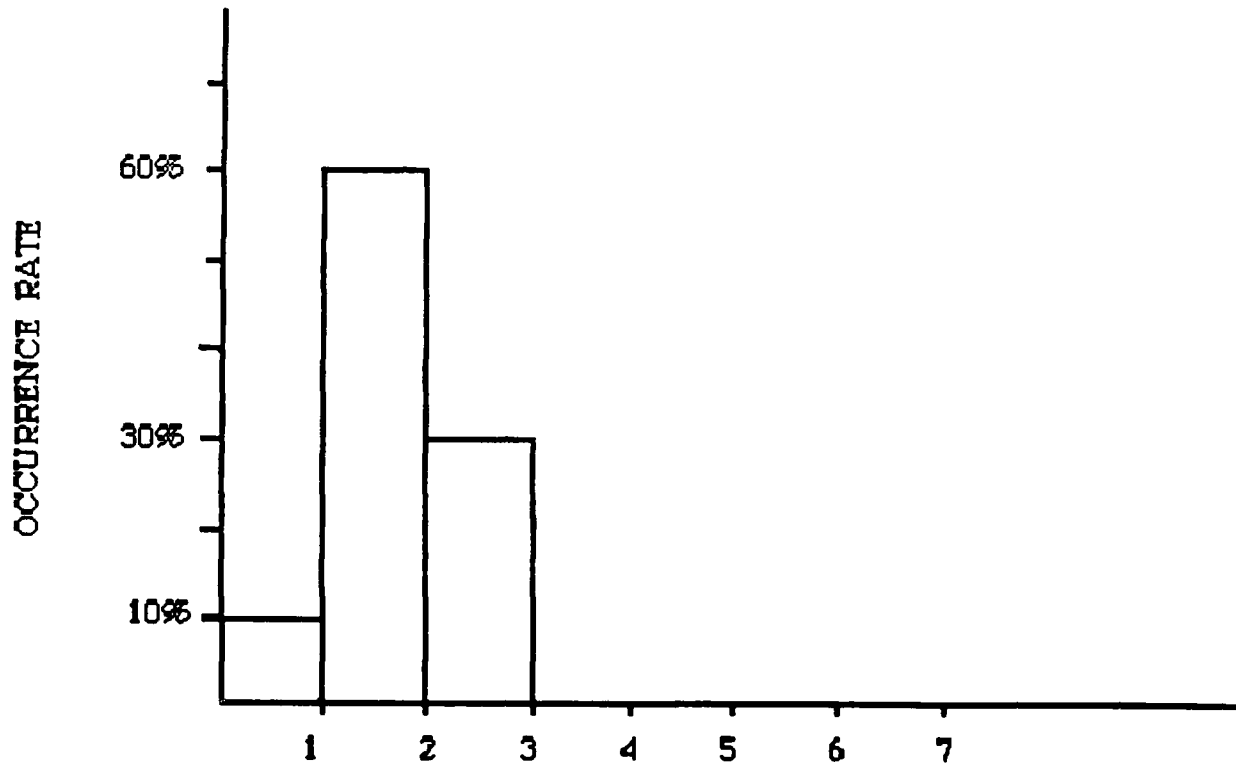


Figure 2: NUMBER OF DROPLETS PER BURST

**DISTRIBUTION OF THE NUMBER OF DROPLETS
FORMED IN RESPONSE TO A PULSE**

The inherent simplicity of the tethered droplet technique, as compared to the levitator systems led to the decision to focus on the use of this method rather than the levitator with the QMS/HSE instrument. This decision permitted us to focus our attention on the development of the QMS/HSE instrument.

Quadrupole Mass Spectrometer/High Speed Electrometer –

Accordingly, the primary focus of our activity has been the development of a Quadrupole Mass Spectrometer/High Speed Electrometer that is capable of independently measuring the charge to mass ratio and the charge of individual droplets and particulates in the size range of interest (order of ten microns). Figure 3 is a schematic of the instrument we have built and which is fully described in the thesis of Appendix B. While the schematic depicts the droplet source as a diode sprayer, the device was designed to be coupled with the droplet levitator and with the tethered droplet rig of Elghazaly. As described in the appendix, which should be consulted for technical detail, the device has been designed to filter droplets having charge to mass ratios in the 0.01 to 100C/kg (10 to 10^5C/m^3) range. However, limitations imposed by the availability of appropriate high voltage transformers effectively restricted the charge to mass capability to ~ 0.1 to $\sim 3 \text{C/kg}$, corresponding to the droplet size range of most interest. Commercially available Amptek charge detectors and amplifiers provide a maximum charge sensitivity of 280 electrons.

Droplets or particulates having charge to mass ratios within the bandwidth of the QMS, which typically is set at 3 to 5% of the preselected value in the range noted, will pass to a collector plate where their charge is transferred for measurement. As will be noted, particular attention had to be devoted to the charge collection process to assure that all droplet charge is drained to the amplifier circuit within the response time of the detector. Once collected, the amplifier generates an output signal that is proportional to the charge collected. It is this signal that produces the droplet population vs charge level spectrum on the multichannel analyzer (MCA) shown in Figure 4. These data and the operating state of the droplet source of the quadrupole mass spectrometer form the raw data suite that is used as a basis for analysis of droplet behavior.

Calibration –

The most crucial and time consuming aspect of the experiment involved calibration. Low mass (high charge to mass) instruments, which can be calibrated with well defined atomic and molecular species, have exhibited excellent agreement of predicted and actual performance. Although comforting, the droplet charge to mass range is too far removed

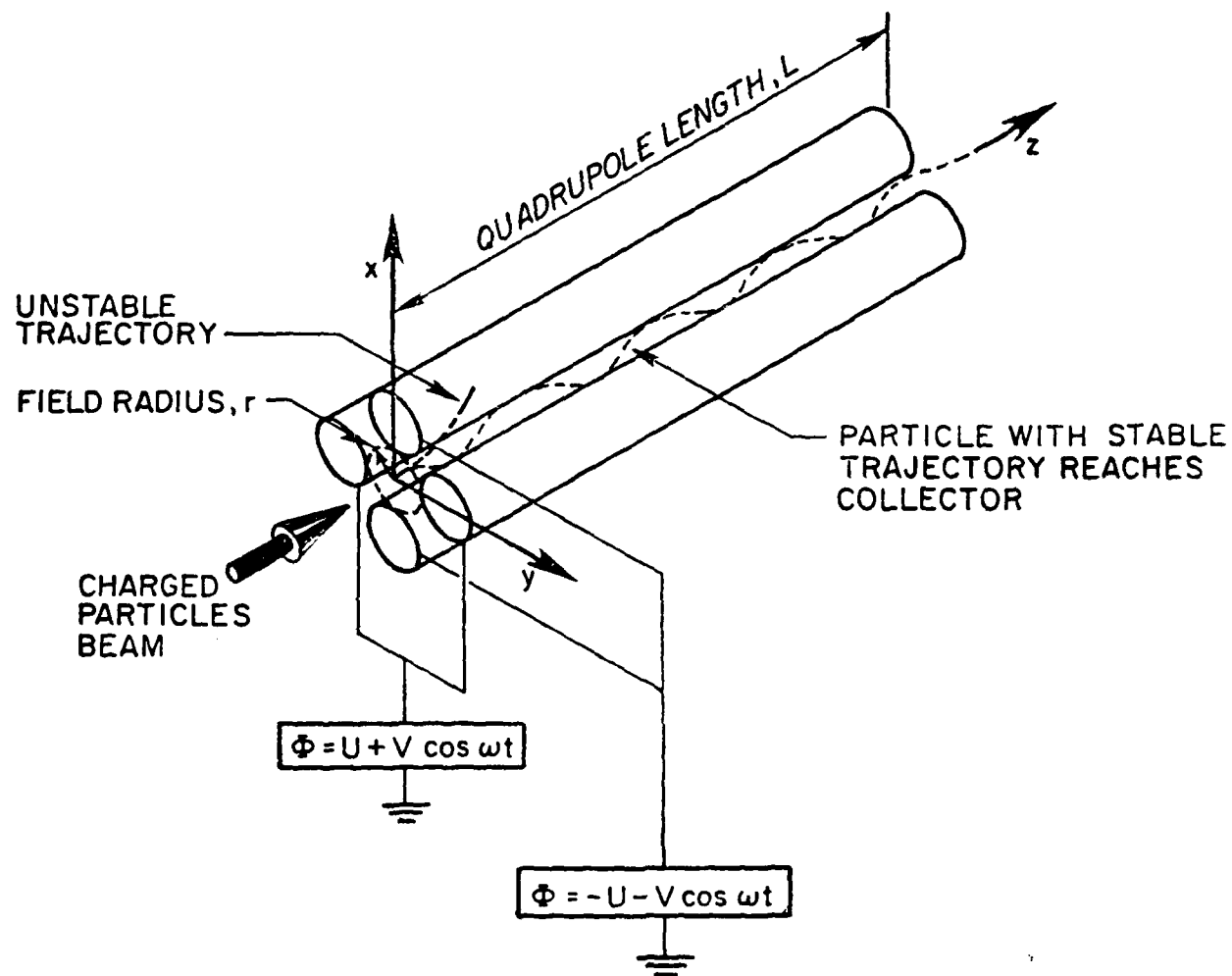


Figure 3. Quadrupole Mass Spectrometer

Raw Data from MCA
(Octoil Data at 1.23 C/kg)

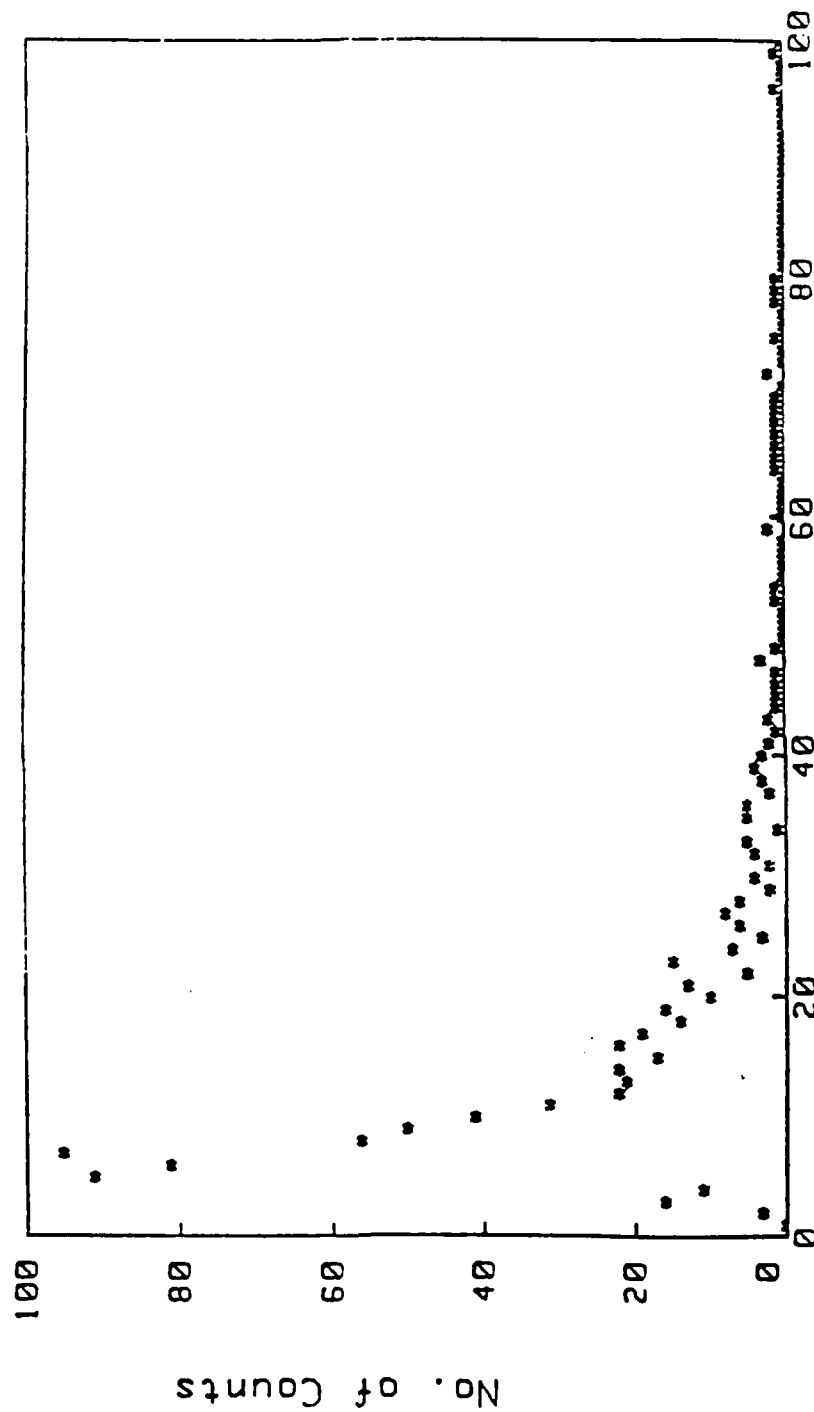


Figure 4: Channel Number

from typical experience to permit confident extrapolation. In the absence of a clearly defined calibration source, in the range of interest, it is necessary to resort to the use of droplet data obtained from an independent measurement technique for comparison. This other technique, a time of flight charge, charge to mass ratio measurement method, [18] also uncalibrated, has the advantage of minimum data reduction complexity. Since the only such data involve the use of an octoil (dioctyl phthalate) spray, an octoil sprayer was developed for use with the QMS/HSE experiment.

Only if the results of both experiments are in agreement can there be confidence that the QMS/HSE is providing quantitative data. Otherwise there is no means by which a judgment of the validity of either technique can be made. The comparison of data sets obtained by both techniques, shown in Figure 5, displays the level of agreement that exists. The initial comparison made with high charge to mass ratio ($\geq 10^3 \text{C/m}^3$) is in excellent agreement with the time of flight data of Hendricks. This congruence of the two experiments is sufficiently precise for us to conclude that the QMS/HSE experiment and the time of flight measurements are both quantitative. It is worth noting that whereas the Hendricks experiment involved manual data collection and a very limited number of spray droplets the computerized QMS/HSE experiment permitted two orders of magnitude larger data base to be developed.

Subsequent tests conducted at charge density levels below 10^3C/m^3 , the range of most interest, produced data that increasingly diverged with decreasing charge density level from that published by Hendricks. This behavior was ultimately traced to charge relaxation at the detector surface, as discussed in Appendix B. Briefly, what we discovered is that the relatively high resistivity of the octoil used in the test produces charge relaxation times for the transfer of droplet charge to the metallic charge detector plate that are comparable to, or larger than, the gated charge acceptance time scale of the charge detector circuit. The reason this effect only occurs for the larger, less highly charged droplets is simply related to the relaxation time scale being a function of conductivity, which, in turn, is dominated by the mobility, charge density term. Once this factor was taken into account, excellent agreement between the two data sets is obtained over the entire charge density range, as displayed in Figure 5.

Octoil Spray Testing -

Having established that the QMS/HSE instrument is capable of measuring both the charge and the mass of all droplets (and deagglomeration debris) having charge to mass ratios between 3C/kg and 0.1C/kg and with total surface electron counts larger than 280,

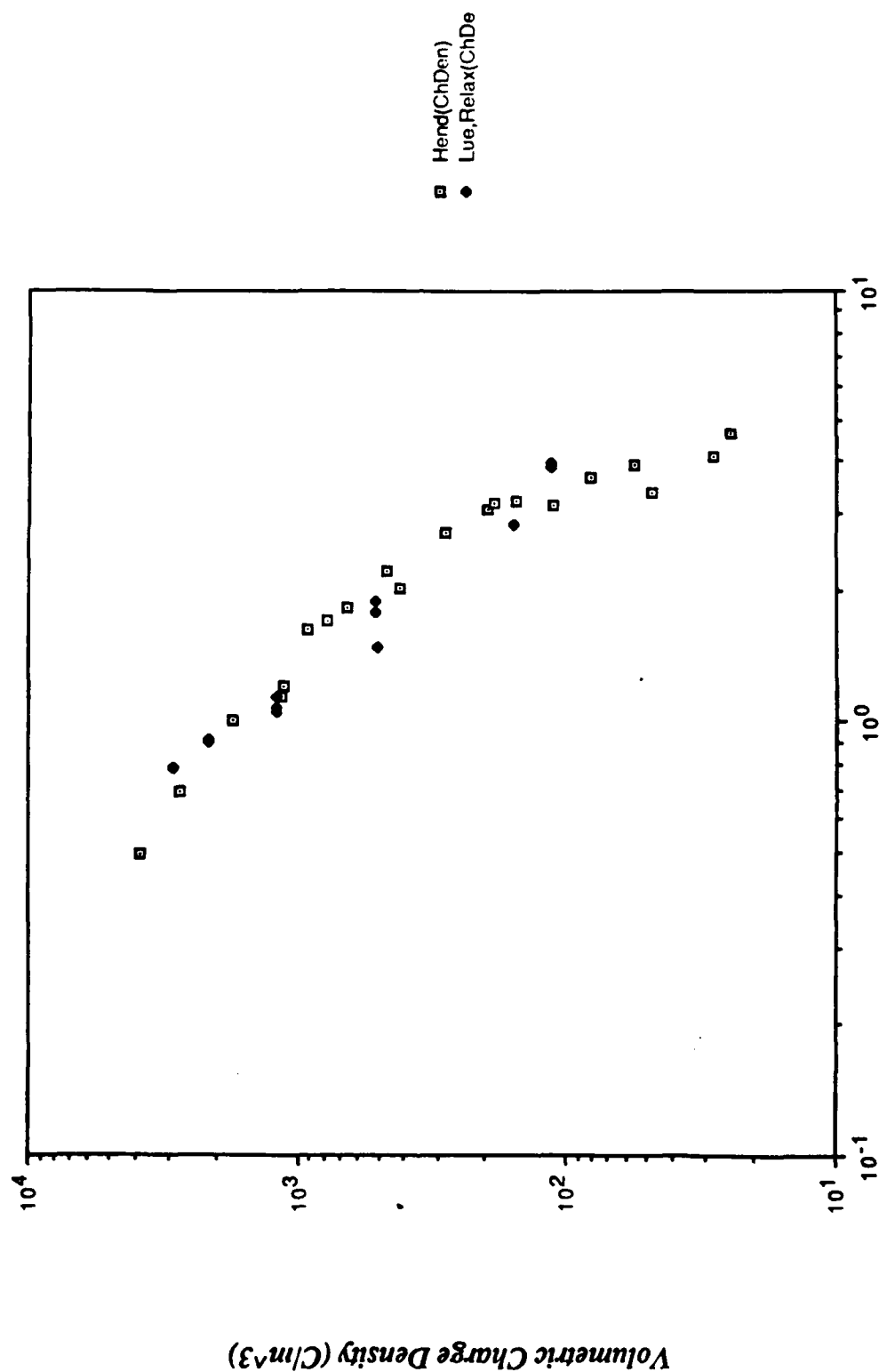


Figure 5: Average Droplet Radius (Microns)

the research was directed toward the use of this instrument to analyze the octoil spray. This effort was motivated by several factors. First, this study would provide a convenient means to become familiar with the apparatus and to assess its capabilities. Second, little quantitative droplet spray data exists and the results of the investigation would represent a valuable contribution to the sparse data base. Third, data would be obtained in the droplet size and charging realm in which the Statistical Equilibrium Model of electrostatic spraying predicts the existence of an enigmatic phase transition, about which nothing is known. And, fourth and finally, it was anticipated that the availability of quantitative information concerning droplet behavior in this charge and mass interval would provide insight into the physics of surface charging and would make it possible to understand why it is necessary to invoke the disquieting assumption of limited surface mobility in order to model the Rayleigh Bursting phenomena [8]. It is this question above all that motivated the decision to devote the bulk of our resources to this study.

Background -

In addition to the octoil data previously mentioned, comparable droplet mean charge to mass ratio *vs* radius data exist only for Woods' metal [19] and glycerin [20]. Despite the sparseness of this data base, it is sufficient to set as a first test of the validity of the Statistical Equilibrium Theory of electrostatic atomization [21-23]. This is illustrated by the comparison of the octoil and Woods' metal data and theory presented in Figure 6. The Statistical Equilibrium Theory is a thermodynamic model insofar as it is based on the premise that the long-range electrostatic force field in charged fluids will guarantee that all physical states of the spray system are "well-mixed", are in intimate communication and result in the most probable end state — the maximum entropy (equilibrium) end state [21-23]. These states are shown to be describable in terms of the product of two coupled distributions; the Maxwell-Boltzmann distribution for droplet number and Fermi-Dirac for charging. Use of the Lagrangian multiplier method, to define the most probable state, results in the following two descriptive equations for all Rayleigh Limit restrained electrostatic atomization:

$$\frac{\ln Z - \ln(1-Z)}{Z \ln Z + (1-Z) \ln(1-Z)} + \alpha' \left(\frac{4\gamma}{\epsilon_0 E_s^2} \right)^{-3/2} r^{3/2} + \beta' \frac{\epsilon_0 E_s^3 q}{4\gamma} r^2 Z = 0 \quad (1)$$

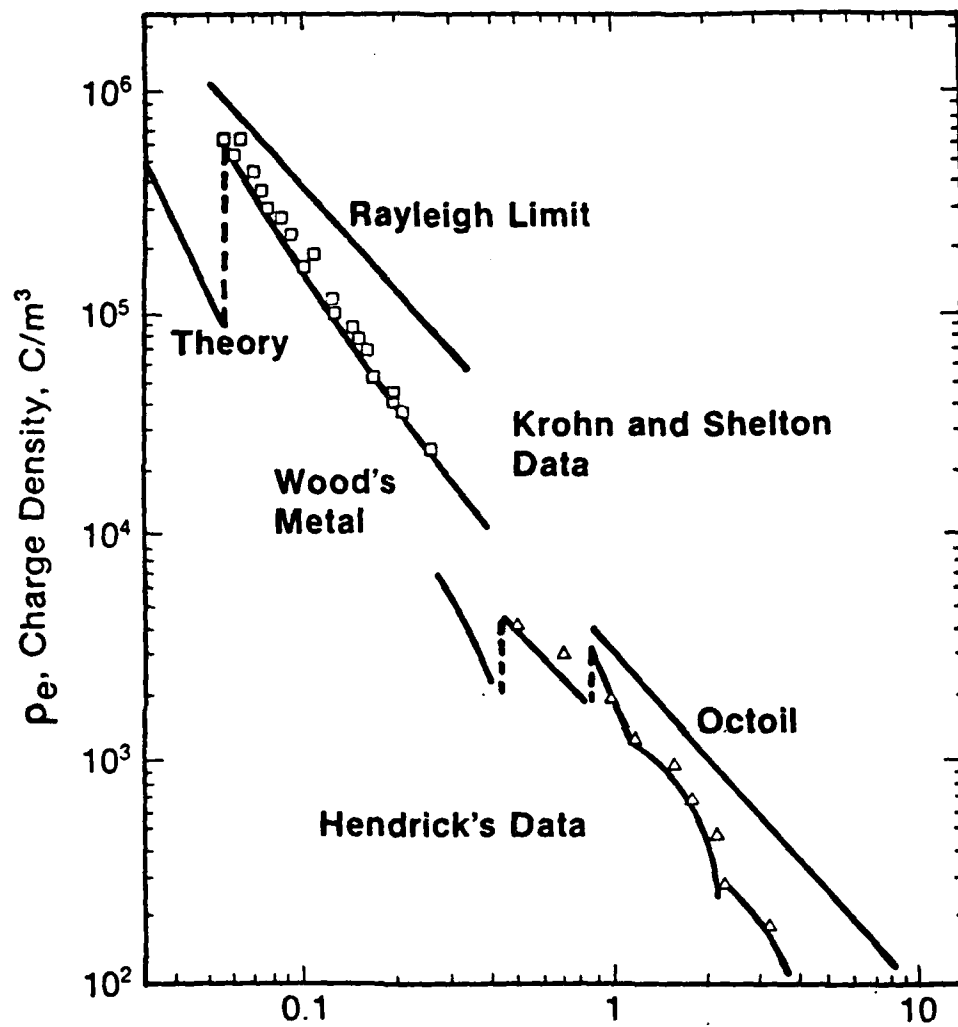


Figure 6: r , Droplet Radius- μm

$$N = \exp \left\{ \alpha' Z \left(\frac{4\gamma}{\epsilon_0 E_s^2} \right)^{-3/2} r^{3/2} + \beta' \frac{\epsilon_0 q E_s^3}{16\gamma} (1 + 2Z^2) r^2 + \delta' \frac{\rho q \epsilon_0 E_s^3}{48\gamma^2} r^3 \right\} \quad (2)$$

where α' , β' , and δ' are the Lagrangian multipliers representing the conservation law restraints of charge, energy and system mass, respectively. The system is defined in terms of droplet number N and the charge parameter Z , defined as the fraction of Rayleigh limit charging. Within the context of this model, the surface tension (γ), fluid density (ρ), and surface electron field emission limit, E_s , are the only fluid properties of fundamental importance to the description of electrostatic spraying. The permittivity ϵ_0 and the electron charge q are the only other parameters in the model.

Comparison of the charging equation with data, as illustrated in Figure 6, yields the startling result that the ratio of the charging and energy Lagrangian multipliers (α'/β') is a constant and is numerically equal to $\sim -66\text{eV}$. Physically, this means that, on average, a droplet in either the Woods' metal and the octoil sprays, and by implication all sprays, are charged to levels that require an expenditure of $\sim 66\text{eV}$ to bring another charge to their surface. This unexpected result must reflect an underlying fundamental mechanism insofar as all of the physical properties of these materials differ by at least an order of magnitude and the individual values of α' and β' differ by approximately four orders of magnitude. Additional work has verified that $-\alpha'/\beta'$ is a constant for a wide variety of fluids including No. 2 Heating Oil and Jet-A, to name but two.

Equally startling are the ramifications of the fact that α'/β' is a "constant of motion" for spraying. This can be seen in Figure 7, which illustrates the theoretical mean droplet charging behavior, derived from the charging equation when $-\alpha'/\beta' = 66\text{eV}$. Droplet charging is predicted to undergo a first order phase transition that, in the case of hydrocarbon oils, occurs at a mean diameter of about one micron. Moreover, the behavior of sprays having droplet sizes larger than the transition diameter is described by the energetically favored middle solution branch. In fact, all of the available data have been obtained in this regime; none is available for droplet sizes smaller than the transition.

In addition, the theory predicts that along this central solution branch (branch B) the mean droplet size will be independent of all fluid properties and will be determined uniquely by the fluid charge density level. This pertains to all sprays on the large droplet side of the transition providing the physical properties of the spray fluid are not extreme (eg. viscosity $\lesssim 200\text{cp}$) [23]. The independence of mean droplet size on fluid property

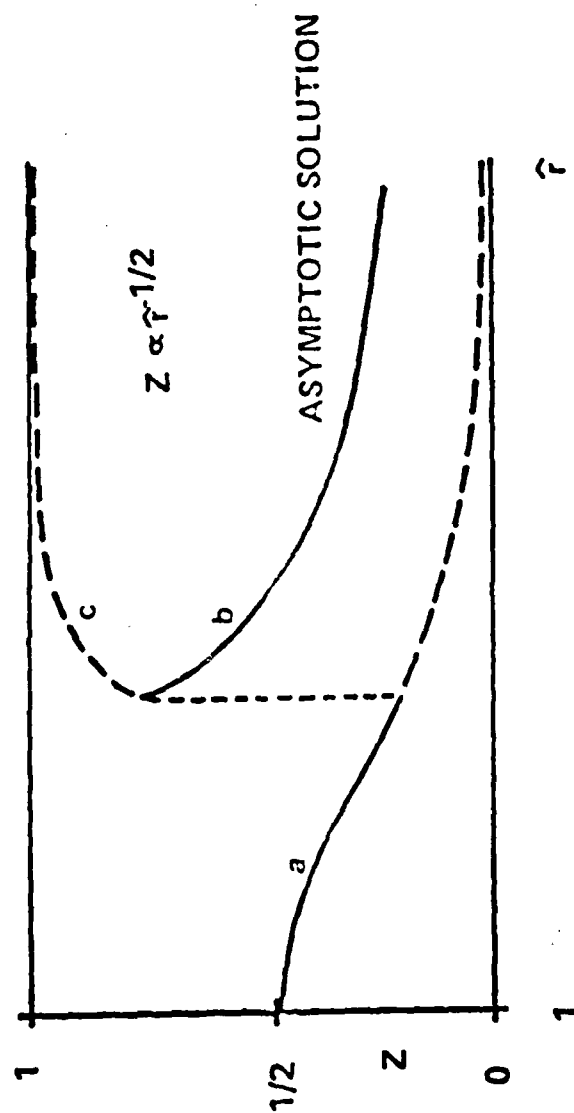


FIG. 7 RELATIVE CHARGING LEVEL vs. DROPLET SIZE

implies that the spray process is controlled by strictly electronic phenomena. Most intriguing is the indication that the size of sibling droplets produced by Rayleigh Bursting are in the vicinity of the transition size. Collectively, these factors were sufficiently compelling to make the study of this transition region the focus of our research effort. It can be argued that since the transition establishes the scale of spraying, it also dominates the Rayleigh Bursting process, which is a more restricted form of the spray process.

QMS/HSE and the Phase Transition -

The phase transition for Woods' metal and octoil has the form noted in Figure 8 when plotted in terms of the charge to mass ratio, droplet charging parameter space of the QMS/HSE experiment. Although the experiment will ultimately be capable of operation within a full four order of magnitude charge to mass ratio range (0.01 to 100C/kg), the available range of ~ 0.1 to ~ 3 C/kg fortuitously brackets the predicted octoil phase transition. Note that only the mean droplet charge level is displayed in this figure. Consequently, since there is a distribution of droplet charging levels about the mean, operation at fixed charge to mass ratio will produce a "charging spectrum" (droplet number vs charge level) that will consist of three peaks, one each for the A, B and C branches. If present, these peaks will be broadened by the small but finite bandwidth of the QMS/HSE, which is typically maintained at 3 to 5% of the mean charge to mass ratio, as explained in Appendix B.

Appendix B should also be consulted for details of the manner in which the charge spectrum data are reduced. Briefly, the charging and droplet number distributions have been recast in terms of the measurables, charge to mass ratio and charge, and have been reformulated to permit the fundamental spray (α' , β' , δ') and droplet property parameters (ϵ , E_s) to be evaluated. Attempts to fit the data with a single distribution proved fruitless. Independent of the charge to mass ratio of the data used, the SAS Institute non-linear regression program [24] that has been used for all data reduction was always able to obtain a more accurate fit to the data when using two distributions as opposed to when one distribution was fit. All attempts, in which the program was asked to fit the theoretically expected three distributions (one each for branch A, B and C), were indistinguishable from the two distribution result. This outcome is to be anticipated since, in the charge to mass ratio being scanned, the presence of branch C would be in the noise level of the experiment.

Figures 9 through 13 show the results of the automatic fit of dual distributions to the QMS/HSE data. Quantitatively, the results conform to expectation. At the highest

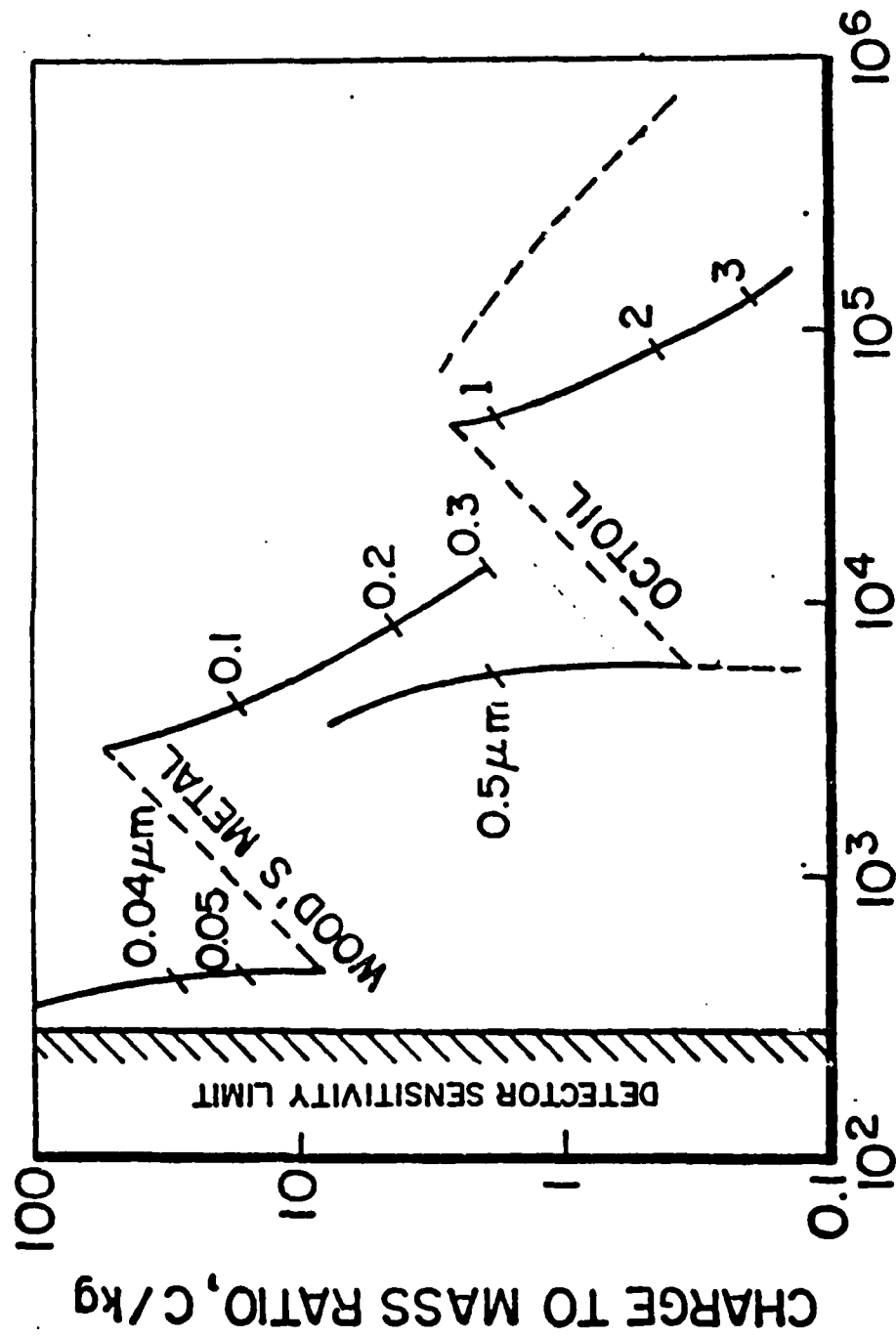


Figure 8: SURFACE ELECTRON COUNT

Double Distribution Fit for QM95 Octoil Data @2.93 C/kg

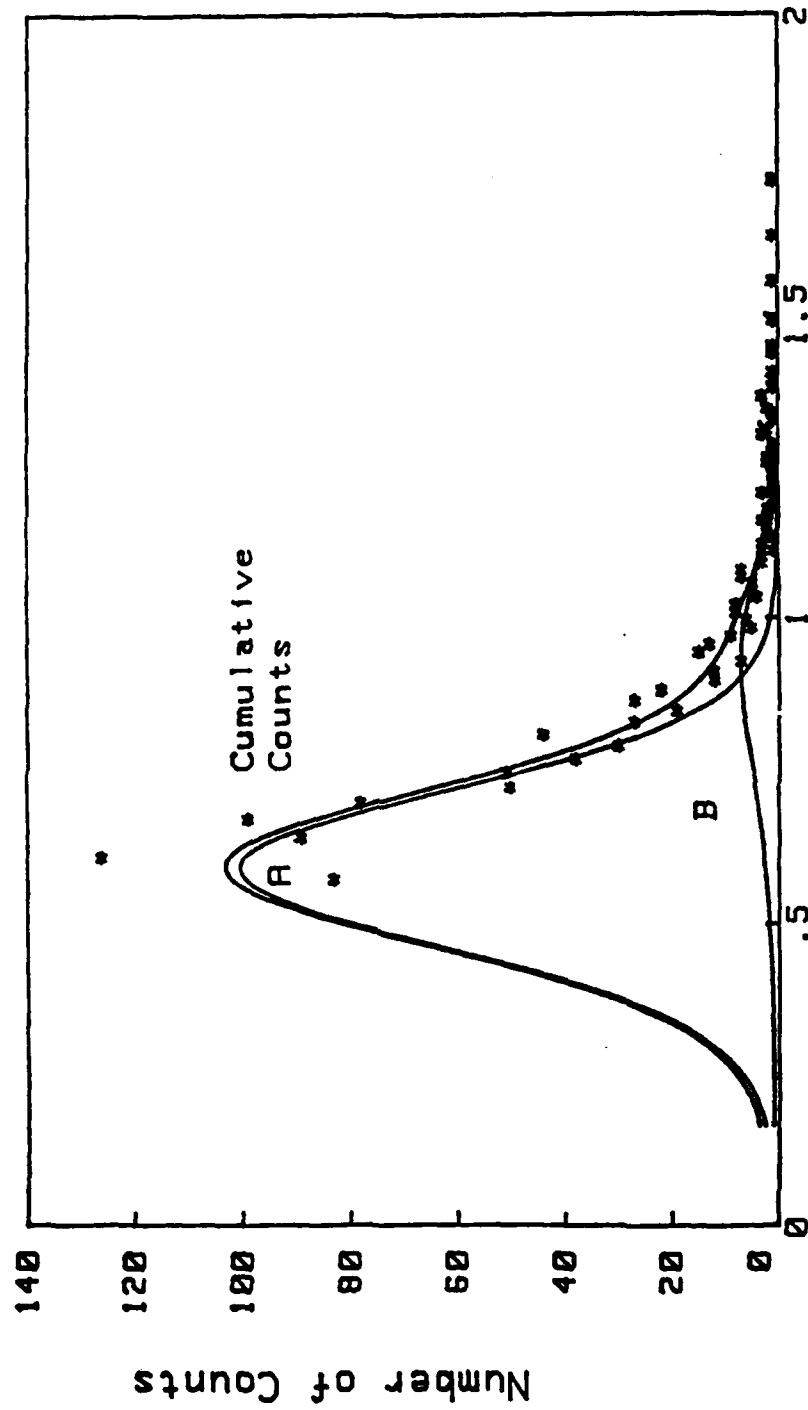


FIGURE 9: Radius (Microns)

Double Distribution Fit For QM93 Octoil Data @2.20 C/kg

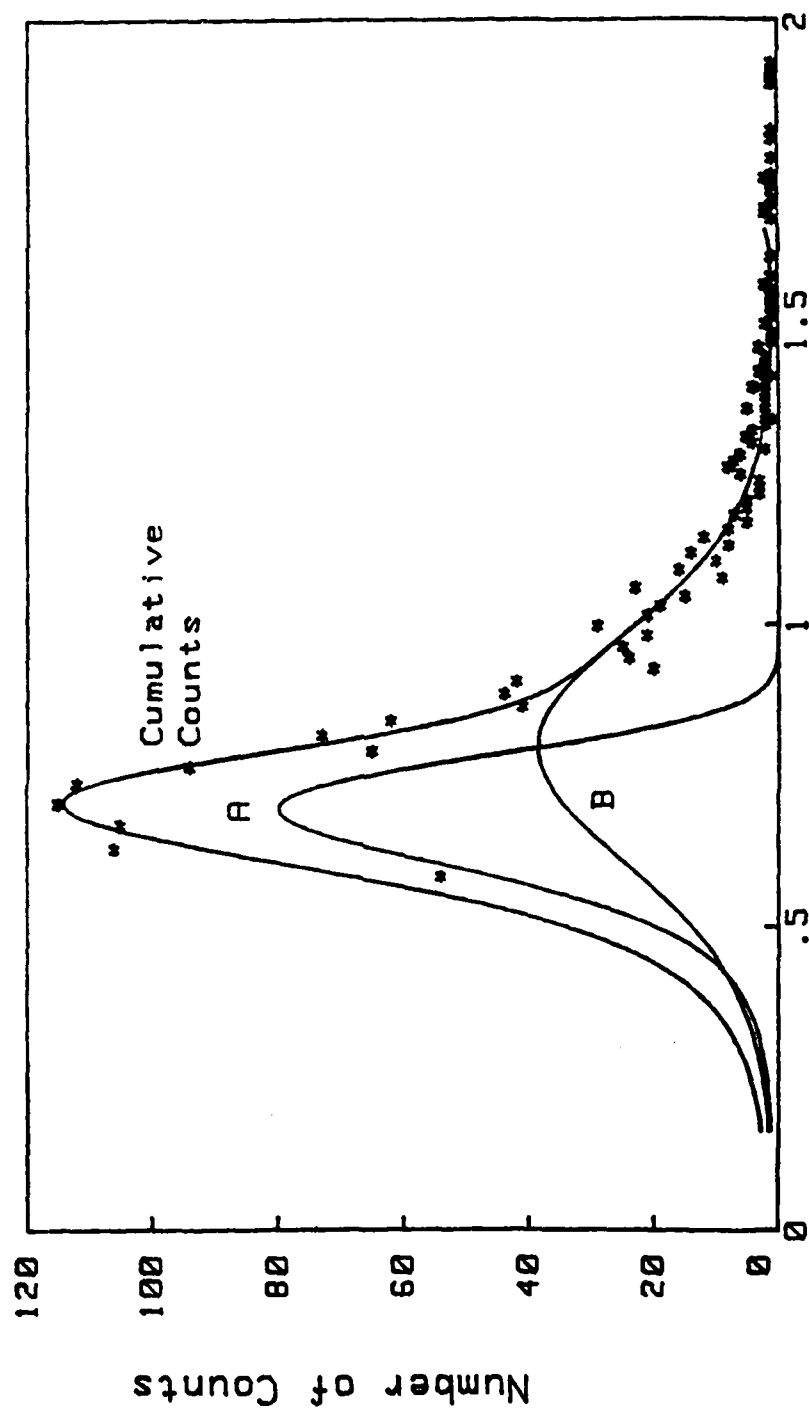


FIGURE 10: Radius (Microns)

Double Distribution Fit For QM90 Octoil Data @1.23 C/kg

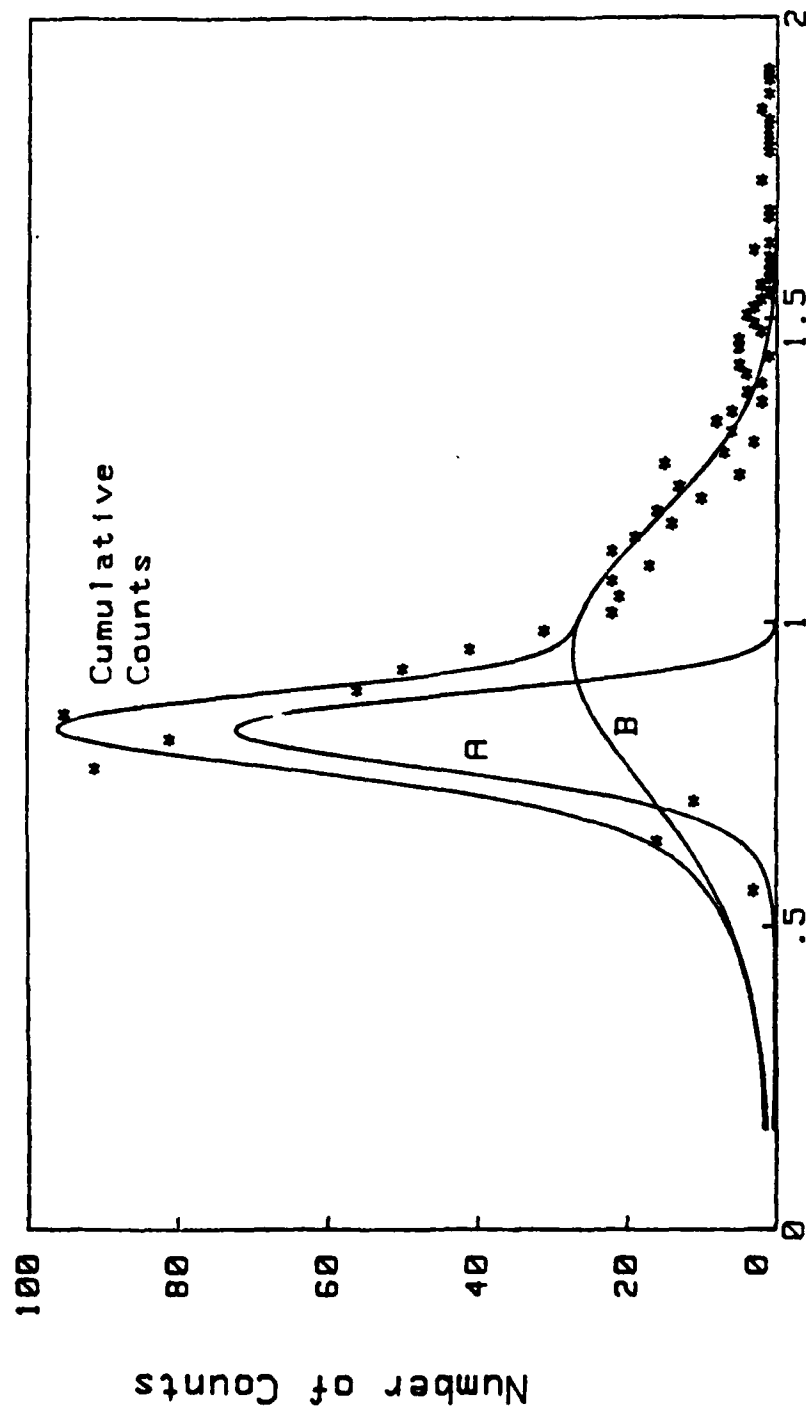


FIGURE 11: Radius (Microns)

Double Distribution Fit For QM91 Octoil Data @0.53 C/kg

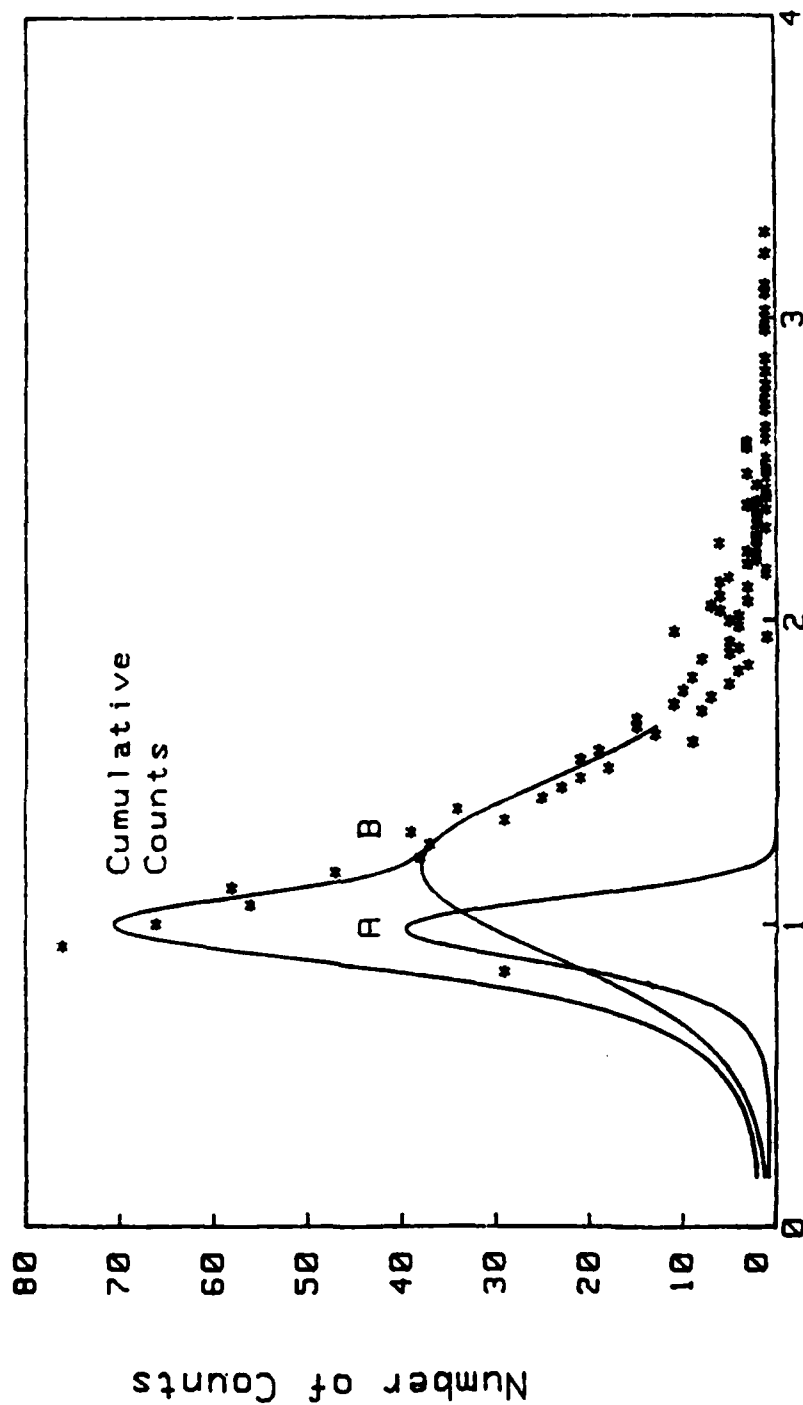


FIGURE 12: Radius (Microns)

Double Distribution Fit for QM100 Octoil Data @0.118 C/kg

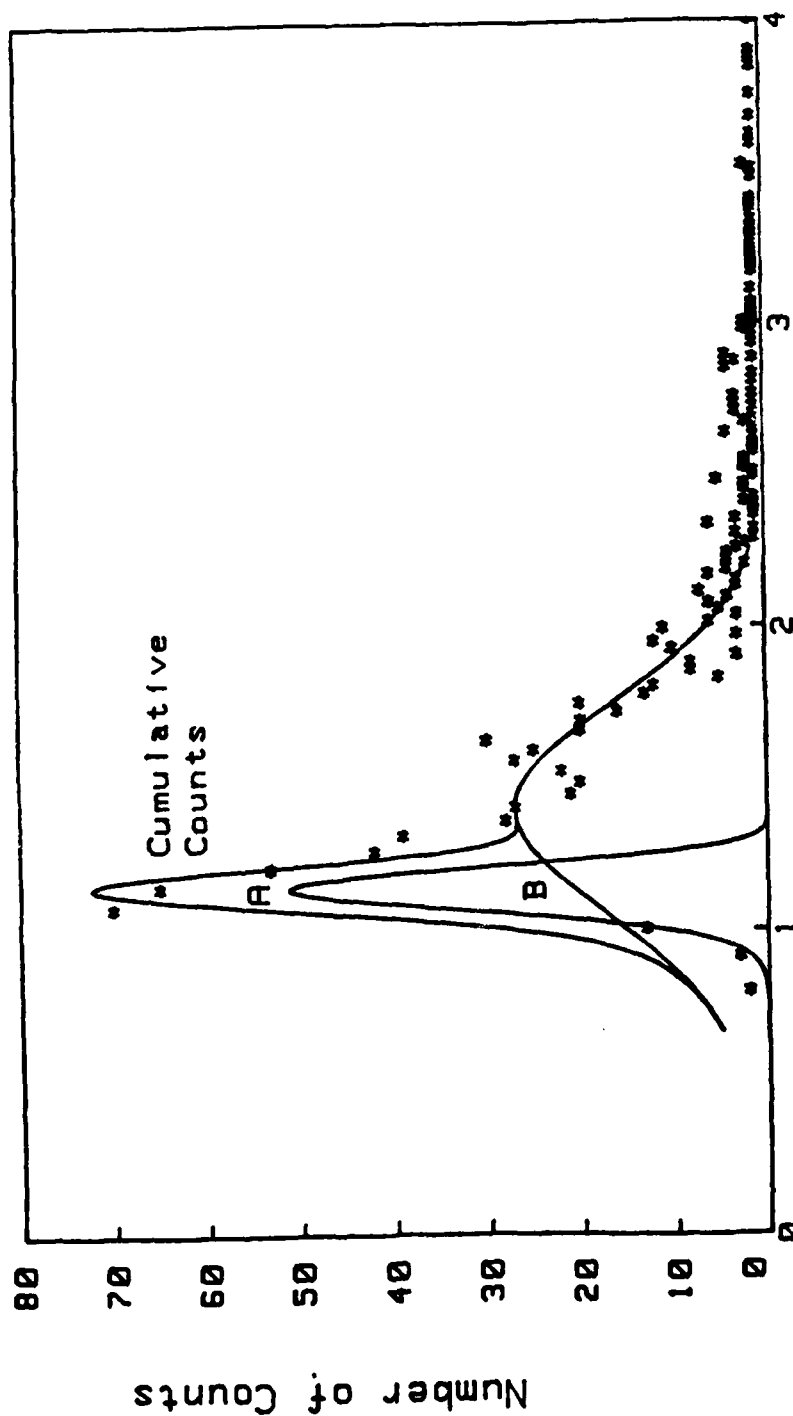


FIGURE 13: Radius (Microns)

charge to mass ratio accessible with the QMS/HSE (Figure 9, 2.93C/kg), the dominant feature is the branch A, and little if any contribution is to be made by branches B and C (cf. Figure 8). This operating state is close to the theoretically predicted small droplet, high charge density side of the transition. Subsequent figures, obtained at successively lower charge to mass ratios, show the emergence of the central "B" branch. In addition, the data are also consistent with theoretical expectations with respect to the drift of the distribution peaks for the A and B branches to successively larger droplet sizes as a function of increasing charge density level.

It is obviously desirable to probe the high charge density realm upward from the $\sim 3\text{C/kg}$ level of the present experiment and away from the transition to demonstrate unequivocally that spray behavior continues to be monomodal as demanded by theory. Equally desirable would be the collection of data at lower charge density levels than the 0.118C/kg of Figure 13 and away from the transition in the large droplet direction to establish how the dominance of the central B branch is attained and spray monomodality is restored. However, pending the modification of the experiment and the collection of these data, sufficient data have now been obtained to permit a number of definitive statements concerning the phase transition and the behavior of charge on the droplet surface to be made.

Results —

Since the QMS/HSE experiment is conducted under hard vacuum ($\sim 10^{-6}\text{Torr}$), and since evaporation of the octoil is negligible, the permittivity of background medium was taken to be that of vacuo. By fixing $\epsilon = \epsilon_0$, the distribution function coefficients obtained from the SAS Institute non-linear regression fit program can be used to extract values for the limiting electric field strength E_s . The results of this analysis are displayed in Figure 14 where the limiting, emission electric field E_s is shown plotted verse charge to droplet mass ratio as determined by the quadrupole mass spectrometer.

Several features of these data are noteworthy. First, the behavior of E_s for each of the branches (E_{sa} & E_{sb}) exhibit the same trends with charge to mass ratio. Secondly, the measured values are related by a factor of 5/3. That is, for all of the data available, covering approximately a twenty fold variation in Q/M (0.12 to 2.2), the ratio of the B branch to the A branch limiting electric field is $E_{sb}/E_{sa} = 5/3 \pm 8\%$. Although the data are limited, the limiting electric field can be reasonably taken to be invariant with charge to mass ratio for charge to mass ratios greater than about 1C/kg . More data are required in the range between 1 and $\sim 3\text{C/kg}$, where the B branch disappears and the quality of the

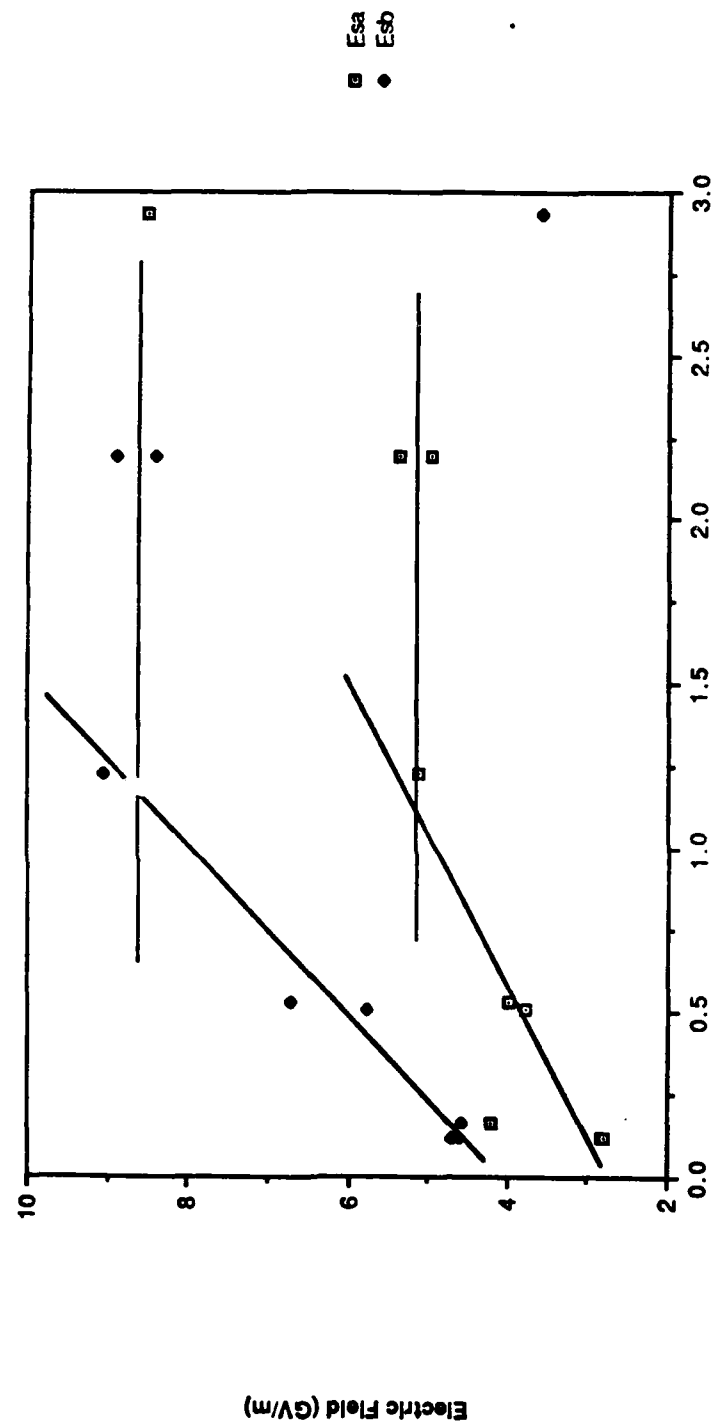


Figure 14: Charge to Mass Ratio (C/kg)

available test results is questionable. However, based on the three data runs we have obtained, the B branch droplets have a limiting field strength of $\sim 9\text{GV/m}$ in contrast to $\sim 5\text{GV/m}$ on the high charge density A branch.

In the charge density realm below $\sim 1\text{C/kg}$, the A branch is truncated, as anticipated, at a charge density level of about 0.1C/kg . On the basis of the available six data points, the data neatly describe a linear relationship of E_s and Q/M . It is interesting to note that the minimum value for the A branch (at $\sim 0.1\text{C/kg}$) is 2.8GV/m , which is comparable to 4.2GV/m value projected for the B branch for low Q/M values. These low values of emission field are compatible with published values for negative (electron) emission [25-27].

As yet there is no explanation for these trends, nor do we have any basis for understanding the distinct regularity of the E_{sa}/E_{sb} ratio. A provocative feature of these data is the relationship that exists between dielectric permittivity ϵ and the limiting electric field E . These two parameters appear as a product having the form $\epsilon^4 E_s^6$. When interpreted in terms of a fixed immutable limiting electric field and a variable permittivity, all of the available data (for $0.1 \leq Q/M \leq 2.2$) can be summarized in terms of the effective dielectric constant for the large droplet B branch being some 2.1 ± 0.2 times that of the small droplet A branch.

It is this curious result that has strongly suggested that a fundamental shift in the configuration of surface charge is occurring at the transition. That is, the data imply that the surface charge is in a plasma state (low permittivity) on the small droplet side of the transition and is in a condensed state (crystallized) on the large droplet side — the side defined by the B branch. At this point our lack of sufficient data makes this an inferential conclusion. However, support for this conclusion can be found in what has been established concerning the behavior of droplet systems on the large droplet B branch. The evidence is as follows:

1. The first principles Analysis of Rayleigh Bursting presented in the Roth/Kelly paper (8) requires that the surface charge mobility be small or zero. No other assumption permits a model to be developed that is consistent with the available data.
2. The first principles electrostatic spray model with fixed $-\alpha'/\beta'$ (verified by this work) reveals that beyond the transition mean droplet size is not a function of fluid properties. It is solely dependent on charge density level and, is thus, a purely electronic effect.

3. Estimates, discussed below, indicate that the mean electrostatic energy of the droplet surface charge along the B branch is constant, independent of droplet size and is consistent with what is known about the electron crystallization process.

The Electron Crystal

One of the more perplexing aspects of this theoretical work is the predicted discontinuous charging. For all intents and purposes the trace of predicted charging level vs. droplet size represents a first order phase transition (cf. Figure 7). This phase transition in droplet charging level is explicable within the context of Coulomb crystallization.

Evidence for this is presented in Figure 15 where the ratio of electrostatic to thermal energy for individual droplet surface electrons is shown plotted vs. droplet radius using the α' , β' parameters from the octoil data [21-23]. The phase transition behavior is clearly evident. As droplet radius increases the energy ratio increases reaching a peak of 136 prior to decreasing along the single solution portion of the plot. This value is interestingly close to the critical value $\Gamma_m = 137$, noted by Brinkman, et al. [28] for the formation of planar electron "crystals". It should be noted that a similar calculation for Wood's metal yields a peak value of 122 (cf. the table). However, this value is based on the assumption that the data were collected at the melting point. The actual test temperature is uncertain.

As the spray droplet size is increased, the energy ratio decreases until the onset of multiple solutions at a critical droplet radius of $\sim 0.85 \mu\text{m}$. It is the central, minimum energy branch to which actual sprays conform.

Immediately after the discontinuity and bifurcation the ratio on this branch decreases from somewhat above the asymptotic level of 437 to slightly below, and rises slowly to ultimately attain this value for large droplet sizes. The virtual constancy of the energy ratio is apparent. As is noted on the plot, the mean electrostatic energy of individual surface charges is $(-\alpha'/\beta')/6$ or 11eV; a value that is suggestively close to the first ionization potential of hydrocarbons [29,30]. By comparison it requires an average energy expenditure of $-\alpha'/\beta' = 66\text{eV}$ to transport a charge to the surface of droplets in the plume.

The essential feature to note is that the energy ratio is predicted to change abruptly from a value that is below the putative critical value of 137 to a level that is pi times as high. It is this behavior that prompts the suggestion that Coulomb crystallization is occurring on spray droplet surfaces in the same manner that it is known to occur in planar electron clouds that can be formed in close proximity to liquid helium surfaces.

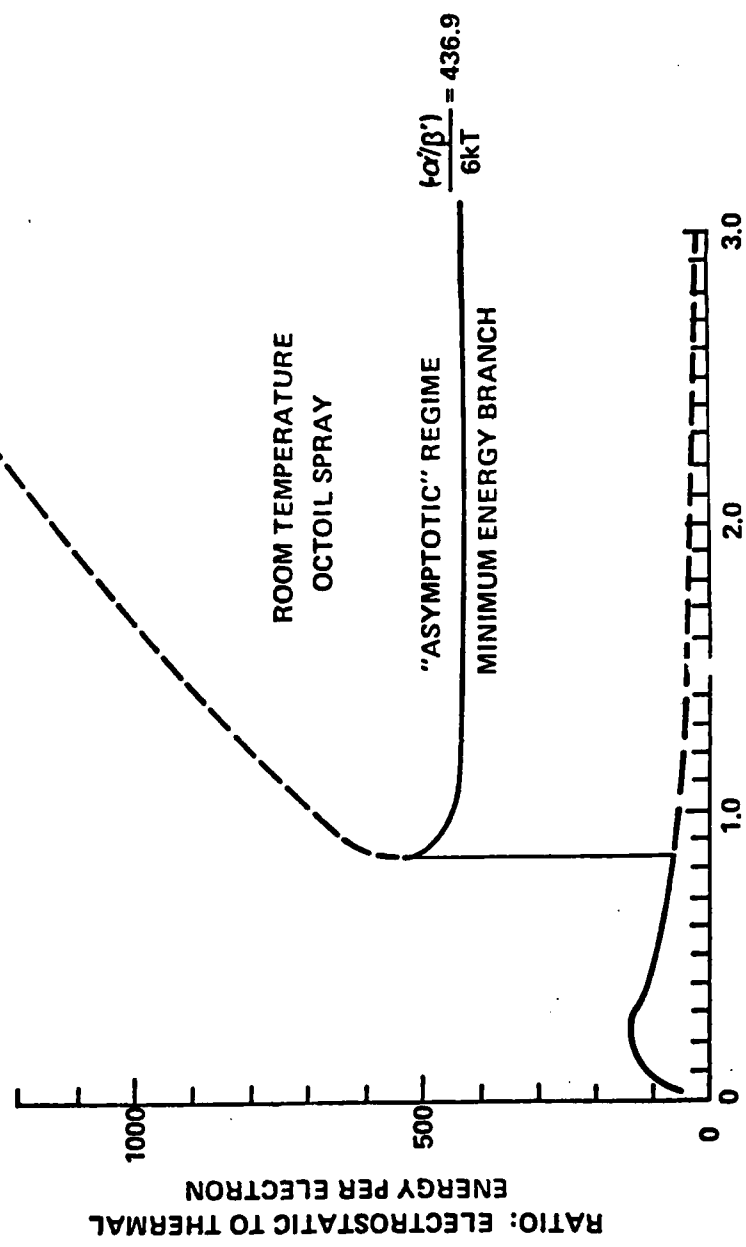



Figure 15: DROPLET RADIUS · μm

Wood's metal sprays are sufficiently similar to those of octoil as to suggest that a universality of behavior exists. This is exhibited in Figure 16 where the ratio of electrostatic to thermal energy per surface electron is normalized by the asymptotic value. This normalization eliminates the uncertainty of test temperature from the result and reduces the ordinate to a ratio of electrostatic energies. In addition, the droplet radius has been normalized by the discontinuity value. The detailed similarity of the relative behavioral pattern of the two physically disparate liquids is apparent. The parameter listing of the table permits an absolute comparison to be made.

Several facts are certain: 1. the use of empirically derived values for α' and β' (from the available data for octoil and Wood's metal), when applied to the statistical equilibrium model of electrostatic spraying, predicts discontinuous spray charge behavior, 2. the discontinuity brackets the currently accepted energy ratio for the occurrence of Coulombic crystallization, and 3. the asymptotic spray regime corresponds to a fixed energy ratio value that is well above that required for crystallization to occur. We conclude that droplets in electrostatic sprays having mean sizes larger than about one micron and similarly charged isolated droplets are encased in electron crystals and that the fluid in these crystals is irrelevant except to form a surface upon which crystallization can occur. This offers an opportunity to use this unique form of matter for catalysts or in applications such as oscillators or where precise control of the state of electrons is of interest and importance.



A.J. Kelly
Senior Research Engineer

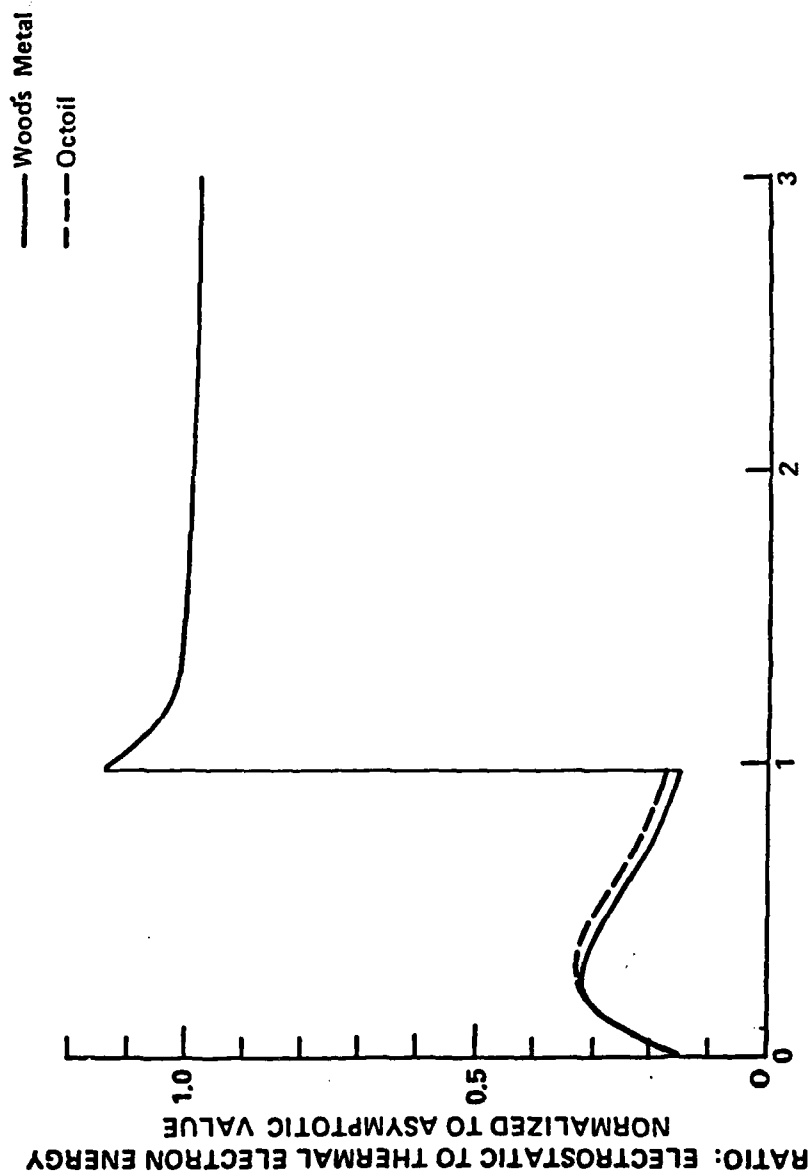


Figure 16: DROPLET RADIUS NORMALIZED TO DISCONTINUITY RADIUS

DROPLET SURFACE CHARGE PARAMETERS

TABLE

	<u>Fluid</u>	
	<u>Octoil</u>	<u>Wood's Metal</u>
<u>Pre-discontinuity Peak</u>		
Energy ratio	137*	122**
Droplet radius (μm)	0.23	0.020
Charge density (m^{-2})	5.2×10^{15}	6.5×10^{16}
<u>Discontinuity</u>		
Energy ratio	68 → 493	65 → 415
Droplet radius (μm)	0.87	0.060
Charge density (m^{-2})	$7.3 \times 10^{14} \rightarrow 4.8 \times 10^{15}$	$1.1 \times 10^{16} \rightarrow 6.2 \times 10^{16}$
<u>Asymptotic Energy Ratio</u>		
	437	373

* T = 293° K

** T = 343° K

REFERENCES

1. A. Doyle, D.R. Moffett, B. Vonnegut, "Behavior of Evaporating Electrically Charged Droplets", *J. Colloid Sci.* **19**, 136, 1964.
2. M.A. Abbas, J. Latham, "The Instability of Evaporating Charged Drops", *J. Colloid Mech.*, **30**, 663, 1967.
3. J.W. Schweizer, D.H. Hanson, "Stability Limit of Charged Drops", *J. Colloid Interface Sci.*, **35**, 417, 1971.
4. J.V. Iribane, B.S. Thompson, "On the Evaporation of Small Ions from Charged Droplets", *J. Chem. Phys.* **64**, 2287, 1976.
5. S.E. Law, "Charge and Mass Flux in the Radial Electric Field of an Evaporating Charged Water Droplet: An Experimental Analysis", Proceedings of the 21st IEEE/IAS annual meeting, Denver, CO, Sept. 28 – Oct. 3, 1986, p.1434. Accepted for publication IEEE Transactions on Industry Applications.
6. Lord Rayleigh, "On the Equilibrium of Liquid Conducting Masses Charged with Electricity", *Phil Mag* **14**, 184, 1882.
7. A.E. Cerkanowicz, "Rayleigh Limit for Non Stationary Charged Drops", Proceedings of the 16th IEEE/IAS annual meeting, Philadelphia, PA, Oct. 5 – Oct. 9, 1981.
8. D.G. Roth, A.J. Kelly, "Analysis of the Description of Evaporating Charged Droplets, IEEE Transactions on Industry Applications, *IA-19*, 771, 1983.
9. H.M.A. Elghazaly, G.S.P. Castle, "Analysis of the Instability of Evaporating Charged Liquid Drops", IEEE Transactions on Industry Applications, *IA-22*, 892, 1986.
10. H.M.A. Elghazaly, G.S.P. Castle, "Analysis of Multisibling Instability of Charged Liquid Drops", IEEE Transactions on Industry Applications, *IA-23*, 1, 108, 1987.
11. W-K Rhim, M.M. Saffren, D.D. Ellemann, "Development of an Electrostatic Positioner for Space Material Processing", *Rev. Sci. Inst.* **56**, 1, 307, 1985.
12. W-K Rhim, S.K. Chung, E. Trinh, M.T. Hyson, D.D. Ellemann, "Large Charged Drop Levitated Against Gravity", IEEE-CH 2272, 1383, 1986.
13. P.J. Burt, E.H. Adelson, "The Laplacian Pyramid as a Compact Image Code", IEEE Trans. Communication, COM **31**, p.532, 1983.
14. D. Trevor, W. Kwangyoen, "Calculating Depth from Focus Using a Pyramid Architecture", Grasp Laboratory, Department of Computer and Information Science, University of Pennsylvania, 1987.
15. H.M.A. Elghazaly, G.S.P. Castle, "Experimental Study on the Break Up of Charged Liquid Droplets", Proceedings of the 21st IEEE/IAS annual meeting, Denver, CO, Sept. 28 – Oct 3, 1986, p.1429. Accepted for publication in the IEEE Transactions on Industry Applications.
16. M. Moshrrafa, H.T. Oskam, "Design and Construction of a Mass Spectrometer for the Study of Basic Processes in Plasma Physics", NP-11459, U.S. Dept. of Energy, Oak Ridge, TN, 1961.
17. P.H. Dawson, N.R. Whetten, "Mass Spectroscopy Using RF Quadrupole Fields", *Adv. in Electronics and Electron Physics*, vol. 27, Academic Press, p.59, 1969.
18. C.D. Hendricks, Jr., "Charged Droplet Experiments", *J. Colloid Sci.* **17**, 249, 1962.
19. V.E. Krohn, Jr., "Liquid Metal Droplets for Heavy Particle Propulsion", in *Progress in Astronautics & Rocketry*, vol. 5 Electrostatic Propulsion. D.B. Langmuir, E. Stuhlinger, J.M. Sellen, Jr., Eds. Academic Press, NY, 73, 1961.
20. R.J. Pfeifer, C.D. Hendricks, Jr., "Charge to Mass Relationships for Electrohydrodynamically Sprayed Liquid Drops", *Physics of Fluids*, **10**, 2149, 1967.
21. A.J. Kelly, "Electrostatic Metallic Spray Theory", *JAP*, **47**, 5264, 1976.
22. A.J. Kelly, "Electrostatic-Spray Theory", *JAP*, **49**, 2621, 1978.
23. A.J. Kelly, "Low Charge Density Electrostatic Atomization", IEEE Trans. Industry Applications, *IA-20*, 2, 267, 1984.

24. SAS Institute — Basic User Manual, Economic Time Series (ETS) User Manuals, available from SAS Institute Inc., SAS Circle, Box 8000, Cary, NC 27512.
25. P.A. Chatterton, R. Holmes, in "Digest of Literature on Dielectrics", 36, 289, 1972, National Academy of Sciences.
26. A. Van Oostrum, Invited papers, 6th International Symposium on Discharges and Electrical Insulation in Vacuum Swansea 49, 1974.
27. J.M. Meek, J.D. Craggs, Eds., Electrical Breakdown of Gases, Chapter 2., Vacuum Breakdown, 129, John Wiley & Sons, Wiley Series in Plasma Physics, 1978.
28. W.F. Brinkman, D.S. Fisher, D.E. Moncton, Science 217, 693, 1982.
29. A.E.D. Heylen, T.J. Lewis, "The Electric Strength and Molecular Structure of Hydrocarbon Gases", Can. J. Phys., 36, 721, 1958.
30. D.P. Brand, "Dielectric Strength, Boiling Point and Toxicity of Gases — Different Aspects of the Same Molecular Properties", IEEE Transactions on Electrical Insulation, EI-17, 5, 451, 1982.

Publications -

Lue, K-M, and Kelly, A.J., "Quadrupole Mass Spectrometer Measurement of Electrostatic Sprays", Electrostatics 1987, pp 337-342, edited by J.L. Sproston, Institute of Physics Conference Series Number 85, Institute of Physics, Bristol, PA.

Lue, K-M, "Fundamentals of Electrostatic Atomization", MS Thesis, School of Engineering & Applied Science, Princeton University, January 1989.

Seneviratne, K.P., "A Real Time Tracker Controlled Electrodynamic Balance", Senior Independent Work Thesis, Electrical Engineering Department, Princeton University, 1988.

Talks -

Lue, K-M, Seventh International Conference on Electrostatic Phenomena, St. Catherine's College, Oxford, G.B., April 1987.

Kelly, A.J., Invited Lectures on Charge Fluids, University of Pisa, April 1987.

Kelly, A.J., Toyota Research Center, Seminar on Charge Fluids, August 1988.

Personnel -

Graduate Students: K-M Lue, J. Whitney
Undergraduate Students: K.P. Seneviratne, P. Chow
Principal Investigators: A.J. Kelly, R.G. Jahn
Staff: G. Miller, D. Tregurtha

Inventions -

none

APPENDIX A

***A REAL TIME TRACKER CONTROLLED
ELECTRODYNAMIC BALANCE***

by

K. Pradeep Seneviratne

ABSTRACT

Implementation of a Electrodynamic Balance to levitate electrostatically charged large liquid droplets is presented. The levitator consists of two horizontally placed electrodes and a nozzle to eject liquid droplets. When a droplet is ejected to the space between the electrodes, a real time Pyramid Tracker determines the position of the center of the droplet. Picture frames of the droplet is recorded by a CCTV camera, and trasfered to the tracker through a VCR. A COMPAQ 386 obtains the position of the droplet from the tracker and using position, velosity, and acceleration feedback determines the appropriate voltage difference required to stabalize the droplet. The voltage differnce between the two electrodes is constantly changed to compensate for the mass loss of the droplet due to evaporation. The ultimate object of the experiment is to observe sibling formation characteristics of the suspend droplet when it evaaporates and loose enogh mass to collapse in to many droplets. Results of the experiment verify that the tracker is fast enough to calculate the center of the droplet up to four times as it travels across the view of the camera. Since the velocities of the droplets in these studies have been comparable to that of ejection velocities of droplets, the tracker is fast enough for the COMPAQ to calculate the required voltage difference between the electrodes. The results of these tests further indicate that, when a fast moving liquid spray is ejected to the space between the electrodes, the tracker is capable of identifiing the number of pixels contained in some of the bigger droplets of the spray. This ability of the tracker is very usefull in studying the process of sibling formation.

ACKNOWLEDGEMENT

I wish to thank my advisor Dr. Arnold Kelly for his guidance and support in carrying out this project. My thanks are extended to Dr. Burt, Dr. Siniger and Dr. Van der Wal for providing me with the necessary equipment, Matt Clark for his valuable advice in writing the tracker routines and George Miller for his help in building the equipment.

This project is sponsored by the Air Force Office of Scientific Research.

TABLE OF CONTENTS

<u>SECTION</u>	<u>PAGE</u>
1.0 Abstract	i
Acknowledgement	ii
Table of Contents	iii
2.0 Introduction	1
3.0 Description and Design of Equipment	5
3.1 Background	5
3.2 Overall System Configuration	6
3.3 COMPAQ 386 to Power Source Interface	6
3.4 Voltage Monitoring System	7
3.5 Electrode Design and Specifications	9
3.6 Multi-purpose Room Temperature Chamber	10
3.7 Modifications of the System	12
3.8 The Fast Response High Voltage Power Supply	14
4.0 Stabilization of the Droplet	18
4.1 Charging and Ejecting the Droplet	18
4.2 Feedback Control Sequence	21
5.0 Summary and Conclusion	23
References	28
6.0 Appendix A - The Vision System	29
6.1 The Pyramid Tracker	29
6.2 Detecting the Center of the Droplet	31
6.3 The Software Listings	35
7.0 Appendix B - Illustrations	82
8.0 Appendix C - Plots	87

INTRODUCTION*

Levitation of electrostatically charged liquid droplets has generated a great deal of interest in recent years because of its possible applications in material processing and its potential usefulness in the understanding of properties of droplets under zero gravity conditions. Containerless processing of materials in space as well as in ground-based laboratories, supercooling and superheating of droplets, dynamics of non-stationary objects, and characteristics of evaporating liquid droplets are some of the applications and experiments of current interest that will require an efficient levitator.

While experiments on large liquid droplets can be performed free from physical contact in space under various conditions, the same experiments are difficult to duplicate on ground due to the fact that the size of the drop to be levitated against one-gravity is limited by its density and surface tension. Levitation of large droplets, up to several millimeters in diameter, has been achieved in wind tunnels since the late 1960's⁸, but such levitated drops invariably suffer from shape distortion due to air drag. Presently, there are two common methods used in levitating liquid droplets without a wind tunnel; unfortunately, both methods have inherent drawbacks as well. In the first method, a droplet is suspended by forces and torques generated by applying

* The first three paragraphs of this chapter was taken from reference 3: a paper written by the author and another student.

acoustic waves on the surrounding medium. It, however, has the disadvantage of requiring a gas medium around the droplet to be suspended. Moreover, a droplet levitated using this technique suffers shape distortion due to forces generated by the acoustic waves¹². The second method employs a RF (radio frequency) field to suspend the droplet. This method can only be used on electrically conductive materials and thus limits the number of liquids which can be used in conjunction with such a levitator.

The method of levitation this paper propose is to suspend the liquid drop by first inducing an electrostatic charge on the droplet, and then launching the droplet into an electric field generated by a pair of horizontal parallel electrodes. The position of the droplet is located by a CCTV (closed circuit television) camera and controlled by a feedback loop to a microcomputer connected to the voltage sources. This method is free from the disadvantages of the above mentioned techniques; therefore, it increases the scope of applications of liquid drop levitators. This type of levitator for a large droplet against 1-g conditions has only been achieved before in the Jet Propulsion Laboratory at California Institute of Technology¹⁰.

The method of levitation of large liquid droplets this paper propose was originally tried out to suspend droplets by the author and another classmate³. This attempt was unsuccessful due to two reasons. Firstly, the frame grabber we used, though was able to digitize frames in real time, the IBM PC-XT we used was not able to process these frames in real time. Thus, our PC-XT was not able to respond fast

enough to change the voltage difference between the two electrodes in order to stabilize the droplet. Secondly, the power supplies we used did not have a fast enough response time. In this experiment I attempted to avoid the first of these two problems by using a Pyramid tracker instead of the frame grabber and the powerful COMPAQ 386 computer instead of an IBM PC-XT. The second problem will be avoided simply by building a very fast response high voltage power supply.

Other than these two major differences and few other modifications in some of the equipment, I will be using the same levitator system for this experiment. Thus, description of system components in the sections 3.0 through 3.6 of chapter 3 was taken directly from the report submitted by me and my class mate(these sections were changed slightly. For instance, instead of the IBM PC-XT, the COMPAQ 386 and instead of the frame grabber the Pyramid tracker are described in these sections.) The modifications I did to the system is explained in the section 3.7 and the fast response power supply is detailed in section 3.8.

Chapter 4 details charging the droplet, ejecting it and the feedback control sequence to stabilize the droplet. Chapter 5 is a summary of the experiment detailing some of the results obtained and the conclusions derived from these results. Appendix A describes the vision system of the system. The main component of the vision system-the pyramid tracker is detailed in this section. Capabilities of the tracker as well as the advantages of using the pyramid tracker instead of a conventional frame grabber are described in section 6.1. In section 6.2 the algorithm used to calculate the

center of the droplet is explained. Section 6.3 contains the software programs which provide information on tracking the liquid droplet.

Much time was spent in obtaining the necessary equipment and understanding and reprogramming the pyramid tracker. Now that the tracker is completely reprogramed to suit this experiment and most of the equipment is built, the electrodynamic balance could be assembled and tested.

DESCRIPTION AND DESIGN OF EQUIPMENT

3.1 Background:

An evaporating liquid droplet suspended in an electrostatic field is in equilibrium under two forces; namely, the gravitational force acting on the droplet and the electrostatic force provided by the two horizontal parallel electrodes. At equilibrium, we have the following equation:

$$V(t)Q/d = m(t)g \quad (i)$$

where: $V(t)$ = Variational voltage difference between the electrodes.

Q = Charge carried by the droplet.

d = Distance between the two electrodes.

$m(t)$ = Variational mass of the droplet.

g = Acceleration of gravity.

Due to the loss of mass from evaporation, $m(t)$ will be a function of time. The rate of mass loss of the droplet depends on such external factors as temperature and humidity of the surrounding medium. When $m(t)$ changes, the voltage difference $V(t)$ has to be changed accordingly to provide a corresponding compensating electrostatic force. Initial hand control of $V(t)$ has been attempted unsuccessfully at the Electric Propulsion Laboratory of Princeton University. In fact, due to the high rate of mass loss as well as the different $V(t)$'s required for the launching and levitating phases of the experiment, it is necessary that the voltage difference be

continuously monitored and varied by means of a computer controlled feedback system.

3.2 Overall System Configuration:

The overall experiment set up is shown in Figure 1 with the main controller and CPU of the system being a COMPAQ 386. The input voltage, $V(t)$, to the levitator is determined by the microprocessor through continuous tracking of the position of the droplet, using an image acquisition system consisting of a CCTV camera, a monitor, a VCR, and a Pyramid tracker built at David Saranoff Research Center. The digitized image by the tracker can be displayed on the monitor in real time for focusing and positioning purposes during the set up phase of the experiment. Once $V(t)$ is calculated by the COMPAQ 386, it is sent to the system's high voltage power supplies via an IBM PC parallel interface board connected to digital-to-analog converters and inverting operational amplifiers. The high voltage power supplies are monitored by a NICOLET oscilloscope, which can dump incoming signal to a Hewlett Packard microcomputer connected to a plotter for voltage vs. time plots. Finally, the appropriate voltage $V(t)$ is sent to the electrodes mounted on a multi-purpose room temperature chamber.

3.3 Microprocessor To Power Source Interface:

The circuit diagram of the microprocessor to high voltage power supply

interface is shown in Figure 2. Since two different power supplies are used for the two electrodes, the output byte of the parallel interface is split into two 4-bit nibbles feeding into two MC1408 8-bit D-to-A converters. The 4 data bits are connected to bits 3, 4, 5, and 6 of the D-to-A, while bits 0, 1, 2, and 7 of the D-to-A are jumpered to ground. This allows each power supply to have 16 possible input control voltage levels. Each D-to-A converter has a $3k\ \Omega$ resistor connected between it and the +5V power supply to provide the necessary drive current and a 1000 pF capacitor connected between it and the -15V power supply for stabilization. The output of D-to-A converters are connected to TL081 inverting differential operational amplifiers, since each D-to-A acts as a current source. The timing of the parallel port is controlled via software delay loops, because D-to-A converters are dumb peripherals that do not take advantage of the status and control ports provided on the parallel communication board. The only line, other than data lines, that is used for interfacing is the BUSY line, which is jumpered to the +5V power supply so it will never be asserted during normal operation.

3.4 Voltage Monitoring System:

To observe the high voltage outputs through the NICOLET, special voltage divider circuits had to be made because the maximum allowable input voltage to the NICOLET is 40V. Since the outputs of the high voltage devices have to be fed into the electrodes as well, two T-junctions were made to interface each of the voltage

devices with the NICOLET and the electrodes. The T-junctions themselves are well covered with epoxy to avoid high voltage discharges. The connection between the high voltage device and the T-junction, as well as the connection between the voltage divider circuit and the T-junction, are both temporary connections, so alligator clamps are used.

It should be noted that even after taking great care in making these connections and grounding the table on which the high voltage devices are placed, it is not possible to avoid minor electric shocks when we touch the table or the room-temperature chamber. Only after suspending all high voltage cables in air using clamps and keeping the cables far away from each other was this experiment performed safely.

The voltage dividers used in our experiment consist of a $400\text{M}\Omega$ resistor in conjunction with a $10\text{k}\Omega$ resistor to produce an approximate 1:40,000 voltage divider for the power supply which control the voltage of the bottom electrode, and a $100\text{M}\Omega$ resistor in conjunction with a $100\text{k}\Omega$ resistor to produce an approximate 1:1,000 voltage divider for the power supply which control the voltage of the top electrode. The $400\text{M}\Omega$ and the $100\text{M}\Omega$ resistors are high quality ceramic resistors. These resistors are necessary since ordinary resistors cannot be guaranteed to retain their specified ohmic values when subjected to high temperatures caused by drastic drops in high voltages. The values $100\text{k}\Omega$ and $10\text{k}\Omega$ are chosen since these are negligible when compared to the input impedance of the NICOLET. The voltage

outputs of the high voltage devices can then be observed by connecting the voltage dividers to the NICOLET as shown in figure 1, and hardcopies of the voltage vs. time plot can be obtained by dumping data from the NICOLET to a Hewlett Packard microcomputer connected to a HP plotter.

3.5 Electrode Design And Specifications:

In this experiment, the concern is stabilization of the liquid drop along the vertical axis, since the electric field created by the parallel electrodes can be utilized to confine the path of the droplet in lateral directions to a reasonable degree. This is easily accomplished by choosing properly shaped electrodes. As a first attempt, a circular convex upper electrode and a matching concave lower electrode was used. The symmetry of the electric field and the strong upward electric force provide the necessary centering force, as the levitated object follows the horizontal potential well along the axis of symmetry. This design was also used in an earlier electrostatic positioner at JPL¹¹. As a direct consequence of equation (i) given earlier, the centering force created by such a pair of electrodes is proportional to $(VQ/dR)X$, where X is the separation between the object and the axis of symmetry, and R is the curvature radius of the electrodes. This type of electrode configuration, however, requires a large constant gravitational force; therefore, it can only be operated in ground-based laboratories.

The electrodes actually used in the experiment are shown in Figure 3. It

follows basically the same design, except for dimensions, as that used in JPL¹⁰, and it was built at the Electric Propulsion Laboratory of Princeton University. The electrodes are a pair of cylindrical aluminum disks. The top ring is tapered to provide the necessary centering force, and both rings are connected to the COMPAQ 386 controlled high voltage power supplies. The electrodes are physically mounted on plexiglas boards that fit into the multi-purpose room temperature chamber used in this experiment. An injection nozzle can be mounted into the chamber through a 0.15 inch opening at the center of the bottom electrode.

3.6 Multi-Purpose Room Temperature Chamber:

The plexiglas levitation chamber used in this experiment was also constructed here at the Electric Propulsion Laboratory. The electrodes described above are mounted at the centers of both the top and the bottom plates of the chamber, and the chamber itself has an inside dimension of 6" x 6" x 1-13/32". At the present time, the multi-purpose room temperature chamber is designed only for the use of suspending a charged droplet; however, it can be easily modified to have the capability of inducing levitated droplet rotation and/or oscillation, like the final version used in the experiment at JPL. The basic method to induce specific motion on an electrostatically levitated droplet is to apply either an acoustic torque² or an oscillating acoustic pressure¹. One possible approach is to have two acoustic transducers mounted on adjacent side walls of the levitation chamber so that

mutually orthogonal acoustic standing waves can be created within the chamber¹⁰. These acoustic transducers can be driven by amplified outputs from two phase and frequency locked synthesizers. Mathematically, we know that the acoustic torque is given by the following equation, according to Busse and Wang²:

$$T = (3/2) l_{\eta} (P_x P_y / 2 \rho c^2) A \sin \phi \quad (\text{ii})$$

where: l_{η} = Viscous length.

P_x = Pressure amplitude of the standing wave in the x-direction.

P_y = Pressure amplitude of the standing wave in the y-direction.

ρ = Density of the medium.

c = Velocity of sound.

A = Surface area of the sphere.

ϕ = Relative phase angle between the orthogonal waves.

Clearly, a varying level of acoustic torque can be produced by either holding the relative phase fixed while varying the sound pressure levels or holding the level of sound pressure constant and adjusting the relative phase. According to Annamalai, Trinh, and Wang¹, we can induce oscillation on a non-rotating liquid droplet by fixing the relative phase at 0° and sinusoidally modulating the amplitude

of the sound wave. Similarly, both rotation and oscillation can be induced at the same time by applying a non-zero relative phase with amplitude modulation. Such a modified chamber can be used to carry out a range of experiments on charged drop dynamics, since surface tension and viscosity of a liquid droplet can be calculated from observations of the oscillating droplet at its natural frequency. One experiment of interest is to observe the behavior of a large evaporating electrically charged liquid droplet near the threshold of Rayleigh's criteria for stability.

3.7 Modifications of the System:

During the experiment which I and my class mate carried out (see introduction) it was observed that after operating the levitator for many hours, the electrodes can no longer be predicted to operate in a consistent manner. To avoid this problem and make the levitator more reliable and efficient, I did the following modifications to the levitator.

a) The reservoir of liquid:

When the levitator is operated for a long time, a considerable amount of liquid from the reservoir is drawn out. After a fair amount of liquid has flown out of the reservoir, the internal pressure acting on the liquid at the tip of the needle will have a different value from before; thus resulting in the need for a new ejection voltage. The solution to this problem is to have a reservoir with a near constant pressure near the tip of the needle at all times. Thus, in place of the fixed reservoir,

a reservoir of liquid which could slide approximately 2" in the vertical direction was installed. Now, by sliding the reservoir the liquid pressure on the tip of the needle can be kept constant.

b.) The position of the needle :

One of the drawbacks that was affecting the levitator was the relatively unstable stand used to hold the needle in position. "After carrying on the experiment for a few minutes, some liquid would accumulate on the bottom electrode. When an attempt is made to wipe out this liquid in order to preserve the surface shape characteristics of the electrode, often the needle would be displaced slightly; hence varying a dimension that should be kept constant if consistent results are to be expected."³

In order to solve this problem, the needle positioning system was designed in the late part of the above mentioned experiment. However the method implemented proved to be of no great promise. Thus, to obtain a stable needle, a clamping mechanism which tightly position the glass tube which leads to the needle was employed. Even when considerable force is employed on the glass tube, this design seems to be able to maintain the needle tip in a stable position.

c) The electrodes:

aluminum rings which supported two central metal coated glass disks. It was observed that after some time this metal coat would wear away leaving behind electrodes of unsuitable surface characteristics. To avoid this problem, aluminum disks were placed in place of the glass disks.

d) The droplet ejection nozzle:

I plan to cover the tip of the ejection nozzle with a non wetting cloth so that surface tension force between the droplet and the needle could be kept to a minimum. Such an arrangement would reduce the voltage necessary to eject a droplet from the needle and consequently the importance of the settling time of the power supply would be reduced. In addition to that, to further reduce the surface tension between water and the needle, small amount of a liquid which would reduce the surface tension of water will be added to the reservoir.

e.) The voltage difference between the electrodes:

In the present configuration of the electrodes, the top electrode is grounded while the voltage of the bottom electrode is kept at an appropriate negative value. It can be shown that under this arrangement, negatively charged droplets ejected from the nozzle, could experience a non converging electric field. By grounding the top

the nozzle, could experience a non converging electric field. By grounding the top electrode and placing an appropriate positive voltage on the bottom electrode this problem could be avoided. However the droplets ejected under this arrangement will be positively charged.

3.8 The Fast Response High Voltage Power Supply :

The circuit configuration of the high voltage power supply is illustrated in figure 4. The Hitachi flyback transformer, produces a high voltage output corresponding to the input voltage at the low voltage section of the power supply, as illustrated in graph 1. There are many advantages of using a Hitachi flyback transformer to generate the necessary high voltage for the electrodes of the levitator. The most important of these is that this transformer is capable of producing an output of 0 to 25kV to a corresponding input voltage with a transient time of approximately 1ms. As seen from graph 1 this output is linear with the input voltage.

The low voltage section of this unit was separated from the high voltage section by enclosing the high voltage section in a metal box. The high voltage transformer is provided with a square wave input. The output of the transformer depends on the magnitude and the frequency of this square wave. Since we need to have the dynamic range of the high voltage output as large as possible the frequency

of the square wave provided to the transformer has to be the resonant frequency of the transformer. The Hitachi flyback transformer resonates around 55kHz, and thus, the frequency of the square wave generated by the NEC 555 oscillator is adjusted to 55kHz.

The amplitude of the square wave determines the output voltage of the transformer. Since the output voltage of the transformer has to be a function of the input voltage to the low voltage section of the power supply, (This input comes from the output of the circuit of figure 3. The output of the circuit of figure 3 is controlled by the COMPAQ 386.) the amplitude of the square wave has to be controlled by this input voltage. The input voltage to the low voltage section of the power supply is first amplified and properly adjusted by means of a buffer amplifier and a level adjuster. This properly scaled input voltage when applied across the clamping diode 1N916, controls the amplitude of the square wave. This controlled square wave is combined with a voltage stabilizing feedback signal at the comparator TL074. The output of the comparator is fed to the primary winding of the flyback transformer to generate the corresponding output voltage. This output voltage of the transformer when properly half-wave rectified and filtered should produce a positive dc voltage with a 1% 55-kHz ripple.¹¹

In addition to the elements shown in the circuit, to obtain a symmetric square wave, the values of R_A and R_B and c have to be properly chosen. According to plot

2 to obtain a square wave of 55kHz frequency, the values of R_A , R_B , and c have to be such that⁷,

$$R_A + 2R_B = 10k\Omega.$$

In addition since t_h and t_L have to satisfy⁷;

$$t_h/t_L = R_B/(R_A + R_B);$$

$$R_A \geq 1k\Omega.$$

and;

$$c \sim .003 \mu F$$

Solving these equations R_A and R_B were taken to be $4k\Omega$ and $2k\Omega$ respectively.

STABILIZATION OF THE DROPLET

4.1 *Charging and Ejecting the Droplet:*

Before the start of the experiment, we have a column of liquid located at the lower section of the injection nozzle. This column is then subject to an electrostatic field produced by the two electrodes, with the bottom electrode being negatively charged with respect to the top electrode. Since the liquid column is in contact with the reservoir, the relatively positive top electrode will cause the liquid column to be induced with a negative charge. The mutual attraction between the top electrode and the negatively charged liquid column, as well as the liquid pressure acting on the column produced by a reservoir located at a higher level than the tip of the nozzle, will cause the column to flow toward the tip of the needle.

At the tip of the needle, the first speck of liquid which attempts to eject itself out from the nozzle toward the top electrode will be stopped from doing so by the surface tension between the needle and itself. Thus, a small amount of liquid will accumulate at the top of the ejection needle. This droplet of liquid will gather more and more negative charge due to the influence of the positive top electrode. Invariably, such an accumulation of charge will lead to more liquid being pushed to the top of the needle. This charge will cause an ever increasing electrostatic force to *push* the now bigger and highly charged droplet upwards. When this force is large enough to overcome the surface tension between the droplet and the needle, a spherical droplet will be observed

to leave the tip of the needle.

As mentioned before, I and my class mate tried out numerous control algorithms in an earlier experiment to stop the droplet from reaching the top electrode after its ejection from the needle. During that experiment we found a particular algorithm that is capable of stopping droplets from reaching the top electrode. That algorithm is as follows³:

- (1) Provide a control voltage of known magnitude to the bottom electrode.
Provide the control voltage long enough so that the output of the power supply will reach a constant value and will remain at that value for a few seconds. (The method we used to observe the outputs of the high voltage devices is outlined in the section *Voltage Monitoring System*.)
- (2) Increase the control voltage to the power supply. Let the computer run through a loop of few useless instructions to allow the power supply to reach an ejection voltage. (Note that once a control voltage is fed into the power supply, even if the computer goes through a wait loop, the control voltage to the power supply will remain the same, since data is latched into the parallel port of the PC. To change the control voltage, another control voltage must be explicitly fed into the power supply.)
- (3) Provide a zero control voltage to the power supply.
- (4) While steps 1, 2, and 3 are being executed, apply a zero voltage to the top electrode. As soon as step 3 is executed, apply a large control voltage to the

top electrode.

- (5) Wait for a few seconds and then provide a zero control voltage to the top electrode.
- (6) Repeat steps 1 through 6.

The function of the individual steps in this algorithm is as follows:

- (1) Provide voltage large enough to bring up a droplet to the needle tip and provide enough charge to that droplet so that if a higher voltage is applied (in the next step), the droplet will be ejected from the needle. It is important not to provide too big a voltage in this step since we do not want the droplet to be ejected while this step is being carried out. We had to experiment with the levitator for a while before selecting such a control voltage.
- (2) Provide a higher control voltage so that the droplet will be ejected. It is important that the time spent on the wait loops is not too long, for what we want is to provide just the ejection voltage and no more.
- (3) Switch off the voltage supply to the bottom electrode so that the voltage on this electrode will decay to zero.
- (4) While the above steps are being performed, the voltage on the top electrode should be zero. Step 3 will eject a droplet. Thus, by supplying a large control voltage to the power supply immediately after step 3, we will repel the ejected droplet from the top electrode.

- (5) Wait to make sure that the droplet is stopped and shut off the voltage to the top electrode.
- (6) Start again to eject another droplet.

While executing this program, we observed that after ejection, the droplet would travel up, reach zero velocity, and then fall back. I hope to use this same algorithm to charge, launch and stop the droplet from reaching the top electrode.

4.2 Feedback Control Sequence:

Since there are 4 bits of data, which can easily be expanded into 8 bits by sending out separate controlling signals to the top and the bottom electrodes, for each power supply at disposal, a range of control algorithms are available for stabilizing the droplet. The obvious extension from a bang-bang control is a simple proportional control scheme, where variable control voltages are sent to the electrodes, depending on the actual position of the drop within the frame rather than its presence in a particular region. Furthermore, if the velocity of the droplet can be measured based on the previous position of the droplet, a straight forward PID, i.e. proportional-integral-derivative, control algorithm can be implemented to model a simple second-order linear feedback system. The relationship in discrete form that governs such a control algorithm is as follows:

$$S[n] = G_p E[n] + G_i \left(\sum_{j=0}^n E[j] \right) + G_d (E[n] - E[n-1]) \quad (\text{iii})$$

where: $S[n]$ = Output at n^{th} sample time.

$E[n] = P_d - P[n]$ = Position error.

P_d = Desired position in pixels.

$P[n]$ = Actual position in pixels at n^{th} sample time.

G_p = Proportional gain.

G_i = Integral gain.

G_d = Derivative gain.

One advantage that the PID control does have over the simple bang-bang control is greater flexibility, where various design tools, such as root-locus, Nyquist, or Bode plots can be used to pick the desired gains for different situations.

SUMMARY AND CONCLUSION:

Success of this project depends on two major capabilities of the levitator system. The first is the capability of the high voltage power source to have a fast enough decay time such that the droplet will not hit the top electrode. This means that the power supply has to have a very fast transient time. The second is the capability of the image processor of the system to process frames fast enough so that the COMPAQ 386 could control the voltage difference between the two plates fast enough to stabilize the droplet.

The first of these two problems will be avoided, as mentioned before by building a fast response high voltage unit. If the transient time of the power supply is within its guaranteed range of 1ms, then this power supply would certainly be fast enough for our purpose. The low voltage section and the control section of the power supply has been already built. Building the high voltage section of the power supply has been halted due to the delay in obtaining a high voltage transformer and lack of vital information regarding the outlets of this high voltage transformer. Once this information is available the power supply can be built and tested for its transient time.

One of the major major problems of the above mentioned experiment carried out by me and my classmate, was that once the droplet is stopped by the top electrode after its ejection, the droplet showed a lateral movement in its falling trajectory. The reason for this movement, we then believed, was that the top electrode causing too

great a damping force to the oncoming droplet. Since we were able to provide only 16 different control voltages, at that time, to the power supply, we could not achieve the exact damping force that was necessary to smoothly turn back the oncoming droplet. however, if the power supply which I am in the process of building prove to have a fast enough transient time, there is no need to control the voltage of the top electrode. In this case not only can we avoid the problem of top electrode diverting the droplet, but we will also be able to control the bottom electrode with 256 different control voltages levels.

The second of the major concerns of the project has been avoided by using the Pyramid tracker as the image processor of the system. The capabilities of the tracker and how these capabilities are modified so that the tracker functions as a real time frame grabber are detailed in Appendix A. Results of some of the tests performed to determine the speed at which the tracker could calculate the center of the droplet are outlined below.

In these experiments a reservoir of liquid was placed at a considerable height above the view of the camera. The liquid in the reservoir is water-colored by mixing with black ink. A small hole was punched in the bottom of the reservoir so that very small liquid droplets would emanate from this hole and fall down passing the view of the camera. It should be noted that the vertical distance between the camera and the bottom of the reservoir is such that the droplet will pass the view of the camera at a considerable velocity. This was necessary if we are to determine whether the tracker

is capable of detecting a fast moving droplet. (Note that the tracker has to detect the droplet when the droplet is ejected, and that at the time of ejection the droplet has a considerable velocity.)

The results of the experiment indicated that the tracker was capable of calculating the center of the droplet upto four times while the droplet was moving across the view of the camera. Note that for velocity feedback control of the droplet as explained in chapter 3, the tracker has to detect the droplet only 2 times. Thus, the tracker is certainly fast enough for the purpose of this experiment.

One of the other experiments carried out to determine the capabilities of the tracker is as follows. The reservoir of liquid was brought closer to the camera and a metal needle was connected to the reservoir of liquid by a glass tube. The glass tube is also connected to a high voltage power supply. Thus, when the power supply is turned on it will inject charge to the liquid resulting in a spray of liquid at the mettles needle. Depending on the output voltage of the power supply and the diameter of the needle the size distribution of the droplets in the spray could be varied. The tracker was initialized at the beginning of the experiment such that the frame obtained from the camera contains no pixel above a prescribed threshold value. (The process of doing this is explained in Appendix A) It is interesting to note that when the needle was spraying the liquid in the view of the camera the tracker was able to identify the total number of pixels which are above the threshold value. This capability of the tracker is vital in observing the sibling formation characteristics of liquid droplets. For, by

programming the tracker to group all the pixels which are adjacent to each other and which are above the threshold value we can determine the number of droplets and the size distribution of these droplets when an evaporating droplet collapses into many droplets.

Note that to calculate the center of a fast moving droplet the tracker has to calculate the center of the droplet at least twice and thus be programmed to operate in Pyramid levels 1 or 2. (See Appendix) The need in this application is then, to have a very fast image processor at the expense of great resolution. To calculate the number of siblings formed when a bigger droplet collapses, the tracker has to be able to identify whether a group of pixels is separated from another group of pixels and thus have to be programmed to operate in Pyramid levels 5 or 6. The need here is to have a image processing system of high resolution at the expense of speed. Note that I was able to program the same tracker to switch between speed and resolution. In this respect perhaps the Pyramid tracker is the only single image processor which is capable of successfully stabilizing a droplet and obtain information on sibling formation.

The effectiveness of the modifications done to the electrodes, reservoir, and the injection needle will be revealed only when the actual experiment is carried out. Much time was spent in trying to obtain the necessary equipment, understand the Pyramid tracker and reprogramming it to suit the purpose of this experiment. Now that the tracker has been completely modified and tested for its capabilities, with positive

results, once the high voltage power supply is built the actual experiment of attempting to suspend large liquid droplets could be carried out.

REFERENCES

- [1] Annamalai, P.; Trinh, E.H.; and Wang, T.G., "Experimental Studies of the Oscillation of a Rotating Drop," *J. Fluid Mechs.*, Vol. 158, 1985, pp. 317.
- [2] Busse, F.H. and Wang, T.G., "Torque Generated by Orthogonal Acoustic Waves Theory," *J. Acoust. Soc. Am.*, Vol. 69, 1981, pp. 1634.
- [3] Chow, P.S., Seneviratne, K.P., "Microprocessor Controlled Levitation of an Electrostatically Charged Liquid Droplet," *ELE 418 Project Report, Department of Electrical Engineering, Princeton University, Princeton, New Jersey*, 1987.
- [4] Doyle, Arnold; Moffett, D. Read; and Vonnegut, Bernard, "Behavior of Evaporating Electrically Charged Droplets," *Journal of Colloid Science*, Vol. 19, 1964, pp. 136 - 143.
- [6] Lindblad, N.R., and Schneider, J.M., "Method of Producing and Measuring Charged Single Droplets," *The Review of Scientific Instruments*, Vol. 38, Number 3, March, 1967, pp. 325 - 327.
- [7] Linear Circuits Data Book, Texas Instruments, Dallas, Texas, 1984
- [8] Pruppacher, H.R., and Beard, K.V., "A Wind Tunnel Investigation of the Internal Circulation and Shape of Water Drops Falling at Terminal Velocity in Air," *Quart. J. Roy. Meteor. Soc.*, Vol. 96, 1970, pp. 247.
- [9] Rayleigh, "On the Equilibrium of Liquid Conducting Masses Charged with Electricity," *Phil. Mag.*, Vol. 14, pp. 184-186.
- [10] Rhim, Won-Kyu; Chung, San Kun; Trinh, Eugene; Hyson, Michael T.; and Elleman, Daniel D., "Large Charged Drop Levitation Against Gravity," *IEEE - CH2272 (Jet Propulsion Laboratory, California Institute of Technology)*, 1986, pp. 1338 - 1341.
- [11] Rhim, Won-Kyu; Collender, M.; Hyson, Michael T.; Simms, W.T.; and Elleman, Daniel D.; "Development of an Electrostatic Positioner for Space Material Processing," *The Review of Scientific Instruments*, Vol. 56, Number 2, February, 1985, pp. 307 - 317.
- [12] Rhim, Won-Kyu; Saffren, Melvin M.; and Eleman Daniel D., "Development of Electrostatic Levitator at JPL," *Proceedings of Material Processing in Reduced Gravity Environment of Space*, edited by Guy E. Rindone, Elsevier Science Publishing Company, Inc., 1982, pp. 115 - 119.

APPENDIX A - THE VISION SYSTEM

6.1 THE PYRAMID TRACKER

The Pyramid Tracker is a real time frame grabber which can be programmed to operate in 6 "Pyramid levels". A Pyramid level identifies a frame transferred by a camera as a picture consisting of following number of pixels,

Pyramid level	width x length of the picture in pixels
1	7 x 8
2	15 x 16
3	30 x 32
4	60 x 64
5	120 x 248
6	240 x 256

The advantage of having Pyramid levels is the ability to analyze objects in different resolution levels and at different speeds. For instance, if we want to stop a fast moving droplet from reaching the top electrode, we need to know its position, velocity, and acceleration in a short time. In this case, identifying the droplet with

good resolution is unnecessary. Thus, by considering the whole frame transferred by the camera as a 7×8 pixel picture the position of the droplet can be calculated in a maximum of 56 instructions. To perform the same calculation in Pyramid level 6 a maximum of 61,440 instructions have to be performed. Now, consider observing the droplet at the moment of sibling formation with the objective been observing the number of droplets and their size distribution. It is obvious that in this case, to identify the correct number of siblings and to identify the size of these droplets with a high degree of accuracy, we need to capture only one high resolution frame. Thus, for this application the number of frames the tracker can process per second is of no concern. In this case, there are two advantages of using Pyramid level 6 over Pyramid level 1. The first is, by dividing the frame transferred by the camera into a grid consisting of 240×256 pixels the size of the individual droplets can be measured with high precision. The second is, by dividing the picture into many pixels, even the very small droplets can be identified.

Note that it is possible to stabilize the droplet using Pyramid level 1, and then once the droplet is stabilized, the droplet and its immediate surrounding area can be scanned using Pyramid level 6. Thus, by using the Pyramid tracker the need to have two frame grabbers and supporting equipment-- A fast frame grabber to suspend the droplet, and a high resolution frame grabber to observe sibling formation -- can be avoided.

There is another advantage of using the Pyramid Tracker instead of a

Note that it is possible to stabilize the droplet using Pyramid level 1, and then once the droplet is stabilized, the droplet and its immediate surrounding area can be scanned using Pyramid level 6. Thus, by using the Pyramid tracker the need to have two frame grabbers and supporting equipment-- A fast frame grabber to suspend the droplet, and a high resolution frame grabber to observe sibling formation -- can be avoided.

There is another advantage of using the Pyramid Tracker instead of a conventional frame grabber for this experiment. When I was attempting to suspend a droplet using a 30 frames per second frame grabber³, though the frame grabber was transferring 30 frames per second to the IBM-XT processor, the XT was able to process only 6 frames per second. Thus, not counting the time it would take to calculate the necessary voltage difference between the two plates, the XT would take 1/5s to respond to a frame transferred by the camera. As will be explained in the next section, by taking advantage of the special features of the tracker, the COMPAQ 386 could respond to a frame transferred by the tracker in 1/30s: a six fold increase in the response time of the feedback loop.

6.2 DETECTING THE CENTER OF THE DROPLET

The following algorithm was used to calculate the center of the droplet in the two experiments explained in the last section. This same algorithm can be used to calculate the center of the droplet in the actual experiment.

The basic algorithm used in calculating the center of the droplet is as follows.

V1, V2 and V3 are integer variables with zero initial value.

- 1) Paste bright white paper to the interior walls of the room temperature chamber. Now illuminate the inside of the chamber. By constantly checking the highest grey leveled pixel in the frame, (the tracker should be operated in Pyramid level 6 to maximize the resolution. The gray level of a pixel can be directly obtained from the tracker by giving the address of that pixel.) provide light to the chamber until the highest grey level found in the frame is a minimum. Note this threshold level T1. At this time fix the position of the illuminators. The light intensity level inside the chamber must not be varied hereafter.
- 2) Now select a threshold level for the droplet. This threshold level is such that it is slightly higher than T1. Thus, if we now ask the tracker to find pixels whose grey level is above the threshold value the tracker should not be able to find any such pixels. Program the tracker to await, expecting a droplet.
- 3) Since the water in the reservoir has been colored black, if a droplet of this liquid appears in the view of the camera now, the tracker should detect some pixels above the threshold value. program the tracker to check each pixel of the frame starting from the upper left hand and all the way upto the upper right hand corner. At the end of this row the tracker will start checking the pixels starting from the left hand corener of the second row. This process continues untill the

tracker has checked all the pixels. All the pixels in the first row have x address 1 and all the pixels in the second row have x address 2 etc. Thus, in Pyramid level 6, the x address of any pixel in the last row is 240. Similarly the y address of any pixel in the first column is 1

- 3) If a pixel is encountered above the threshold value increment V1. Add the x address of this droplet to V2 and y address to V3. Repeat this procedure for all the pixels in the frame.
- 4) At the end of the frame divide the value in V2 by V1 and V3 by V1. This gives the approximate x and y coordinates of the center of the droplet.

There is actually no need to scan the whole frame to look for the position of the droplet. Once we determine the x and y coordinates of the center of the droplet from the first frame, to track the droplet thereafter, though we need to scan all the horizontal lines, only few of the vertical lines need to be scanned. As the droplet stabilizes we need not scan all the horizontal lines either. In this manner the COPMAQ has more time to spend for the feedback loop.

Another feature was incorporated into this algorithm. While scanning the image if we encounter high grey level pixels that implies that the tracker is currently scanning the droplet. In such a case, if we started scanning from the top, and if we do not encounter any high value pixel for an entire horizontal line that means that we have completely scanned the droplet. In this case we can stop scanning the droplet and start calculating the necessary control voltages to the power supplies etc. Hence by

using this method the COMPAQ has more time to spend on calculating the feedback outputs.

6.3 The Soft Ware Listings:

Listed below are the general software routines which the tracker requires, and the special purpose routines which are required to detect the droplet. The programs in pages 37 - 44 were written by me. The rest of the programs were originally written by Dr. Van der Wal of David Sarnoff Research Center and modified by me to best suit the purposes of this experiment.

Modules cursor.c and reg.c contains propriety information of RCA Corporation and should be treated as confidential.

<u>TITLE AND FUNCTION OF THE PROGRAM</u>	<u>PAGE</u>
Initializes pyramid microcode memory after power on	37
makefile - makefile for main.c and gaus.h	38

gaus.h - Gaussian pyramid header module	39
main.c - Generate gaussian pyramid. Calculate the center of the droplet. Determine the required voltage difference between the two electrodes to stabilize the droplet.	41
makefile - makefile for ips directory	45
bus.c - Image processing system drivers	46
cursor.c - mouse functions	48
gfx.c - Graphical utilities	54
ips.c - image processing system drivers	59
ips.h - macros for standard ips routines	62
key.c - For input/output directed through the keyboard	65
reg.c - Functions for register reading and writing	68

screen.c - Input/output functions and functions to

display the screen

71

state.c - Functions to manipulate programs in ips

75

wr.c - writes code from 'file.q' to control board

79

#_Script Gaus setup microcode to run tracker
#_Initializes pyramid microcode memory after power on

cpy -ab < gp4.q | cpy -dm 0x2000 0x1000 1
gaus

SRC=main.c
OBJ=main.o
CFLAGS=-i -Mse2 -O
NAME=gaus
EXE=\$(NAME)
ARCH=../ips/ips.a
LIB=

\$(EXE): \$(OBJ) \$(ARCH)
cc \$(CFLAGS) -o \$(EXE) \$(OBJ) \$(ARCH) \$(LIB)

lint:
lint -a -x \$(SRC) > 1

wc:
wc \$(NAME).h \$(SRC) makefile

purge:
/bin/rm \$(OBJ) \$(EXE)


```

/* file:  gaus.h
   desc:  gaussian pyramid header module
   date:  11/12/87 msc
   mod:   11/12/87 msc

*/

/* include file */

#ifdef M_XENIX
#include "../ips/ips.h"
#else
#include "../ips/ips.h"
#endif

/* NULL fix */

#ifdef NULL
#undef NULL
#endif
#define NULL 0

/* macro function redefinitions */

#ifdef M_XENIX
#define IP_ADDR(offset)    (ips_base[(offset) >> 8] ; ((offset) & 0xffff))
#define IP_PGM(staddr)    ioctl(ipd,'p',staddr)
#else
#define IP_ADDR(offset)    (ips_base + (offset))
#define IP_PGM(staddr)    ips_pgm(staddr)
#endif

/* macro constants */

#define TRK_X    16      /* width of tracker window */
#define TRK_Y    15      /* height of tracker window */

/* structure for pyramid constants */

struct pyrlevel {
    short uix,uiy,          /* (xl,xh),(yl,yh) offset registers */
          unx,uny;         /* image size in (x,y) directions */
};

struct tblock {
    short xmean,ymean;      /* sum of x, sum of y */
    short numpix;           /* number of pixels > thr */
    short pixsum;           /* sum of pixels > thr */
    short x,y;              /* x and y offsets within level */
    struct pyrlevel *pp;    /* pointer to pyramid level */
};

/* static global variables */

struct pyrlevel Pyr[6];    /* pyramid constant values */

```

```
/* external functions */
```

```
/* main.c */
```

```
int main();
```

```

/* file: main.c
   desc: generate gaussian pyramid
   func: main(argc,argv)
   date: 11/01/87 msc
   mod:  11/06/87 msc

*/

#include <stdio.h>
#include "gaus.h"

/* static global variables */

struct pyrlevel Pyra[] = {
    { 7, 3, 256, 240 }, /* |G0| */
    { 277, 0, 128, 120 }, /* |G1| */
    { 279, 121, 64, 60 }, /* |G2| */
    { 281, 182, 32, 30 }, /* |G3| */
    { 283, 213, 16, 15 }, /* |G4| */
    { 285, 278, 8, 8 } /* |G5| */
};

/* func: main(argc,argv)
   desc: controller function
   args: <none>
   ret: (int) 0 == successfull
        . == error
*/

main(argc,argv)
int argc;
char *argv[];

{
    register short pix,
        thr,
        xx;
    register pointer bp;
    short numpix = 0,
        pixsum = 0,
        xoff = 0,
        yoff = 0,
        deep = 0,
        pixoff = 0,
        xmean,
        ymean,
        yy,
        xcenter,
        ycenter,
        dxcenter,
        dycenter,
        i,
        j,
        k;
    byte st1[64],
        st2[64];

```

```

struct tblock blockB,
    *B;
struct pyrlevel *pp;

/*  initial values  */

for (i = 0; i < 5; i++)                /*  pyramid loc's          */
    Pyr[i] = Pyra[i];
if (!ips_init())                        /*  image processing system */
    exit(1);

/*  arguments          */

for (i = 1; i < argc; i++) {
    if (argv[i][0] == '-') {
        for (j = 1; j < strlen(argv[i]); j++)
            switch (argv[i][j]) {
                case '1':                /*  camera 1 (default)      */
                    break;
                case '2':                /*  camera 1 (default)      */
                    camera = 0x20;
                    for (k = 0; k < 4; k++)
                        apcval[k] |= camera;
                    *apc = apcval[0];
                    break;
                default:
                    fprintf(stderr, "invalid flag  '-%c\n", argv[i][j]);
            };
    } else
        fprintf(stderr, "invalid argument  '%s'\n", argv[i]);
};

/*  input lookup table
    input LUT 1,2:  linear
    input LUT 3:    inverse linear  */

for (i = 1; i < 4; i++) {
    *apc = apcval[0];  *slut = slutval[i];
    for (j = 0; j < 256; j++) {
        *alut = (byte) j;
        *dlut = (i != 3) ? j : 255 - j;
    };
};

/*  output lookup tables          */

for (i = 0; i < 3; i++) {
    *apc = apcval[i + 1];  *slut = 0xaa;
    for (j = 0; j < 256; j++) {
        *alut = (byte) j;
        *dlut = j;
    };
};

/*  control registers
    set:  camera->pyr->(v0a,v0b & v2a) */

*(v0 + ctrl) = *(v1 + ctrl) = *(v2 + ctrl) = 0x47;    /*  256x240          */
*ab = 0x44;  *cd = 0x34;  *e = 2;  *out = 0x07;        /*  paths            */

```

```

*alu = 0x03; /* alu A+B */
*(v0 + ctrh) = 0x0c; /* cont grab */
*slut = 0x55; /* linear lut */

/* initialize state variable program */
/* To show G0 - use v2.ctrh=0x08 when sst==0 */
/* To show Gn - use v2.ctrh=0x08 when sst==1 */

if (!st_encode(st1,"sst!=1 sst==1 v0.pan=0x100"))
    exit(1);
if (!st_encode(st2,"sst!=0 sst==0 v0.pan=0x000 v2.ctrh=0x08"))
    exit(1);

/* initialize blocks */

B = &(blockB);
B->pp = &(Pyr[4]);
B->x = B->y = 0;
for (i=0;i < 18;i++)
    printf("                \n");
printf("                GAUSSIAN PYRAMID TRACKER 11/12/87\n");
printf("                \n");
printf("                \n");
printf("Press Ctrl/Backspace to stop tracker\n");
printf("                \n");
printf("Initializing tracker. Keep off from the view of the camera.\n");
printf("                \n");

/* write .q microcode program to buffer

#ifdef NOT_NOW
if (!wrips("gp4.q"))
    exit(1);
#endif */

pp = B->pp; /* this and next line were taken from loop */
d0 = d0 + DELY * (long)(pp->uiy + B->y) + (pp->uix + B->x);

/* loop forever and determine the center of the droplet */

fb = d2;
while (TRUE) {
    IP_PGM(st1);

    /* do calculations here . . . */

    IP_PGM(st2);
    bp = d0;
    xmean = ymean = numpix = pixsum = 0;
    for (yy = TRK_Y; yy; yy--) {
        for (xx = 16; xx; xx--)
            if ((pix = *(bp++)) > 20) {
                numpix++;
                pixsum += pix;
                xmean += xx;
                ymean += yy;
                printf("%d\n",pix);
            };
        bp += DELY - TRK_X;
    };
};

```

```

if (deep == 700) {
    deep = 701;
    printf("                                TRACKER  READY\n");
}
if ( deep == 701) {
    numpix = numpix - pixoff;
    if (numpix > 0 ) {
        ycenter = (ymean - yoff)/ numpix;
        ycenter = 16 - ycenter;
        dycenter = 240*ycenter/15;
        xcenter = (xmean - xoff)/ numpix;
        xcenter = 17 - xcenter;
        dxcenter = 256*xcenter/16;
    }
}

if (deep < 700) {
    xoff = xmean;
    yoff = ymean;
    pixoff = numpix;
    deep = deep +1;
}

drawline(dxcenter -3, dycenter,dxcenter +3,dycenter,255);
drawline(dxcenter,dycenter +3, dxcenter,dycenter - 3,255);
};

/* ips_close();
return(0);  */

}

```

SRC=bus.c cursor.c gfx.c ips.c key.c reg.c screen.c state.c wr.c
OBJ=bus.o cursor.o gfx.o ips.o key.o reg.o screen.o state.o wr.o
CFLAGS=-i -Mse2 -O
NAME=ips
ARCH=ips.a
LIB=

\$(ARCH): \$(OBJ) \$(OBJ)
 ar ru \$(ARCH) \$(OBJ)
 ranlib \$(ARCH)

lint:
 lint \$(SRC) > 1

wc:
 wc \$(NAME).h \$(SRC) makefile

purge:
 /bin/rm \$(OBJ) \$(ARCH)

```

/* file: bus.c
   desc: image processing system drivers
   func: bus_init()
         bus_close()
   date: 07/02/87 msc
   mod:  10/29/87 msc
*/

#include <stdio.h>
#include <fcntl.h>
#include "ips.h"
#ifdef M_XENIX
#include <sys/hwdbus.h>
#include <sys/ioctl.h>
#endif

/* func: bus_init()
   desc: initialize hardware bus
   args: <none>
   ret:  bool:  FALSE = error
         TRUE  = successfull
*/

bool
bus_init()
{
    byte b;
    pointer bp;
#ifdef M_XENIX
    struct hwdbase pb;
#endif

    /* open image processing system as file descriptor */

#ifdef M_XENIX
    /* open bus device */

    if ((ipd = open("/dev/bus",O_RDWR)) == ERR) {
        fprintf(stderr,"cannot open bus\n");
        return(FALSE);
    };

    /* get base address */

    if ((ioctl(ipd,HWDBASE,&pb)) == ERR) {
        fprintf(stderr,"ioctl error\n");
        return(FALSE);
    };
    ips_base = (byte *) pb.hwdmem + 0x00a00000L;

    /* wake up hardware */

    b = *(pb.hwdio + 0x0200);
#else
    /* open bus device */
    if ((ipd = open("/dev/ip",O_RDWR)) == ERR) {
        fprintf(stderr,"cannot open device '/dev/ip\n");[

```



```

    return(FALSE);
};

/*  get initial segment descriptor - 'inquiry'  */

if (ioctl(ipd, 'i', &ips_base)) {
    fprintf(stderr, "cannot access '/dev/ip'\n");
    return(FALSE);
};
#endif

/*  read and write a test byte  */

bp = ips_base + 0x10;    b = *bp;
*bp = 0x00;
if (*bp != 0x00) {
    fprintf(stderr, "could not access image processing system\n");
    return(FALSE);
};
*bp = 0xff;
if (*bp != 0xff) {
    fprintf(stderr, "could not access image processing system\n");
    return(FALSE);
};
*bp = b;

return(TRUE);
}

/* func:  bus_close()
   desc:  terminate bus interface parameters
   args:  <none>
   ret:   <void>
*/

void
bus_close()
{
    if (close(ipd) == ERR)
        fprintf(stderr, "error closing bus\n");
}

```

```

/* file: cursor.c
   desc: mouse functions
   func: cursor_init()
         cursor_close()
         rawxy(buttons,mx,my)
         isbut()
         getxy(mx,my,func)
         drawcursor(mx,my,func)
   date: 07/07/87 msc
   mod:  11/29/87 msc
*/

#include <stdio.h>
#include <fcntl.h>
#ifdef M_XENIX
#include <termio.h>
#include <sys/ioctl.h>
#else
#include <sys/hft.h>
#endif
#include "ips.h"

/* macro constants */

#define MAX_CURSOR_X 8 /* mouse cursor size */
#define MAX_CURSOR_Y 14

#define CURSOR_ERASE FALSE /* flags sent to cursor_draw() */
#define CURSOR_DRAW TRUE

#ifdef M_XENIX
#define MOUSE_DEVICE "/dev/ttyla" /* mouse device i/o name */
#define MAX_RETRIES 500 /* max number of error retries */
#endif

/* static variables */

#ifdef M_XENIX
static char mousectrl[] = { ESC, '[', 'x', NULL, NULL, NULL, 0x0e, HFKSRPROH,
                           HFKSRPROL, 0x04, NULL, NULL, NULL, NULL, 0x80, NULL, 0x80,
                           ESC, '[', 'x', NULL, NULL, NULL, 0x0c, HFLOTHCH,
                           HFLOTHCL, 0x02, NULL, NULL, 0x02, NULL, 0x02 };
#endif

/* func: cursor_init()
   desc: initialize mouse cursor
   args: <none>
   ret:  bool: FALSE == unsuccessfull
         TRUE == successfull
*/

bool
cursor_init()
{
#ifdef M_XENIX
int i;
byte b = ' ';

```

```

static struct termio ttmouse;          /* for communication line */

if ((mfd = open(MOUSE_DEVICE,O_RDWR | O_NDELAY)) == ERR) {
    fprintf(stderr,"could not open '%s'\n",MOUSE_DEVICE);
    return(FALSE);
};

ttmouse.c_iflag = 0;  ttmouse.c_oflag = 0;  ttmouse.c_lflag = 0;
ttmouse.c_cflag = B1200 | CS7 | CSTOPB | CREAD | PARENB | CLOCAL;
if (ioctl(mfd,TCSETA,&ttmouse) == ERR) {
    fprintf(stderr,"could not ioctl info\n");
    return(FALSE);
};

for (i = 0; i < MAX_RETRIES; i++) {
    if (write(mfd,&b,1) == -1) {
        fprintf(stderr,"could not write to mouse\n");
        return(FALSE);
    };
    if (rdchk(mfd))
        break;
};
if (i == MAX_RETRIES) {
    fprintf(stderr,"mouse is not attached\n");
    return(FALSE);
};
#else
    write(tfd,mousectrl,32);
#endif

return(TRUE);
}

/* func:  cursor_close()
   desc:  close cursor routine
   args:  <none>
   ret:   <void>
*/

void
cursor_close()
{
#ifdef M_XENIX
    close(mfd);
#else
    mousectrl[16] = NULL;
    write(tfd,mousectrl,17);
    close(tfd);
#endif
}

/* func:  rawxy(buttons,mx,my)
   desc:  returns raw mouse data
   args:  short *buttons,          * button status - 0x01 and 0x02 *
          *mx,*my;                * relative mouse values      *
   ret:   (bool):  FALSE == error
          TRUE == successfull
*/

```

```

bool
rawxy(buttons,mx,my)
short *buttons,
*mx,
*my;
{
    short r;
    static short blast;
#ifdef M_XENIX
    static char ch[3],
    t;
    static short n;

/*    clear old values    */

*buttons = blast;    *mx = *my = 0;

/*    wait for new value(s)    */

while ((r = read(mfd,ch + n,1)) == 1) {
    switch (n) {

        case 0:  if (ch[0] < '@')
                    continue;
                    t = (ch[0] & 0x0f);
                    if ((t != 0x00) && (t != 0x03) && (t != 0x0c) && (t != 0x0f))
                        continue;
                    break;

        case 1:  if (ch[1] >= '@') {
                    ch[0] = ch[n];
                    n = 0;
                    continue;
                };
                if (((t & 0x03) ^ !(ch[1] & 0x20)) == 1) {
                    n = 0;
                    continue;
                };
                break;

        case 2:  if (ch[2] >= '@') {
                    ch[0] = ch[n];
                    n = 0;
                    continue;
                };
                if (((t & 0x0c) ^ !(ch[2] & 0x20)) == 1) {
                    n = 0;
                    continue;
                };
            };
        if (++n < 3)
            continue;
        n = 0;
        *buttons = blast = (ch[0] >> 4) & 0x03;
        *mx = ch[1] - ((ch[1] & 0x20) << 1);
        *my = ch[2] - ((ch[2] & 0x20) << 1);
        return(TRUE);
    };
    if (r == -1) {

```

```

    fprintf(stderr,"trouble reading mouse");
    return(FALSE);
};
#else
/*  check input queue  */

iskey();

/*  clear old values  */

if (mqbegin == mqend) {
    *buttons = blast;    *mx = *my = 0;

/*  wait for new value(s)  */

} else {
    blast = *buttons = mqbegin->buttons;
    *mx = mqbegin->dx;
    *my = -mqbegin->dy;
    if (++mqbegin >= mqueue + MAX_QUEUE)
        mqbegin = mqueue;
};
#endif

return(TRUE);
}

/* func:  isbut()
   desc:  returns button value
   args:  <none>
   ret:   (bool):  button up (FALSE) or down (TRUE)
*/

bool
isbut()
{
    short buttons,mx,my;

    if (rawxy(&buttons,&mx,&my))
        return(buttons != NULL);
    return(FALSE);
}

/* func:  getxy(mx,my,func)
   desc:  gets x & y coordinates
           draws cursor on screen
           returns when left or right button is pressed
   args:  (int) *mx,*my;          * x & y values *
           (int) func;            * type of function *
   ret:   short:  button value
*/

short
getxy(xx,yy,func)
short *xx,
*yy;
short func;
{
    short buttons,
    but,

```

```

    height,
    width,
    dx,
    dy,
    oldx,
    oldy;
static short mx,
    my;

/* flush cursor input stream */

if (func == CURSOR_FLUSH) {
    if (!rawxy(&buttons,&dx,&dy))
        return(NULL);
    do {
        but = buttons;    height = dx;    width = dy;
        if (!rawxy(&buttons,&dx,&dy))
            return(NULL);
    } while ((buttons != but) || (dx != height) || (dy != width));

/* cursor */

} else {
    drawcursor(oldx = mx,oldy = my,CURSOR_DRAW);
    do {

        /* get raw data - update */

        if (!rawxy(&buttons,&dx,&dy))
            return(NULL);
        oldx = mx;    oldy = my;
        mx += dx;    my += dy;
        if (mx < 0) mx = 0;
        if (my < 0) my = 0;
        if (mx >= xmax) mx = xmax - 1;
        if (my >= ymax) my = ymax - 1;

        /* redraw cursor */

        if ((oldx != mx) || (oldy != my)) {
            drawcursor(oldx,oldy,CURSOR_ERASE);
            drawcursor(mx,my,CURSOR_DRAW);
        };

        /* return condition */

    } while (((func == CURSOR_PRESS) && (!buttons)) ||
        ((func == CURSOR_RELEASE) && (buttons)));
    drawcursor(mx,my,CURSOR_ERASE);
};

/* return values */

*xx = mx;
*yy = my;
return(buttons);
}

```

```

/* func: drawcursor(mx,my,func)
   desc: draw or erase cursor
   args: (short) mx,
          my;
          (short) func; 0=DRAW, 1=ERASE
   ret:  <void>
*/

void
drawcursor(mx,my,func)
short mx,
       my,
       func;
{
    short i,
          height;
    pointer addr = fb + ADDR(mx,my);
    byte *cptr,
          bit;

    static byte bit_data[MAX_CURSOR_Y * MAX_CURSOR_X],
                 cursor_data[] = { 0x01,0x03,0x07,0x0f,0x1f,0x3f,0x7f,
                                    0xff,0x1f,0x1b,0x19,0x31,0x30,0x20 };

    cptr = cursor_data;  i = 0;
    for (height = MAX_CURSOR_Y; height--; cptr++) {
        for (bit = 1; bit; bit <= 1) {
            if (*cptr & bit) {
                if (func == CURSOR_DRAW) {
                    bit_data[i++] = *addr;
                    *(addr++) = 0x50 | color_cursor;
                } else
                    *(addr++) = bit_data[i++];
            } else
                addr++;
        };
        addr += DELY - MAX_CURSOR_X;
    };
}

```

```

/* file: gfx.c
desc: graphical utilities
func: drawline(x0,x1,y0,y1,color)
      drawframe(x0,x1,y0,y1,color)
      drawbox(x0,x1,y0,y1,color)
      clear()
date: 03/09/87 rjk
mod: 12/10/87 msc

*/

#include "ips.h"

/* func: drawline(x0,y0,x1,y1,color)
desc: draw a line on an image/frame
args: (short) x0,y0;      * starting point *
      (short) x1,y1;      * ending point *
      (byte) color;       * value to use, or -1 for exclusive-oring *
ret: <void>
*/

void
drawline(x0,y0,x1,y1,color)
short    x0,
         y0,
         x1,
         y1;
byte color;
{
    short l,
          expr,
          e1,
          e2,
          inc,
          ddx,
          ddy,
          len;
    pointer addr;

    /* vertical line */

    if (x0 == x1) {
        if ((x0 < 0) || (x0 >= xmax))
            return;
        if (y1 < y0) {
            l = y0;
            y0 = y1;
            y1 = l;
        };
        if ((y0 >= ymax) || (y1 < 0))
            return;
        if (y0 < 0) y0 = 0;
        if (y1 >= ymax) y1 = ymax - 1;
        addr = fb + ADDR(x0,y0);
        for (l = y1 - y0; l-- >= 0; addr += DELY)
            if (color == 0xff)
                *addr ^= 0xff;
    }
}

```



```

    else
        *addr = (*addr & color_mask) | color;

/*    horizontal line    */

} else if (y0 == y1) {
    if ((y0 < 0) || (y0 >= ymax))
        return;
    if (x1 < x0) {
        l = x0;
        x0 = x1;
        x1 = l;
    };
    if ((x0 >= xmax) || (x1 < 0))
        return;
    if (x0 < 0) x0 = 0;
    if (x1 >= xmax) x1 = xmax - 1;
    addr = fb + ADDR(x0,y0);
    for (l = x1 - x0; l--; addr++)
        if (color == 0xff)
            *addr ^= 0xff;
        else
            *addr = (*addr & color_mask) | color;

/*    bresenham line algorithm    */

} else {
    if ((x0 < 0) || (x0 >= xmax) || (x1 < 0) || (x1 >= xmax) ||
        (y0 < 0) || (y0 >= ymax) || (y1 < 0) || (y1 >= ymax))
        return;
    ddx = ABS(x1 - x0);
    ddy = ABS(y1 - y0);
    if (ddy <= ddx) {
        if (x1 < x0) {
            l = x0;
            x0 = x1;
            x1 = l;
            l = y0;
            y0 = y1;
            y1 = l;
        };
        inc = (y1 > y0) ? DELY : -DELY;
        e1 = (expr = (e2 = (ddy << 1) - ddx) - ddx);
        len = ddx + 1;
        addr = fb + ADDR(x0,y0);
        while (len--) {
            if (color == 0xff)
                *addr ^= 0xff;
            else
                *addr = (*addr & color_mask) | color;
            if (expr > 0) {
                addr += inc + 1;
                expr += e1;
            } else {
                addr++;
                expr += e2;
            };
        };
    }
    else {
        if (y1 < y0) {
            l = y0;

```

```

    y0 = y1;
    y1 = 1;
    l = x0;
    x0 = x1;
    x1 = 1;
};
    inc = (x0 > x1) ? -1 : 1;
    len = ddy + 1;
    e1 = (expr = (e2 = (ddx << 1) - ddy) - ddy);
    addr = fb + ADDR(x0,y0);
    while (len--) {
        if (color == 0xff)
            *addr ^= 0xff;
        else
            *addr = (*addr & color_mask) | color;
        if (expr > 0) {
            addr += DELY + inc;
            expr += e1;
        } else {
            addr += DELY;
            expr += e2;
        }
    };
};
};
}

/* func: drawframe(x0,y0,x1,y1,color)
   desc: draw a frame on an image/frame
   args: (int) x0,y0;          * one corner *
         (int) x1,y1;          * another corner *
         (byte) color;         * value to use, or -1 for exclusive-or *
   ret:  <void>
*/

void
drawframe(x0,y0,x1,y1,color)
int      x0,
         y0,
         x1,
         y1;
byte color;

{
    drawline(x0,y0,x1,y0,color);
    drawline(x1,y0,x1,y1,color);
    drawline(x1,y1,x0,y1,color);
    drawline(x0,y1,x0,y0,color);
}

/* func: drawbox(x0,y0,x1,y1,color)
   desc: draw a box on an image/frame
   args: (int) x0,y0;          * one corner *
         (int) x1,y1;          * another corner *
         (byte) color;         * value to use, or -1 for exclusive-or *
   ret:  <void>
*/

```

```

void
drawbox(x0,y0,x1,y1,color)
int      x0,
         y0,
         x1,
         y1;
byte color;

{
    short l,
          len;
    pointer addr;

    /* left to right */

    if (x1 < x0) {
        l = x0;
        x0 = x1;
        x1 = l;
    };
    if (y1 < y0) {
        l = y0;
        y0 = y1;
        y1 = l;
    };

    /* loop by rows */

    x1 -= (x0 - 1);
    for (addr = fb + ADDR(x0,y0); y0++ <= y1; addr += DELY - x1) {
        len = x1;
        if (color == 0xff)
            while (len--)
                *(addr++) ^= 0xff;
        else
            while (len--) {
                *addr = (*addr & color_mask) | color;
                addr++;
            };
    };
}

/* func: clear(v)
   desc: clears frame buffer, redisplay menu
   args: pointer v;      * frame to grab *
   ret: <void>
*/

void
clear(v)
pointer v;
{
    short i,
          len,
          start;

```

```

/* clear lower three bits of v0 */

*alu = 0x00;
*(v + mask) = 0xf8;
*(v + ctrh) = 0x08;
len = (*(v + ctrl) == 0x40) ? 11 : 7;
start = *(v + pan) + 512 * *(v + pan + 1);
*(v + pan) = (512 + start - len) & 0xff;
*(v + pan + 1) = (512 + start - len) >> 8;
for (i = 0; i < 2; i++) {
    while (!(*(v + ctrh) & 0x40));
    while (*(v + ctrh) & 0x40);
};
*(v + mask) = 0x07;
*(v + pan) = start & 0xff;
*(v + pan + 1) = start >> 8;

```

```

/* file: ips.c
   desc: image processing system drivers
   func: ips_init()
         ips_close()
   date: 07/02/87 msc
   mod: 12/10/87 msc
*/

#include "ips.h"

/* func: ips_init()
   desc: initialize ips hardware parameters
   args: <none>
   ret:  bool:  FALSE = error
         TRUE  = successfull
*/

bool
ips_init()
{
    register short i,
                  j;
    short k;
    pointer v[3];
    static byte slutidx[] = { 0x00,0x55,0xaa,0xff };

    /* initialize bus */

    if (!bus_init())
        return(FALSE);

    /* initialize registers */

    if (!reg_init())
        return(FALSE);

    /* default values */

    xmax = MAX_X_OFFSET;  ymax = MAX_Y_OFFSET; /* screen size */
    color_mask = 0x00;    color_cursor = 0xff; /* color scheme */
    fb = d0;              /* frame address */
    camera = 0x00;        /* camera input */

    /* initialize 'apcval' and 'slutval' arrays */

    for (i = 0; i < 4; i++) {
        apcval[i] = 0x40 * i;
        slutval[i] = slutidx[i];
    };

    /* initial values of registers */

    /* input lookup table */
    /* input LUT 0: zero */
    /* input LUT 1,2: linear */
    /* input LUT 3: inverse linear */

```

```

for (i = 0; i < 4; i++) {
    *apc = 0x00;
    *slut = slutval[i];
    for (j = 0; j < 256; j++) {
        *alut = (byte) j;
        *dlut = (i == 0) ? 0 : ((i != 3) ? j : 255 - j);
    };
};

/*  output lookup tables          */
/*  output LUT 0:      zero      */
/*  output LUT 1,2,3:  linear    */

for (i = 1; i < 4; i++) {
    *apc = apcval[i];
    for (j = 0; j < 256; j++) {
        *alut = (byte) j;
        for (k = 0; k < 3; k++) {
            *slut = (byte) slutval[k];
            *dlut = (k == 0) ? 0 : j;
        };
    };
};

/*  alu & mux registers          */

*apc = 0x00;
*slut = 0x55;
*k1 = *k2 = *k3 = 0;
*alu = *shft = *mult = 0;
*offs = 0x00;
*gain = 0x80;
*ab = 0x44;
*cd = 0x44;
*e = 0x00;
*out = 0;

/*  reset x,y,pan,control,mask registers  */

v[0] = v0;
v[1] = v1;
v[2] = v2;
for (i = 0; i < 3; i++) {

    /*  set for full screen (512x480)  */

    *(v[i] + ctrl) = 0x40;
    *(v[i] + mask) = 0x00;

    /*  initialize frame registers  */

    for (j = 0; j < 2; j++) {
        *(v[i] + x + j) = 0x00;
        *(v[i] + y + j) = 0x00;
        *(v[i] + pan + j) = 0x00;
        *(v[i] + scroll + j) = 0x00;
    };
};

```

```

};

/* wait one frame time */
while(!*(v0 + ctrh) & 0x40);
while(*(v0 + ctrh) & 0x40);

/* clear screen */
*(v[i] + ctrh) = 0x08;
};

/* wait two frame times */
for (i = 0; i < 2; i++) {
    while(!*(v0 + ctrh) & 0x40);
    while(*(v0 + ctrh) & 0x40);
};

return(TRUE);
}

/* func: ips_close()
   desc: close ip system
   args: <none>
   ret:  <void>
*/

void
ips_close()
{
    reg_close();
    bus_close();
}

```

```

/* file: ips.h
   desc: macros for standard ips routines
   date: 07/01/87 msc
   mod:  11/10/87 msc
*/

/* type definitions */

typedef unsigned char  byte;
typedef char           bool;
#ifdef M_XENIX
typedef byte huge *    pointer;
#else
typedef byte *         pointer;
#endif

/* macro boolean macros */

#undef NULL
#define NULL 0
#define FALSE 0
#define TRUE 1
#define ERR -1

/* macro register constants */

#define REG 1 /* register (k1,k2,ab,etc..) */
#define FRAME 2 /* frame (v0,v1,v2) */
#define OFFSET 3 /* offset (x,y,pan,scroll,etc..) */

/* macro constant maximums */

#define MAX_X_OFFSET 512 /* max x pixel offset */
#define MAX_Y_OFFSET 480 /* max y pixel offset */
#define MAX_LABEL 16 /* maximum length of register name */
#define MAX_REGS 32 /* maximum number of system registers */
#define MAX_QUEUE 512 /* max queue size */

/* macro keyboard constants */

#define BACK ' ' /* backspace */
#define BRK 0x7f /* break key */
#define DEL " " /* delete key */
#define ESC 0x1b /* escape key */
#define RET '\n' /* return key */

/* macro cursor constants */

#define CURSOR_FLUSH 0 /* flush cursor input */
#define CURSOR_GET 1 /* return cursor parameters stat */
#define CURSOR_PRESS 2 /* wait until button is pressed */
#define CURSOR_RELEASE 3 /* wait until button is released */

/* macro image constants */

#define DELY 512 /* default value for image.dely */

```



```
/* macro functions */
```

```
#define MIN(x,y) ((x <= y) ? x : y)
#define MAX(x,y) ((x >= y) ? x : y)
#define ABS(x) (((x) >= 0) ? (x) : -(x))
#define ABS2(x,y) (((x) >= y) ? (x - (y)) : (y - (x)))
#define SIGN(x) ((x < 0) ? -1 : 1)
#define ADDR(x,y) ((DELY * (long) (y)) + (x))
```

```
/* image processing data structures */
```

```
struct regtype {
    char label[MAX_LABEL]; /* label of register */
    pointer addr; /* register address */
    short type, /* register type (REG,FRAME,OFFSET) */
        offset, /* register offset */
        len; /* register length (1 or 2) */
};
```

```
#ifndef M_XENIX
```

```
struct qtype {
    short dx,dy, /* mouse delta x & y values */
        buttons; /* mouse buttons */
};
#endif
```

```
/* global variables */
```

```
pointer ips_base; /* base address for image proc. system */
int ipd; /* image proc. system file descriptor */
#ifdef M_XENIX
int mfd; /* mouse file descriptor */
#else
int tfd; /* terminal file descriptor */
struct qtype mqueue[MAX_QUEUE], /* queue for mouse cursor stats */
    *mqbegin,
    *mqend;
#endif
char cqueue[MAX_QUEUE], /* queue for character input */
    *cqbegin,
    *cqend;
pointer d0,d1,d2, /* frame buffer data addresses */
    v0,v1,v2, /* frame buffer control addresses */
    pyrmem,sst, /* pyramid program,status register */
    dlut,alut,slut,apc, /* lookup tables */
    k1,k2,k3,ab,cd,e, /* multipliers, channels */
    alu,shft,out,mult, /* alu parms */
    offs,gain; /* camera offset & gain controls */
short x,y,pan,scroll, /* frame buffer x & y parms */
    ctrl,ctrh,mask; /* frame buffer control parms */
pointer fb; /* current frame buffer */
byte color_mask, /* number of bits for color ~ 0xff */
    color_cursor; /* color of screen cursor */
short xmax,ymax; /* maximum screen size for gfx,cursor */
short char_width,char_height; /* size of character font */
byte apcval[4], /* index for apc: 0x00,0x40,0x80,0xc0 */
    slutval[4], /* index for slut: 0x00,0x55,0xaa,0xff */
    camera; /* camera 0x00 or 0x20 - 'ored to apc */
short num_reg; /* number of registers */
```

```

struct regtype regs[MAX_REGS]; /* data structure for register info */

/* system functions */

char *strcpy(),*strncpy(), /* string library functions */
    *strcat(),*strncat(), /* string library functions */
    *getenv(); /* return home environment */
long lseek(); /* i/o functions */
int atoi(); /* string to int conversion function */
long atol(); /* string to long conversion function */
double atof(); /* string to float conversion function */
char *malloc(); /* dynamic memory allocation routine */
void free(); /* return allocated memory to system */

/* external functions */

/* bus.c */
bool bus_init();
void bus_close();

/* cursor.c */
bool cursor_init();
void cursor_close();
bool rawxy();
bool isbut();
short getxy();
void drawcursor();

/* gfx.c */
void drawline();
void drawframe();
void drawbox();
void clear();

/* ips.c */
bool ips_init();
void ips_close();

/* keyboard.c */
bool key_init();
void key_close();
char getch();
bool iskey();

/* main.c */
int main();

/* reg.c */
bool reg_init();
void reg_close();

/* screen.c */
bool screen_init();
void screen_close();
void drawstr();
void drawch();
void err();

/* wr.c */
bool wrrips();

```

```

/* file: key.c
   desc: keyboard i/o
   func: key_init()
         key_close()
         getch()
         iskey()
   date: 07/14/87 msc
   mod: 11/11/87 msc
*/

/* include files */

#include <fcntl.h>
#ifdef M_XENIX
#include <stdio.h>
#include <sys/hft.h>
#endif
#include "ips.h"

/* func: key_init()
   desc: initialize keyboard
   args: <none>
   ret:  bool:  FALSE == unsuccessfull
          TRUE  == successfull
*/

bool
key_init()
{
    /* initialize */

#ifdef M_XENIX
    system("stty -echo -brkint -isig -istrip -icanon eof ");
#else
    char kstr[80];

    sprintf(kstr, "/dev/hft/%d", ioctl(0, HFGCHAN, 0));
    if ((tfd = open(kstr, O_RDWR | O_NDELAY)) == ERR)
        if ((tfd = open("/dev/tty", O_RDWR | O_NDELAY)) == ERR) {
            fprintf(stderr, "cannot open vterm\n");
            exit(1);
        };

    system("stty -enhedit ignpar -echo -brkint -isig -istrip -icanon eof ");
    mqbegin = mqend = mqueue;          /* reset cursor queue */
#endif
    cqbegin = cqend = cqueue;          /* reset character queue */

    return(TRUE);
}

/* func: key_close()
   desc: close keyboard
   args: <none>
   ret:  <void>
*/

```

```

void
key_close()
{

#ifdef M_XENIX
    close(tfd);
#endif
    system("stty sane echoe ixany tab3");
}

/* func:  getch()
   desc:  receive character through keyboard
   args:  <none>
   ret:   char:  character typed in, or NULL if none in keyboard buffer
*/

char
getch()
{
    char ch = NULL;

    if (iskey()) {
        ch = *cqbegin;
        if (++cqbegin >= cqueue + MAX_QUEUE)
            cqbegin = cqueue;
    };

    return(ch);
}

/* func:  iskey()
   desc:  checks keyboard for character typed
   args:  <none>
   ret:   bool:  FALSE == no character entered
              TRUE  == character pressed
*/

bool
iskey()
{
    char ch = NULL;

#ifdef M_XENIX
    while (rdchk(0) > 0) {
        read(0,&ch,1);
        *cqend = ch;
        if (++cqend >= cqueue + MAX_QUEUE)
            cqend = cqueue;
    };
#else
    short i;
    struct mice {
        short deltax,
            deltay;
        char sec[3];
        char sixtyths,

```

```

        buttons,
        stype;
    } mouse;

    while (read(tfd,&ch,1) == 1)
        if (ch == ESC) {
            if ((read(tfd,&ch,1) == 1) && (ch == '['))
                if ((read(tfd,&ch,1) == 1) && (ch == 'y')) {
                    for (i = 0; i < sizeof(struct mice); i++)
                        if (read(tfd,((char *) &mouse) + i,1) < 1)
                            break;
                    mqend->dx = mouse.deltax;
                    mqend->dy = mouse.deltay;
                    mqend->buttons = mouse.buttons;
                    if (++mqend >= mqueue + MAX_QUEUE)
                        mqend = mqueue;
                };
            ch = NULL;
        } else {
            *cqend = ch;
            if (++cqend == cqueue + MAX_QUEUE)
                cqend = cqueue;
        };
    #endif

    return(cqbegin != cqend);
}

```

```

/* file: reg.c
   desc: functions for register reading/writing
   func: reg_init()
         reg_close()
   date: 05/14/87 msc
   mod:  11/14/87 msc
*/

#include <stdio.h>
#include "ips.h"

/* static variables */

static struct fldsettype {
    char *label;
    pointer *addr;
    short *offset;
} fldset[] = {
    {"v0",&v0,NULL},{"d0",&d0,NULL},{"v1",&v1,NULL},{"d1",&d1,NULL},
    {"v2",&v2,NULL},{"d2",&d2,NULL},{"pyrmem",&pyrmem,NULL},{"sst",&sst,NULL},
    {"dlut",&dlut,NULL},{"alut",&alut,NULL},{"slut",&slut,NULL},{"apc",&apc,NULL},
    {"k1",&k1,NULL},{"k2",&k2,NULL},{"k3",&k3,NULL},{"ab",&ab,NULL},
    {"cd",&cd,NULL},{"e",&e,NULL},{"alu",&alu,NULL},{"shft",&shft,NULL},
    {"out",&out,NULL},{"mult",&mult,NULL},{"offs",&offs,NULL},{"gain",&gain,NULL},
    {"x",NULL,&x},{"y",NULL,&y},{"pan",NULL,&pan},{"scroll",NULL,&scroll},
    {"ctrl",NULL,&ctrl},{"ctrh",NULL,&ctrh},{"mask",NULL,&mask},
    {"",NULL,NULL}
};

/* func: reg_init()
   desc: initialize registers
   args: <none>
   ret:  (bool)    FALSE == error
           TRUE  == successfull
*/

bool
reg_init()
{
    char *hp,
        str[80],
        type[40],
        saddr[40],
        attr[80],
        env[40];
    short tp;
    long raddr,
        len;
    FILE *fd;
    struct fldsettype *fs;
    struct regtype *rp;

    /* clear variables */

    num_reg = 0;          /* number of registers */

```

```

/* get home directory */
if (!(hp = getenv("HOME"))) {
    fprintf(stderr,"could not get home directory\n");
    return(FALSE);
};

/* initialize registers */

/* get hardware stats from file '$HOME/.cliphw' */
sprintf(str,"%s/.cliphw",hp);
if (!(fd = fopen(str,"r")))
    fd = fopen("/usr/clip/home/cliphw","r");
if (fd) {
    while (!feof(fd))
        if (fgets(str,79,fd)) {
            if (!strncmp(str,"/*",2))
                continue;
            if (sscanf(str,"%s%s%s%s",type,env,saddr,attr) == 4) {
                if (!strncmp(saddr,"0x",2))
                    sscanf(saddr + 2,"%lx",&raddr);
                else
                    raddr = atol(saddr);
                if (!strncmp(attr,"0x",2))
                    sscanf(attr + 2,"%lx",&len);
                else
                    len = atol(attr);

                /* find specific variable */

                for (fs = fldset; (fs->addr) || (fs->offset); fs++)
                    if (!strcmp(fs->label,env))
                        break;
                if ((fs->addr) && !(fs->offset)) {
                    fprintf(stderr,"unable to assign register '%s'\n",env);
                    return(FALSE);
                };

                /* assign value */

                if (!strcmp(type,"frame")) {
                    tp = FRAME;
                    *((fs + 1)->addr) = ips_base + len;
                    *(fs->addr) = ips_base + raddr;
                } else if (!strcmp(type,"offset")) {
                    tp = OFFSET;
                    *(fs->offset) = raddr;
                } else if (!strcmp(type,"reg") || !strcmp(type,"addr")) {
                    tp = REG;
                    *(fs->addr) = ips_base + raddr;
                } else {
                    fprintf(stderr,"invalid type '%s' for label '%s'\n",type,env);
                    return(FALSE);
                };

                /* add to register table */

                rp = regs + num_reg++;
                strcpy(rp->label,env);
            }
        }
}

```

```

        rp->type = tp;
        rp->offset = raddr;
        rp->len = len;
    } else
        fprintf(stderr,"sscanf failed on: '%s'\n",str);
    };
} else {
    fprintf(stderr,"could not open $HOME/.cliphw file\n");
    return(FALSE);
};

return(TRUE);
}

/* func:  reg_close()
   desc:  close registers
   args:  <none>
   ret:   <void>
*/

void
reg_close()
{

```



```

/* file: screen.c
   desc: functions for screen display & io
   func: screen_init()
         screen_close()
         drawstr(sp,row,col,color)
         drawch(ch,row,col,color)
   date: 06/26/87 msc
   mod:  11/16/87 msc
*/

```

```

#include <stdio.h>
#include <fcntl.h>
#include "ips.h"

```

```

/* macro constants */

```

```

#define FONT_HDR_LEN 0x2c
#define DDDFSIZE 0x00
#define FNTCOLMN 0x1c
#define FNTROWS 0x1e
#define FNTLKU 0x28
#define FNTBUG 0x60

```

```

/* static variables */

```

```

static struct fonts { /* information concerning font */
    byte *hptr,
        *dptr,
        *tptr;
} font;

```

```

/* func: screen_init(fontname)
   desc: initialize screen and load font
   args: char *fontname;  * name of font to use *
   ret:  (bool) FALSE == error
         TRUE == successfull
*/

```

```

bool
screen_init(fontname)
char *fontname;
{

```

```

    int fd;
    char str[80];
    unsigned int len;

```

```

/* load font */

```

```

if ((fd = open(fontname,O_RDONLY)) == ERR) {
    sprintf(str,"/usr/clip/font/%s",fontname);
    fd = open(str,O_RDONLY);
};

```

```

if (fd == ERR) {
    fprintf(stderr,"cannot open font file\n");
    return(NULL);
};

```

```

if (lseek(fd,(long) FNTBUG,0) == ERR) {

```

```

    fprintf(stderr,"cannot lseek font file\n");
    close(fd);
    return(NULL);
};
if (font.hptr) {
    free(font.hptr);
    font.hptr = NULL;
    free(font.dptr);
    font.dptr = NULL;
};
font.hptr = (byte *) malloc(FONT_HDR_LEN);
if (read(fd,font.hptr,(int) FONT_HDR_LEN) < FONT_HDR_LEN) {
    fprintf(stderr,"cannot read font header\n");
    free(font.hptr);
    font.hptr = NULL;
    close(fd);
    return(NULL);
};
/* len note - assumes <64K files */
len = 256 * *(font.hptr + DDDFSIZE + 2) + *(font.hptr + DDDFSIZE + 3);
char_width = 256 * *(font.hptr + FNTCOLMN) + *(font.hptr + FNTCOLMN + 1);
char_height = 256 * *(font.hptr + FNTROWS) + *(font.hptr + FNTROWS + 1);
font.dptr = (byte *) malloc(len);
if (read(fd,font.dptr,len) == ERR) {
    fprintf(stderr,"cannot read font data\n");
    free(font.hptr);
    font.hptr = NULL;
    close(fd);
    return(NULL);
};
if (close(fd) == ERR) {
    fprintf(stderr,"cannot close font file\n");
    return(NULL);
};
/* lku note - assumes <64K files */
len = 256 * *(font.hptr + FNTLKU + 2) + *(font.hptr + FNTLKU + 3);
font.tptr = font.dptr + len - FONT_HDR_LEN;

return(TRUE);
}

/* func: screen_close()
   desc: close screen, free memory
   args: <none>
   ret:  <void>
*/

void
screen_close()
{
    free(font.hptr);
    free(font.dptr);
}

/* func: drawstr(sp,row,col,color)
   desc: draws string on screen
   args: (char *) sp;      * string to display *

```

```

        (int) x,y;          * location *
        (byte) color;       * color *
ret: <void>
*/

void
drawstr(sp,x0,y0,color)
char *sp;
int x0,
    y0;
byte color;
{
    for (; *sp; x0 += char_width)
        drawch(*(sp++),x0,y0,color);
}

/* func: drawch(sp,row,col,color)
   desc: draws character on screen
   args: (char) ch;          * string to display *
          (int) x,y;         * location *
          (byte) color;      * color *
   ret: <void>
*/

void
drawch(ch,x0,y0,color)
char ch;
int x0,
    y0;
byte color;
{
    pointer addr;
    short i,
        y1,
        width,
        height;
    byte *tptr,
        *cptr,
        bit;

    /* calculate table location, width, height */

    tptr = font.tptr + 4 * ch;
    width = *(tptr + 1) & 0x3f;
    height = char_height - (*tptr >> 3) -
        ((*tptr & 0x07) << 2) - (*(tptr + 1) >> 6);
    cptr = font.dptr + 256 * *(tptr + 2) + *(tptr + 3);

    /* center character */

    x0 += (char_width - width) / 2;
    y1 = y0 + (*tptr >> 3);

    /* loop */

    addr = fb + ADDR(x0,y1);
    for (bit = 128; height--; addr += DELY - width)
        for (i = 0; i < width; i++, addr++) {
            if (*cptr & bit) {

```

```
    if (color == 0xff)
        *addr ^= 0xff;
    else
        *addr = (*addr & color_mask) | color;
};
if ((bit >>= 1) == 0) {
    cptr++;
    bit = 128;
};
};
```

```

/* file: state.c
   desc: functions for ips program manipulation
   func: skipch(sp)
         st_encode(st,sp)
         ips_pgm(st)      * AIX only *
   date: 05/08/87 msc
   mod:  11/17/87 msc
*/

#include <stdio.h>
#include <ctype.h>
#include "ips.h"

/* global variables */

static char *valid[] = { "+-*/%&|^<>@#~!=",
                        "===== ",
                        "+-*/%&|^<>@#~!:" };

/* func: skipch(sp)
   desc: skip over space, tabs, and carriage returns
   args: (char *) sp;      * string *
   ret:  (char *): pointer to NULL or non-white space character
*/

char *
skipch(sp)
char *sp;
{
    while (*sp && ((*sp == ' ') || (*sp == '\t') || (*sp == '\n')))
        sp++;
    return(sp);
}

/* func: st_encode(st, strptr)
   desc: encode state information from string
   args: (byte *) st;      * state to encode to *
         (str *) str;      * string with info *
   ret:  variable: FALSE == error
           TRUE == successfull
*/

bool
st_encode(bp, sp)
byte *bp;
char *sp;
{
    short offset,
          len,
          i,
          j,
          val;
    char label[40],
          op1,
          op2,

```

```

        *lp;
byte rg;

/*  decode  */

while (*sp) {

    /*  clear  */

    *bp = 0xff;

    /*  optional semicolon  */

    if (*sp && (*sp == ';'))
        sp = skipch(sp + 1);

    /*  register  */

    sp = skipch(sp);
    for (lp = label; *sp && (isalnum(*sp)); *(lp++) = *(sp++));
    *lp = NULL;
    sp = skipch(sp);
    for (i = 0; i < num_reg; i++)
        if (!strcmp(label, regs[i].label))
            break;
    if (i == num_reg) {
        fprintf(stderr, "register '%s' not defined\n", label);
        return(FALSE);
    };
    offset = regs[i].offset;
    len = regs[i].len;
    if (regs[i].type == FRAME) {
        if (*sp == '.') {
            sp = skipch(sp + 1);
            for (lp = label; *sp && (isalnum(*sp)); *(lp++) = *(sp++));
            *lp = NULL;
            sp = skipch(sp);
            for (j = 0; j < num_reg; j++)
                if (!strcmp(label, regs[j].label))
                    break;
            if ((j == num_reg) || (regs[j].type != OFFSET)) {
                fprintf(stderr, "'%s' is not an offset variable\n", label);
                return(FALSE);
            };
            offset += regs[j].offset;
            len = regs[j].len;
        } else {
            fprintf(stderr, "'.' required after frame variable\n");
            return(FALSE);
        };
    } else if (regs[i].type != REG) {
        fprintf(stderr, "'%s' is not a register\n", label);
        return(FALSE);
    };
    rg = ((offset & 0x1fff) == 0x100) ? 0x80 : offset & 0xff;
    *(bp + 1) = len;

    /*  operation  */

```

```

    op1 = *(sp++);
    op2 = (*sp == '=' ? *(sp++) : ' ');
    for (i = 0; valid[0][i]; i++)
        if ((op1 == valid[0][i]) && (op2 == valid[1][i]))
            break;
    if (!valid[0][i]) {
        fprintf(stderr, "illegal operation '%c'\n", *sp);
        return(FALSE);
    };

    *(bp + 2) = valid[2][i];
    sp = skipch(sp);

    /* value */

    for (lp = label; *sp && (isalnum(*sp)); *(lp++) = *(sp++));
    *lp = NULL;
    sp = skipch(sp);
    /* value or mask */
    if (!strcmp(label, "0x", 2))
        sscanf(label + 2, "%hx", &val);
    else if (isdigit(*label))
        val = atoi(label);
    else if (*(bp + 2) == '=') {
        /* register (from copy register) */
        *(bp + 2) = ' ';
        val = -1;
        for (i = 0; i < num_reg; i++)
            if (!strcmp(label, regs[i].label)) {
                val = regs[i].offset;
                if (regs[i].type == FRAME) {
                    if (*sp == '.') {
                        sp = skipch(sp + 1);
                        for (lp = label; *sp && (isalnum(*sp)); *(lp++) = *(sp++));
                        *lp = NULL;
                        sp = skipch(sp);
                        for (j = 0; j < num_reg; j++)
                            if (!strcmp(label, regs[j].label)) {
                                val += regs[j].offset;
                                break;
                            };
                        if (j == num_reg)
                            val = -1;
                    } else {
                        fprintf(stderr, "`.` required after frame variable\n");
                        return(FALSE);
                    };
                };
            };
        if (regs[i].type != REG)
            val = -1;
        else
            val = ((val & 0x1fff) == 0x100) ? 0x80 : val & 0xff;
    };
    if (val == -1) {
        fprintf(stderr, "illegal entry '%s'\n", label);
        return(FALSE);
    };
    *(bp + 3) = val & 0xff;

```

```

    *(bp + 4) = val >> 8;

    /* next */

    *bp = rg;
    bp += 5;
    *bp = 0xff;
};
return(TRUE);
}

#ifdef M_XENIX
/* func: ips_pgm(table)
   desc: program image processing system hardware registers
   args: byte *table;      * state variable buffer address *
   ret:  <void>
   */

void
ips_pgm(table)
byte *table;
{
    short num;
    register pointer addr;

    while (*table != 0xff) {
        addr = ips_base + ((*table == 0x80) ? 0x100 : *table);
        switch (*(table + 2)) {
            case '=': /* set value */
                *addr = *(table + 3);
                if (*(table + 1) == 2)
                    *(addr + 1) = *(table + 4);
                break;
            case '~': /* wait while equal to constant */
                num = *(table + 3);
                while (*addr == num);
                break;
            case '!': /* wait while NOT equal to constant */
                num = *(table + 3);
                while (*addr != num);
        };
        table += 5;
    };
}
#endif

```



```

/* file: wr.c
  desc:  write code from 'file.q' to control board
  func:  wrips(wname)
  date:  05/08/87 msc
  mod:   11/01/87 msc
*/

#include <stdio.h>
#include <fcntl.h>
#include <ctype.h>
#include "ips.h"

/*  macro constants  */

#define MAX_STRING      80          /*  maximum string length      */
#define MAX_PYR_MEMORY  4096       /*  maximum size of ips program ram */
#define MAX_RETRIES     25         /*  maximum number of write retries */

/*  local variables  */

byte buffer[2 * MAX_PYR_MEMORY];

/*  func:  wrips(wname)
  desc:  download file.q to pyramid board code space
        - this program adds code=0 to the end of the file
  args:  (char *) wname:          * file.q name, eg. "lp3.q" *
  ret:   (bool)   FALSE == error
          TRUE    == successfull
*/

bool
wrips(wname)
char *wname;
{
    short l,
           n = 0,
           pos = 0;
    byte *bp;
    char  b0,
           b1,
           str[MAX_STRING];
    register byte *np;
    int fd;

    /*  open file  */

    if ((fd = open(wname,O_RDONLY)) == -1) {
        sprintf(str,"usr/clip/q/%s",wname);
        if ((fd = open(str,O_RDONLY)) == -1) {
            fprintf(stderr,"unable to open %s\n",wname);
            return(FALSE);
        }
    };

    /*  read file  */

```

```

if ((l = read(fd,buffer,2 * MAX_PYR_MEMORY)) <= 0) {
    fprintf(stderr,"error %d while reading %s\n",l,wname);
    return(FALSE);
};

/*    convert    */

for (bp = np = buffer; bp - buffer < l; *(np++) = 16 * (short) b0 + b1) {
    b0 = *(bp++);    b1 = *(bp++);
    if (!isxdigit(b0) || !isxdigit(b1)) {
        fprintf(stderr,"invalid char at location %d in file %s\n",l,wname);
        return(FALSE);
    };
    b0 = (b0 > '9') ? toupper(b0) - 'A' + 10 : b0 - '0';
    b1 = (b1 > '9') ? toupper(b1) - 'A' + 10 : b1 - '0';
};

/*    file with zeroes    */

for (l /= 2; np < buffer + MAX_PYR_MEMORY; *(np++) = 0);
do {

    /*    check for too many times    */

    if (n++ >= MAX_RETRIES) {
        fprintf(stderr,"could not write to ips program memory\n");
        return(NULL);
    };

    /*    make sure the pointer starts on a WORD boundary    */

    pos &= 0xffff;

    /*    write to pyramid memory    */

#ifdef M_XENIX
    lseek(ipd,(long) (pyrmem - ips_base) + pos,0);
    write(ipd,bp = buffer + pos,MAX_PYR_MEMORY - pos);
#else
    memcpy(pyrmem + pos,bp = buffer + pos,MAX_PYR_MEMORY - pos);
#endif

    /*    read from pyramid memory    */

#ifdef M_XENIX
    lseek(ipd,(long) (pyrmem - ips_base) + pos,0);
    read(ipd,np = buffer + MAX_PYR_MEMORY,l - pos);
#else
    memcpy(np = buffer + MAX_PYR_MEMORY,pyrmem + pos,l - pos);
#endif

    /*    compare    */

    for (; pos < l; pos++)
        if (*(bp++) != *(np++))
            break;
} while (pos < l);

/*    close file    */

```

```
if (close(fd) == ERR) {  
    fprintf(stderr,"could not close file '%s'",wname);  
    return(FALSE);  
};  
  
/*  else, OK!  */  
  
return(TRUE);
```

APPENDIX B - ILLUSTRATIONS

<u>TITLE</u>	<u>PAGE</u>
System Block Diagram	83
Microprocessor to High Voltage Power Supply Interface Via D/A Converters and Inverting Op.Amps	84
A Schematic Drawing of Electrodes	85
Circuit Diagram of the High Voltage Unit	86

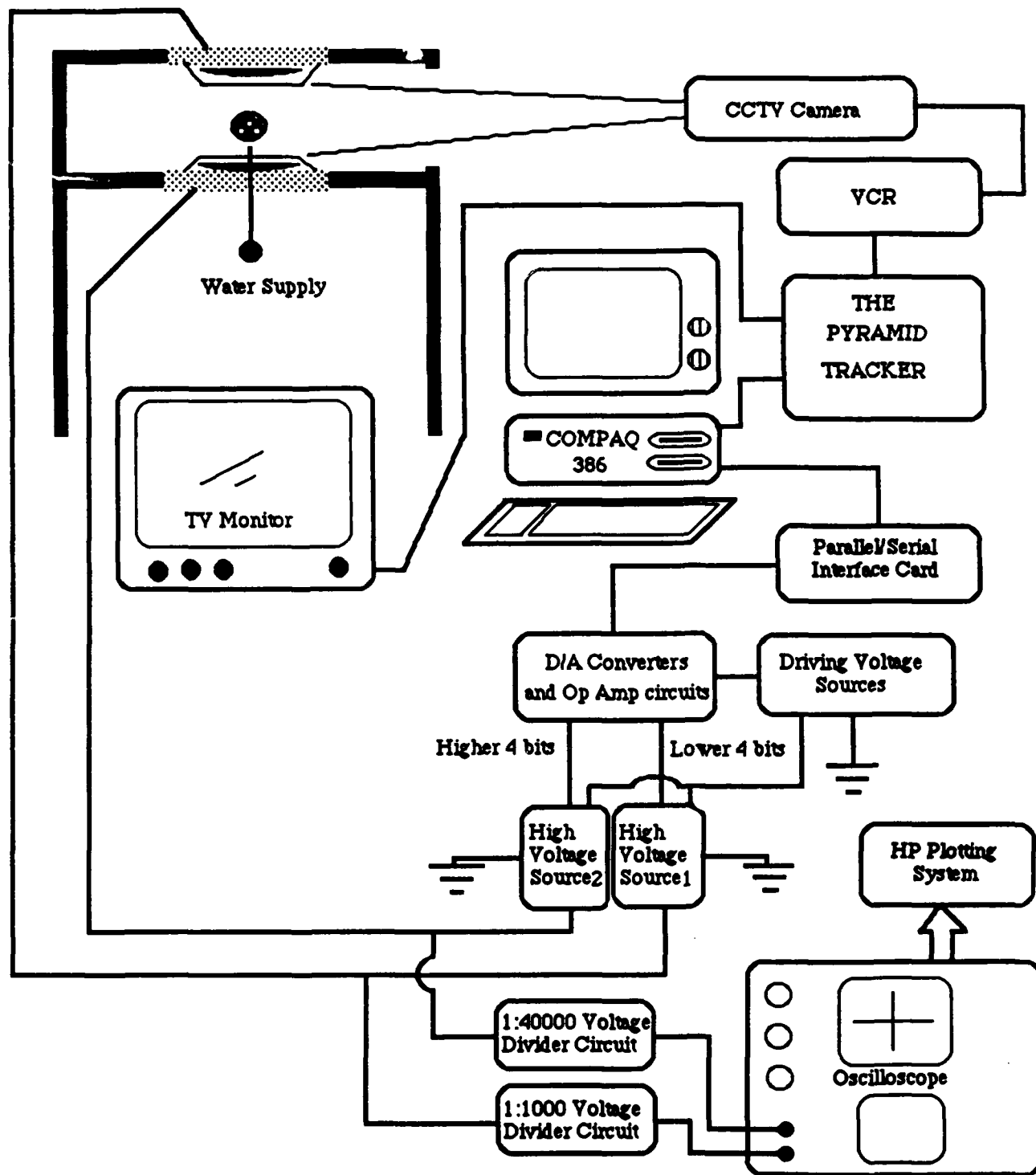


Figure 1: System Block Diagram

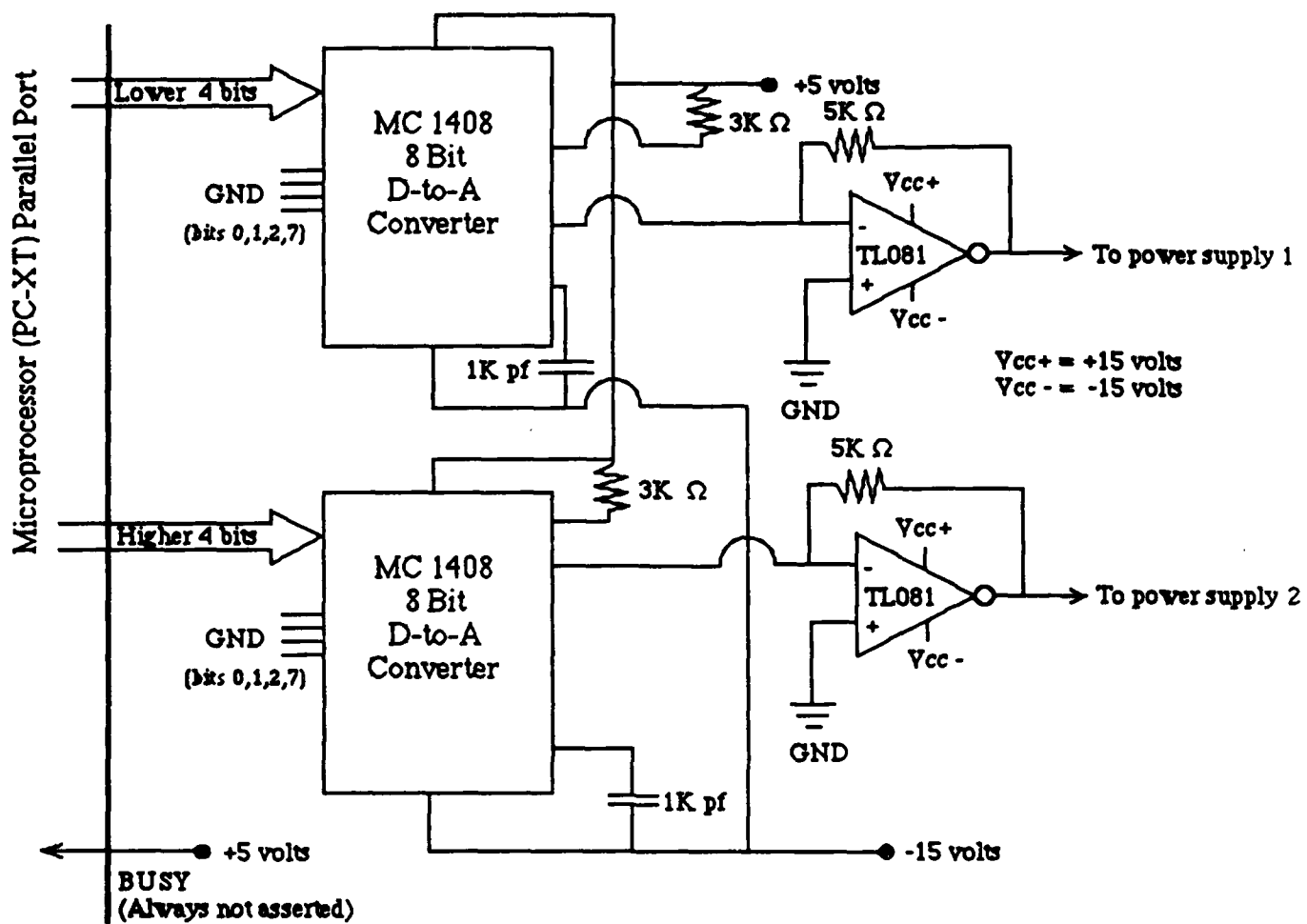


Figure 2: Microprocessor to High Voltage Power Supply Interface via D/A Converters and Inverting Op. Amps.

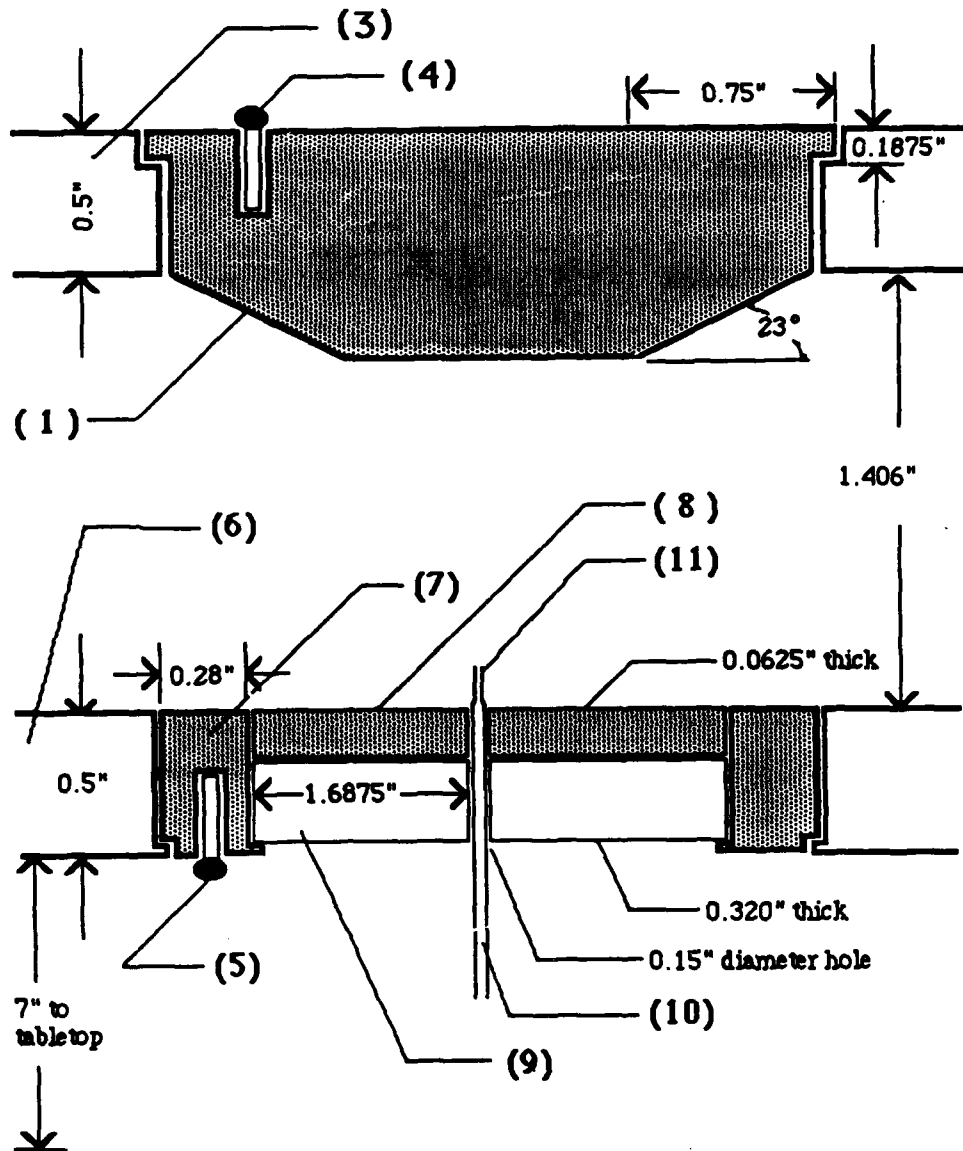


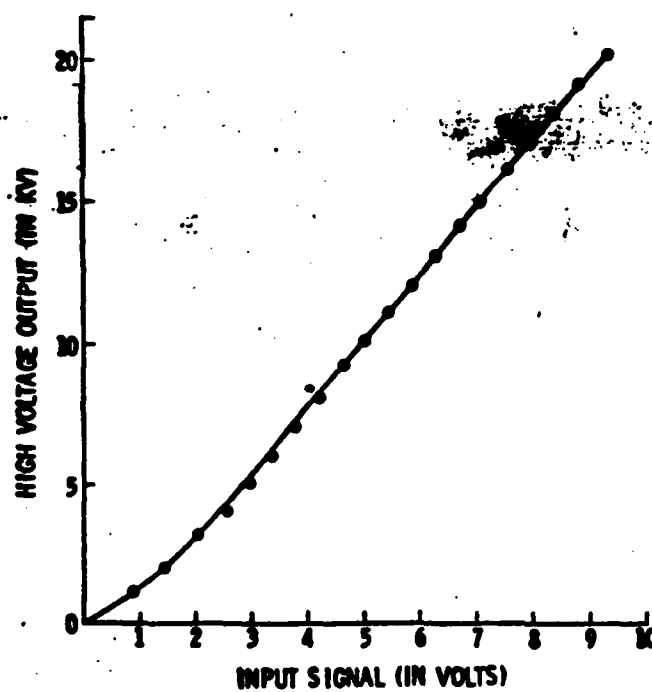
Figure 3: A Schematic Drawing of Electrodes

NOTE:

(1) is the tapered aluminum ring, (3) and (6) are plexiglas top and bottom walls of the chamber, (4) and (5) are connections to the aluminum rings, (7) is an aluminum ring, (8) is the aluminum disk, (9) is a plexiglas support, (10) is the tubing which leads to water supply, and (11) is the injection nozzle made by stretching out the glass tube.

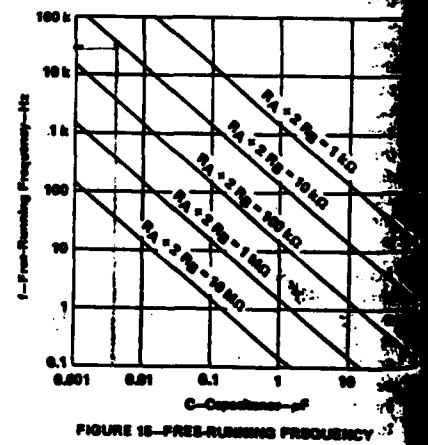
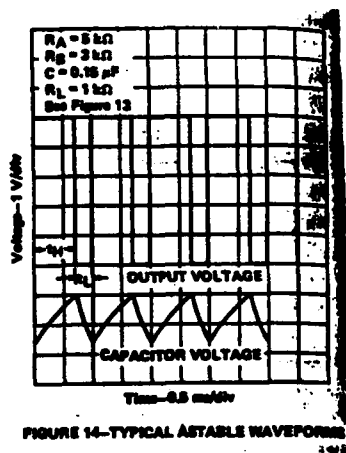
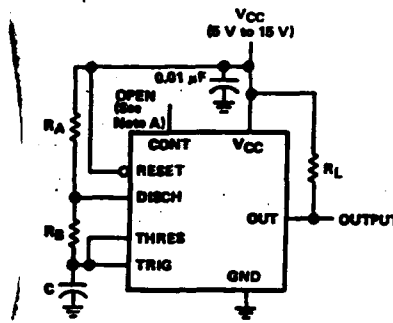
APPENDIX C - PLOTS

<u>TITLE</u>	<u>PAGE</u>
The Linearity Curve of the High Voltage Unit	88
Selecting the Frequency of the Square Wave Generated by NE 555	89



PLOT 1 : The Linearity Curve of the High Voltage Unit.

(taken from reference 11)



PLOT 2 : Selecting the Frequency of the Square Wave Generated by NE 555 (taken from reference 7)

APPENDIX B

Fundamental Studies of Electrostatic Atomization

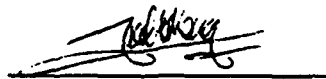
by

Kok-Meng Lue

Princeton University
School of Engineering and Applied Science
Department of Mechanical and Aerospace Engineering

Submitted in partial fulfillment of the requirements for the degree
of Master of Science in Engineering from Princeton University, 1988

Prepared by:



Approved by:


Prof. Robert G. Jahn
Thesis Advisor


Prof. Harvey S-H Lam
Thesis Reader

This thesis carries No. 1839T in the records of the Department of
Mechanical and Aerospace Engineering

Table of Contents

Abstract		1
Chapter I	Electrostatic Atomization	2
1.1	Introduction	2
1.2	Electrostatic Atomization Phenomena	2
1.3	Models and Experimental Data	4
1.4	Summary of Results	6
Chapter II	The Maximum Entropy Model	7
2.1	Maximum Entropy Model	7
2.2	Preliminary Results of Maximum Entropy Model	10
2.3	Further Verification of the Maximum Entropy Model	12
Chapter III	The Electrostatic Atomization Experiment	13
3.1	Charged Droplet Production/Vacuum Facility	13
3.2	Quadrupole Mass Spectrometer	14
3.3	Charge Detection Assembly	15
3.4	Experimental Procedure	16
Chapter IV	Data Analysis and Discussion	17
4.1	Introduction	17
4.2	Experimental Data	17
4.3	Comparison with Published Work	18
4.4	Size Distribution	19
4.5	Regression Analysis Results	20
4.6	Multiple Charging Characteristics	21
4.7	Regression Coefficients	23
4.8	Correction Term for Finite Electrical Conductivity	25
Chapter V	Summary	29

Bibliography	30
Appendix A Minimum Energy Model	33
Appendix B Electrohydrodynamic Model	35
Appendix C Operation Principles of the Quadrupole Mass Spectrometer	37

Abstract

Theoretical modelling using the maximum entropy formalism indicates that droplet charging in electrostatic sprays will exhibit phase transition-like behavior. This research is directed to the collection of detailed electrostatic spray data and their interpretation in terms of theoretical models of charged sprays. It involves the design and construction of a low charge-to-mass ratio quadrupole mass spectrometer and an accompanying vacuum-sprayer facility. Via a high speed electrometer, the electrostatic spray is analyzed at various charge-to-mass ratios to determine its charge and size distributions. A comparison of the initial Octoil data with the maximum entropy model provides the first direct evidence for the predicted phase transition-like behavior in spray charging. In addition, the previously published value for the characteristic electrostatic spray constant ($-\alpha'/\beta'$) is confirmed. The ability of this facility to provide detailed charge and size distributions can facilitate close examination of other factors that may affect the characteristics of the electrostatic sprays.

Chapter I

Electrostatic Atomization

1.1 Introduction

Fluid atomization is a key process in engineering. Its applications include combustion, chemical deposition, colloid production, space propulsion, and spray painting to mention a few. Various devices are available for spray production including air atomizers, swirl atomizers, and impact atomizers. These devices use aerodynamic shear force, centrifugal force, and impact disruption respectively to achieve atomization. Electrostatic atomization, in which stresses are electrically applied to cause atomization, is yet another means of producing sprays.

In these sprays, unique properties are observed as a result of the free electrical charges present in the spray droplets. The spray cloud becomes self-dispersive due to the mutual repulsive forces among charged droplets of similar polarity. The motion of the spray cloud is limited by space charge effects and the droplets have an affinity for electrically grounded objects. The electrostatic spray must be characterized by both a charge distribution and a size distribution.

The primary goal of this research is to examine the two fundamental properties of the electrostatic sprays, the charge and size distributions. For this purpose a new experiment has been constructed involving a quadrupole mass spectrometer and a high speed electrometer that permit both the spray droplet charge-to-mass ratio and the charge to be independently measured.

1.2 Electrostatic Atomization Phenomena

Electrostatic atomization can be easily achieved with simple apparatus. Figure 1.1 illustrates the operation of a *diode-type* sprayer⁴. Spray fluid is contained in the reservoir (or a capillary) having an orifice at the apex into which a conducting wire is dipped. This arrangement allows the potential of the fluid to be raised with respect to the electrical ground. At high potentials, the fluid meniscus at the orifice is drawn into fluid filaments. Instabilities then develop along these filaments causing them to break up into charged droplets.

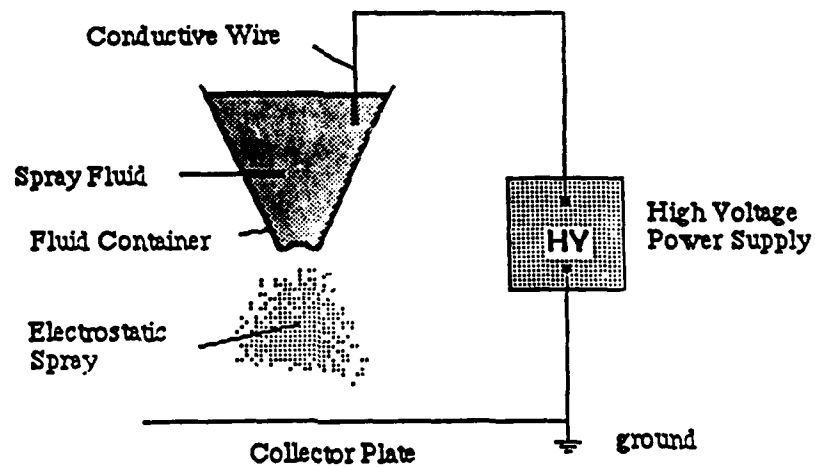


Figure 1.1 Simple Diode Sprayer

This phenomena was first described by Bose in 1745 and more recently by Zeleny^{5,6}, who was interested in the breakdown phenomena of various liquid and metal point conductors when they were raised to high potentials. Zeleny found that the discharge current from the liquid points is carried mainly by charged liquid droplets (the remaining current being carried by ions and electrons). It was an early belief that the applied potential on these liquid points governed the atomization process. Further experiments performed by Drozin⁷ concluded that it was the electric field rather than the applied potential that was causing the spraying.

Various theoretical studies have been published on electrostatic atomization. Most of these invoke stability analysis of the charged fluid surfaces, from which stability criterion for the surface and the most probable charge-to-mass ratio of the droplet is derived as a result of unstable surface perturbations^{8,10}. The stability criterion derived for spherical liquid droplets is due to Rayleigh¹¹. Rayleigh demonstrated that a limit, known to us now as the Rayleigh Limit, exists for the charge-to-mass ratio of a droplet of given size. At this limit the stabilizing surface tension force is just balanced by the destabilizing electrostatic force. This is an important limit for electrostatic atomization because it restricts the size of a droplet if its charge-to-mass ratio is fixed. Since Drozin's experiments showed that the charge-to-mass ratio of the droplet formed is proportional to the charging electric field, it follows that the Rayleigh Limit is a physical limit which governs the maximum size of a liquid droplet to be formed under a specified set of sprayer operating conditions.

Another charged fluid surface study was performed by Taylor^{12,13}. He found that, under the influence of an electric field, a charged liquid meniscus deforms from a hemispherical geometry to that of a cone (now known as the *Taylor Cone*). This cone sustains a characteristic semi-vertical angle of 49.3 degrees. The Taylor Cone has been experimentally verified for both hydrocarbon fluids and liquid metals. At the tip of these cones, liquid is drawn into filaments which subsequently break up into droplets. This mode of charged droplet formation is to be contrasted to the droplet break up when a charged droplet reaches the Rayleigh Limit. In an electrostatic spray, both mechanisms are believed to be operating at the same time.

The sprayer used in this thesis is one that utilizes the Taylor Cone for droplet formation and dispersion.

1.3 Models and Experimental Data

Three classes of models of the electrostatic sprays have been published -- the electrohydrodynamic, the minimum energy, and the maximum entropy models. The electrohydrodynamic model is accurate in describing the break up of a single charged liquid filament under the influence of external perturbation. However, this model is not very good for describing electrostatic sprays because in a sprayer like the one shown in Figure 1.1, many fluid filaments are usually formed. Since the actual number of filaments cannot be predicted beforehand, it is not practical to use this model to predict, for example, the charge-to-mass ratios of the droplets formed.

The other models were formulated to circumvent the difficulties involved in the modelling of the detailed breakup process during atomization. The characteristic of these models is that they ignore the complicated macroscopic details during breakup, using instead thermodynamic conditions about the system to derive the equilibrium state. Therefore, these models are end-state models in which only the initial and the final state of the spray system is of importance.

The minimum energy model was developed by Hendricks¹⁷ using a concept proposed by Vonnegut¹⁶. The model assumes that all observed droplets are formed from larger droplets which are at the Rayleigh Limit. As a result, the surface of these droplets becomes unstable to external perturbations. They eventually break into droplets of smaller diameter and having a different charge-to-mass ratio than the parent droplet. Assuming the final droplets are monodisperse (i.e. equal in size) and each having the same charge-to-mass ratio, an expression for the combined electrostatic and surface energy can be obtained. The combined energy may be minimized with respect to the radius by taking its derivative. This thermodynamic condition then yields the most probable droplet size and charge-to-mass ratio.

This derivation is valid when the spray is monodisperse, but the production of such

sprays is extremely difficult in practice. Usually, some spread is observed around the mean droplet size. Therefore, this model can only give rough estimates of the size and charge-to-mass ratio due to the simplifying assumptions made in the derivation. (The minimum energy and the electrohydrodynamic model are presented in Appendix A and B)

The maximum entropy model, developed by Kelly², considers the electrostatic spray to be an isolated thermodynamic system. At equilibrium, the entropy of the system is maximum. Since the entropy of a system is proportional to its degrees of freedom, an analytical expression for the entropy can be obtained by enumerating all the possible states of the system. The equilibrium end state is then obtained by maximizing the entropy with the system's conservation equations as constraints (i.e. conservation of mass, energy, and charge). Additional details of this theory will be discussed in the following chapter. A further point to be made for the three models is that the minimum energy and the electrohydrodynamic models predict only the charging characteristic of the sprays while the maximum entropy model is capable of predicting both the charging and size characteristics.

Despite the growing interest in and increasing applications of electrostatic sprays, little fundamental data are available, and very few fluids have been studied. The major difficulties in obtaining data are due to the large number of droplets produced in an electrostatic spray device and their generally small size -- typically in the micron range. To produce a set of meaningful data, it is necessary to make charge and size measurements simultaneously at a reasonable rate. As a result, most studies are limited in scope. Precise measurements of charge-to-mass ratio and mass of a single droplet are sparse. Experimentalists often have had to resort to crude estimates of these important parameters to infer the characteristics of the spray.

Only three sets of data for, Octoil¹, Wood's metal¹⁸, and glycerine¹⁹ have been published. Of the three sets, the Octoil data, while the most detailed, is still far from complete. These data, published by Hendricks, are shown in Figure 1.2. Each point on the figure represents a single charged droplet measured. This, unfortunately, represents the sole data available. To obtain a better understanding of the electrostatically driven atomization process, a

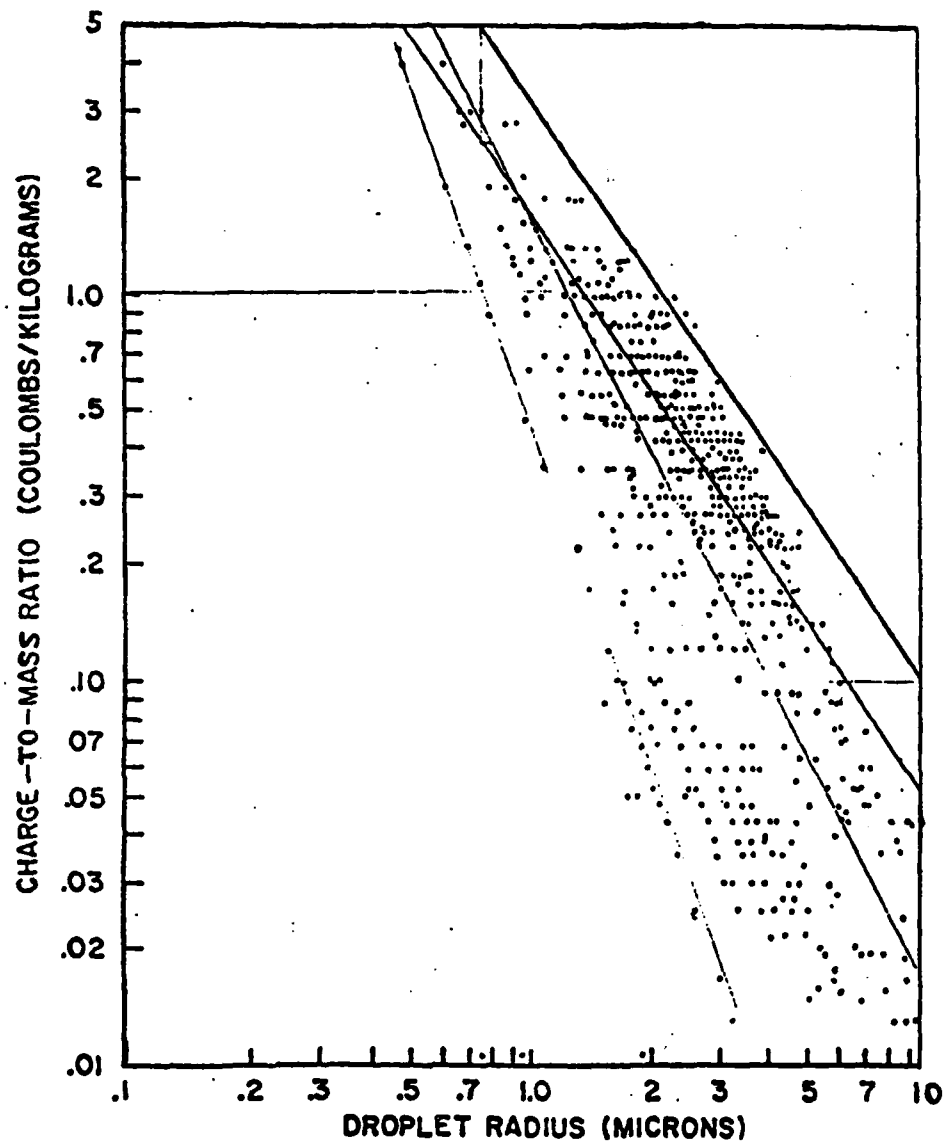


Figure 1.2 Hendricks' Data

more comprehensive data base is required.

1.4 Summary of Results

All of the parameters introduced in the maximum entropy model can now be numerically evaluated. Examination of these results shows that the model is self-consistent. Comparison of the present data with existing Hendrick's data reveals that the finite electrical conductivity of Octoil can cause underestimations of droplet radius. A correction factor based on conductivity variation with volumetric charge density is introduced to correct the error. The size and charge distribution at various charge-to-mass ratios for an Octoil spray are measured in this research. Comparison of the initial Octoil data with Hendrick's shows good agreement.

Regression analysis shows that the experimentally determined size distributions correlate well with the maximum entropy model. The close agreement confirms the multimodal nature of the size distribution claimed by the model. This indirectly implies the existence of a phase transition-like behavior in the charging characteristic. However, more conclusive evidence will require the examination of the size distribution at very high charge-to-mass ratio ($> 5 \text{ C/kg}$) which are inaccessible at the moment due to instrumental limitations. Consistently higher limiting surface electron field emission field strengths are found in certain distributions of droplets. This result suggests possibly different surface properties of the droplets in these spray distributions and should be the focus of additional research.

Chapter II

The Maximum Entropy Model

In electrostatic sprays, the quantities that are of interest to engineering applications are the distributions of the charge-to-mass ratio, the charge, and the size of the droplets. In addition, the variance of these distributions, the spray's penetration depth, and the size range are important parameters to observe. The three classes of models mentioned in the Chapter I, however, do not attempt to model all of these properties of the spray. Ultimately, what is desired in a spray model is its ability to predict these properties from specification of just a few parameters such as sprayer voltage, fluid flow rate, and fluid properties.

The minimum energy model describes the variation of charge-to-mass ratio as a function of average radius in a charged spray. In the electrohydrodynamic model, the charge-to-mass ratio is modeled as a function of average droplet radius, mass flow rate, and the geometry of the sprayer. In the maximum entropy model, the charging characteristic of an equilibrium spray cloud is related to the droplet radius and other fluid properties. Applying the same formalism, Kelly is able to model the atomization process thereby deriving the size distribution model. However, none of these models has yet been able to describe the distribution of the charge-to-mass ratio in a spray. In areas such as space propulsion and non-impact printing, accurate control of the particle beam's charge-to-mass ratio is crucial for the purpose of particle focusing. Thus, attaining a model capable of describing the charge-to-mass ratio distribution in a spray is the next step in the theoretical modeling work.

2.1 Maximum Entropy Model

In the maximum entropy model, no effort is made to model the macroscopic breakup process during spray formation. The model seeks to obtain the most probable size distribution of a charged spray when it is in thermodynamic equilibrium. The problem may be posed in the following way: Given a fixed mass of liquid M , total energy E and total free charge Q , what is

the most likely equilibrium size and charge distribution when the liquid is atomized? The model takes advantage of the long range coulombic interaction between charged droplets which produces a well-mixed state of fluid and charge. The electrostatic interaction is assumed to promote rapid equilibration within the spray.

The model, developed by Kelly², assumes that two independent processes are occurring simultaneously; the atomization and charging process. From this assumption, the droplet size distribution can be modeled independently of the charge distribution. The derivation is very similar to the statistical mechanical derivation of the most probable state of an isolated system of ideal gas molecules.

From statistical mechanics, an isolated system attains thermodynamic equilibrium when its entropy is maximized. The system entropy is related to the degrees of freedom of the system. Thus, to obtain an expression for the system entropy, one must be able to write an analytical expression for the degrees of freedom. The fundamental expression for the entropy s , is given by $s = k \ln(w)$, where k is the Boltzmann's constant and w is the degrees of freedom of a particular system state. In this case, a system state is identified as a particular distribution of droplet charge and size. The degrees of freedom of a system state is also its degeneracy. For the atomization process the degeneracy is prescribed by the Maxwell-Boltzmann²² statistics, while the degeneracy of the charging process is prescribed by Fermi-Dirac²² statistics. These statistics enable us to express w analytically.

From $s = k \ln(w)$, we can find the most probable state by looking for a state of maximum w since s is a monotonic increasing function of w . Mathematically, the most probable state is determined by the standard Lagrangian Multiplier Method. Such a method requires a constant to be introduced with each conservation law applied to the system. In this case three constants (or Lagrange Multipliers) α' , β' , and δ' are assigned to the conservation of charge, energy, and mass respectively. The resulting set of equations from the Lagrangian method are as follows:

$$\frac{\ln Z - \ln(1-Z)}{Z \ln Z + (1-Z) \ln(1-Z)} = -\alpha' \hat{r}^{3/2} - \beta' \frac{4\gamma q}{\epsilon_0 E_s} \hat{r}^2 Z \quad (2.1)$$

$$\ln N_d = [\alpha' Z + \beta' \frac{\gamma q}{\epsilon_0 E_s} (1+2Z) \hat{r}^{1/2} + \delta' (\frac{4}{3} \frac{\rho \gamma q}{\epsilon_0 E_s}) \hat{r}^{3/2}] \hat{r}^{3/2} \quad (2.2)$$

where equation (2.1) is an implicit equation describing the charging characteristic and equation (2.2) describes the size distribution. These equations define a statistically favorable state of the observed spray cloud at equilibrium.

In the maximum entropy model, the Rayleigh Limit¹¹ defines a non-dimensional charging parameter, Z , which is the ratio of the number of droplet surface electrons to the maximum number allowed. The surface electron field emission strength, E_s , identifies another limit in the electrostatic spray. The charge on a droplet is such that it cannot cause a surface field in excess of E_s . At small droplet radius, the amount of charge allowed on the droplet is limited by the critical emission field strength. However, at larger radius, the charge on the droplet is limited by the Rayleigh Limit. This is because the Rayleigh Limiting charge is proportional to the 3/2 power of the radius while the field limiting charge is proportional the square of the radius. Using E_s and the surface tension γ , a natural scaling length can be introduced into the model, of the form:

$$r_x = \frac{4\gamma}{\epsilon_0 E_s^2} \quad (2.3)$$

where r_x is known as the cross-over radius. Physically, the cross-over radius is the characteristic radius of a charged droplet at which it is equally likely to undergo a Rayleigh type breakup or surface electron field emission to relieve its surface electrostatic stress (for Octoil, the cross-over radius is approximately 3.3×10^{-4} microns). The droplet radius in the maximum entropy model is normalized with the cross-over radius,

$$\hat{r} = \frac{r}{r_x} \quad (2.4)$$

2.2 Preliminary Results of Maximum Entropy Model

The maximum entropy model was compared to Hendrick's Octoil⁴ and Wood's metal¹⁸ data by Kelly. Because experimental size distributions were not available, only equation (2.1) was tested. In this research, the theoretical size distribution equation (2.2) is checked with the experimental size distributions.

Figure 2.1 depicts the data for Octoil and Wood's metal, each data point on the graph represents an averaged radius from the group of droplets detected at the same charge-to-mass ratio. Using these data and equation (2.1), the two Lagrangian multipliers α' and β' can be determined for the fluids. Their values are listed below:

<i>Wood's metal</i>	$\alpha' = -0.18$	$\beta' = 1.7 \times 10^{16}$
<i>Octoil</i>	$\alpha' = -0.82 \times 10^{-4}$	$\beta' = 7.5 \times 10^{12}$

Using these values for α' and β' , the charging equation (2.1) can be solved numerically. It turns out that for both Wood's metal and Octoil, a critical charge-to-mass ratio exists below which multiple solutions of average droplet radius are found for a given charge-to-mass ratio. Above this critical ratio, a single solution for average radius is found for each charge-to-mass ratio of the charging equation. Each of these solutions for the radius represents the averaged radius of an individual distribution of droplets. Thus, for the multiple solution case, one would expect the observed distribution to be composed of three smaller distributions.

Figure 2.1 shows the solution for the charging equation that best fits the published experimental data. The volumetric charge density is plotted against the radius because it is a

more appropriate unit of engineering interest (the volumetric charge density is defined as the product of the charge-to-mass ratio and the fluid density). This solution branch, for the moment, is designated as the B Branch. The other solutions are each designated as the A and C Branch respectively.

The B Branch is of special interest because on it, the charging equation (2.1) may be simplified for large droplets. For the observed data of Octoil and Wood's metal, the assumption of large droplets holds for the range of sizes observed³⁰. This simplification allowed the charging equation to be written into the form:

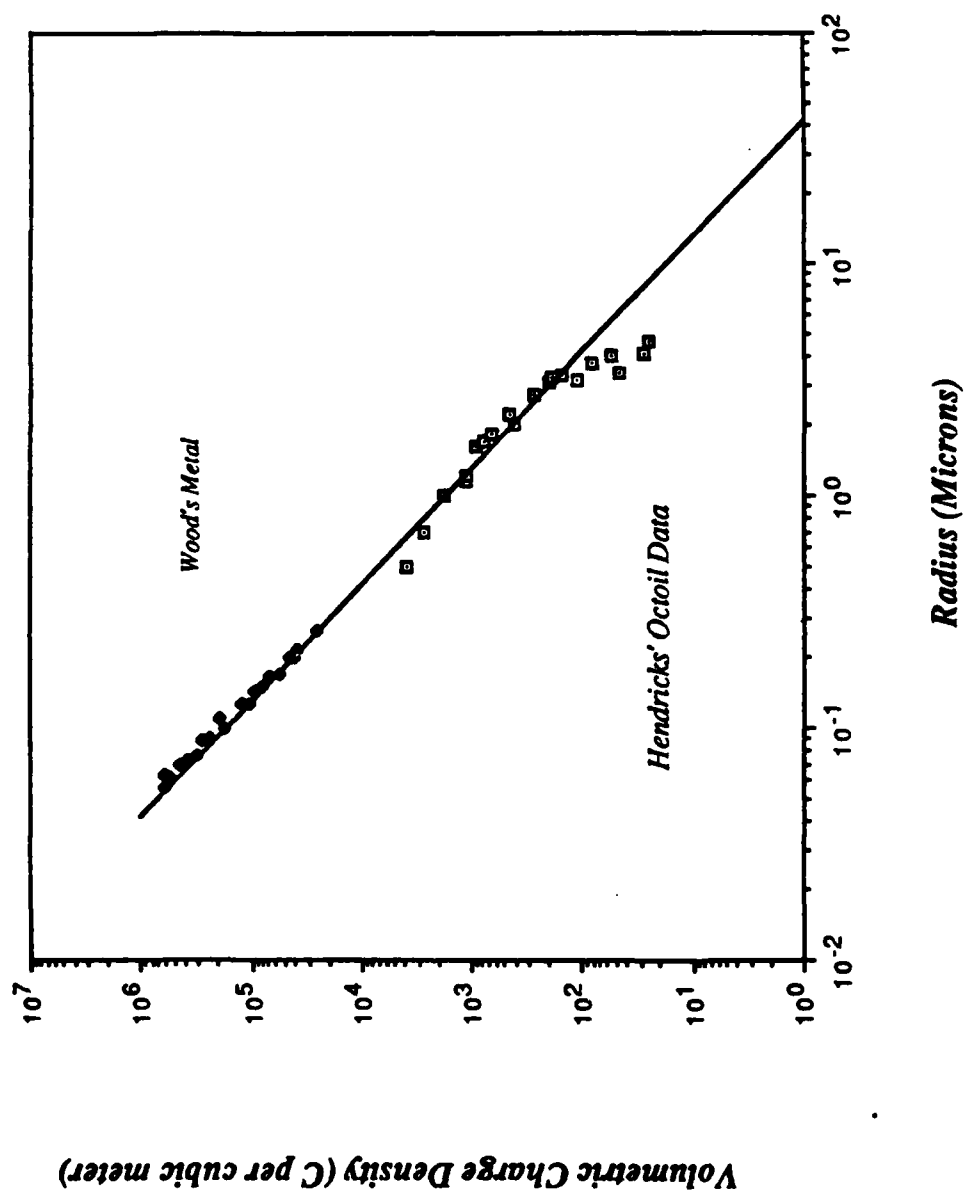
$$d^2 = - \left(\frac{\alpha'}{\beta'} \right) \frac{12\epsilon_0}{q\rho_e} \quad (2.5)$$

where d is the diameter of the droplet, q is the elemental charge, ϵ_0 is the permittivity of free space and ρ_e is the volumetric charge density.

Figure 2.1 reveals that the simplified charging equation (2.5) correlates well with the published data. Therefore, this equation can predict the average droplet size when the volumetric charge density is specified. For hydrocarbon fluids such as diesel, the "large" radius regime that facilitate the simplification corresponds to droplet sizes of 10 microns and above. These are sizes of special interest in engineering, particularly in the area of combustion research.

Equation (2.5) relates the diameter of the droplet to its volumetric charge density. For a given fluid, the ratio $(-\alpha'/\beta')$ is a constant. Two points were stressed in Kelly's work on this simplified charging equation. Firstly, the value $-\alpha'/\beta'$ evaluated for Wood's metal and Octoil were very close. This is counter intuitive because the two fluids are very different in terms of their densities, viscosities, and surface tensions, furthermore, Wood's metal is electrically conducting while Octoil is a dielectric fluid. The physical significance of $-\alpha'/\beta'$ should therefore deserve further examination. Secondly, equation (2.5) is not a function of fluid properties. This is in contrast to the case of uncharged sprays where the spray properties are dependent on the

Figure 2.1 Octoil and Wood's Metal Data



properties of the fluid being atomized.

Therefore, at large droplet radius, the size of the droplet can be correlated to the volumetric charge density alone. For conducting fluids like Wood's metal more charge can be injected into the fluid. This causes a larger electrostatic repulsive force on the surface and the Rayleigh Limit is attained at a smaller radius; as a result, smaller droplets are observed. For Octoil, charge injection is not as efficient due to its dielectric properties. This causes larger droplets and therefore lower charge densities to be observed in the spray.

2.3 Further Verification of the Maximum Entropy Model

We have seen that using the existing data, only two of the three Lagrangian Multipliers can be evaluated. To obtain further information on the model, the published data are insufficient. From this facility, full characterization of the spray can be obtained in terms of detailed size and charge distributions. This not only allows us to obtain a more accurate average of the previous data, it also facilitate the testing of the size distribution model. By appealing to the size distribution model and the size distribution data, we can proceed to evaluate the δ' multiplier. In addition, α' and β' can also be found from this exercise thereby allowing comparison of their values with those obtained from Kelly's work.

Chapter III

The Electrostatic Atomization Experiment

This chapter describes the experimental facility constructed to collect electrostatic spray data. The results and predictions of the maximum entropy model is further examined in the light of the new data. Data for Octoil from this experiment is tested against Hendrick's; this enables a calibration of the facility. Other fluids can, in turn, be sprayed so as to build up a detailed set of fundamental spray data.

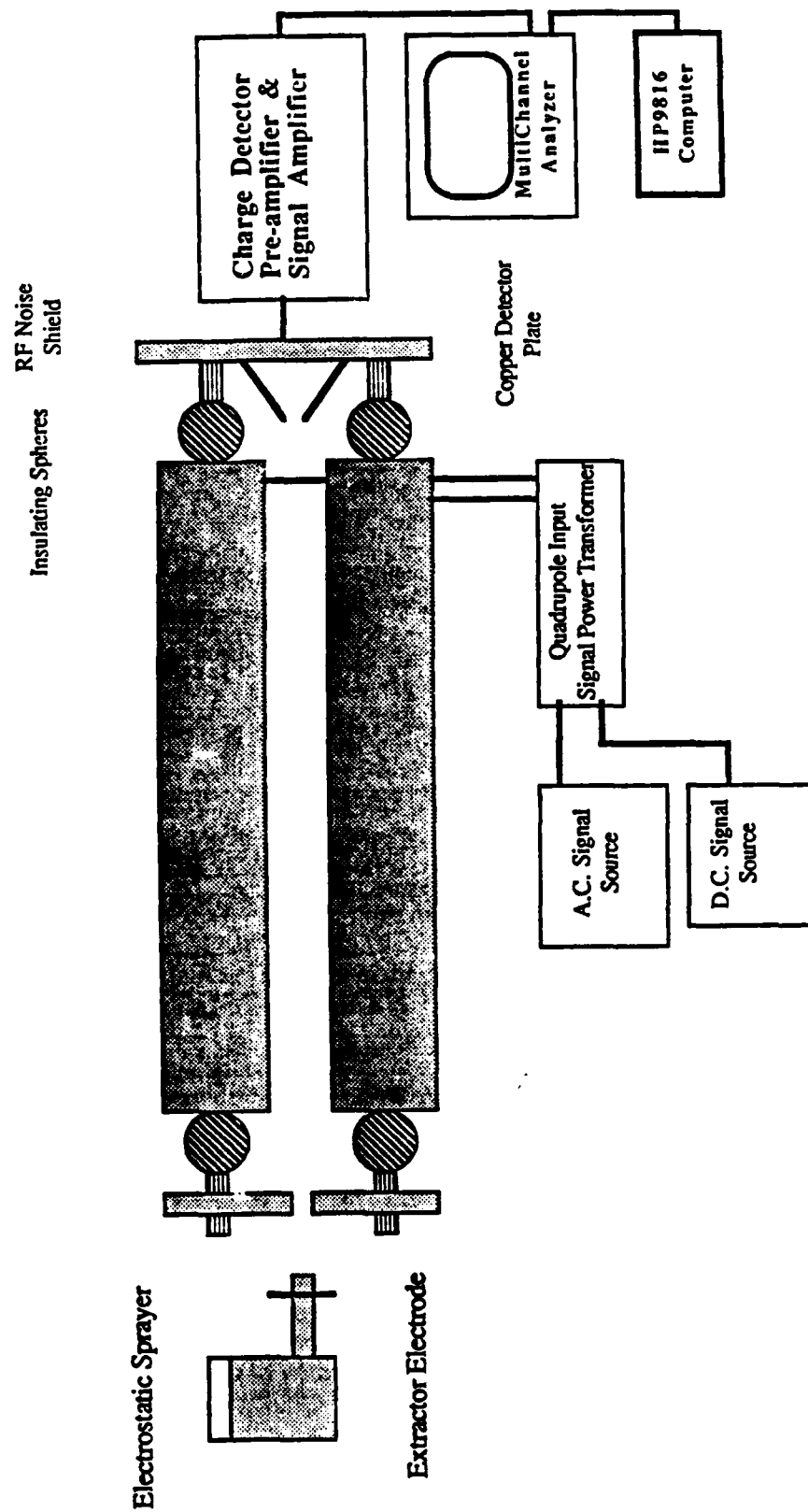
The facility described here resembles closely to the Hogan and Hendrick's apparatus²⁰. A schematic diagram of the experiment and a photograph of the experimental set-up are shown in Figure 3.1 and 3.2. The electrostatic spray is examined at various charge-to-mass ratios with the quadrupole mass spectrometer. Droplets with the pre-selected charge-to-mass ratio are extracted from the main droplet beam. The free electron charges on these droplets are then determined with a high speed electron sensitive pre-amplifier²⁴. These charge data are cumulatively collected on a multichannel analyzer (MCA) which yields the charge distribution of the spray at the selected charge-to-mass ratio. By assuming that the droplets are spherical the size distribution can in turn be calculated.

A vacuum facility is required for the operation of the quadrupole mass spectrometer. The complete sprayer-mass spectrometer-charge analysis system is maintained under a vacuum of 1×10^{-6} torr. Data collected on the MCA are transferred via fiber optic data-link to a HP9816 personal computer for preliminary reduction. This processed data is then sent to the Princeton University mainframe IBM 3081 computer for regression analysis. The purpose of the regression analysis is to examine the goodness-of-fit of the model with the measured data.

3.1 Charged Droplet Production/Vacuum Facility

Charged droplets are produced using the simple diode-type sprayer shown in Figure 3.3. The sprayer consists of a metallic capillary needle of inner diameter 0.01" (1/4 mm) and outer diameter

Figure 3.1 Schematic of Experiment



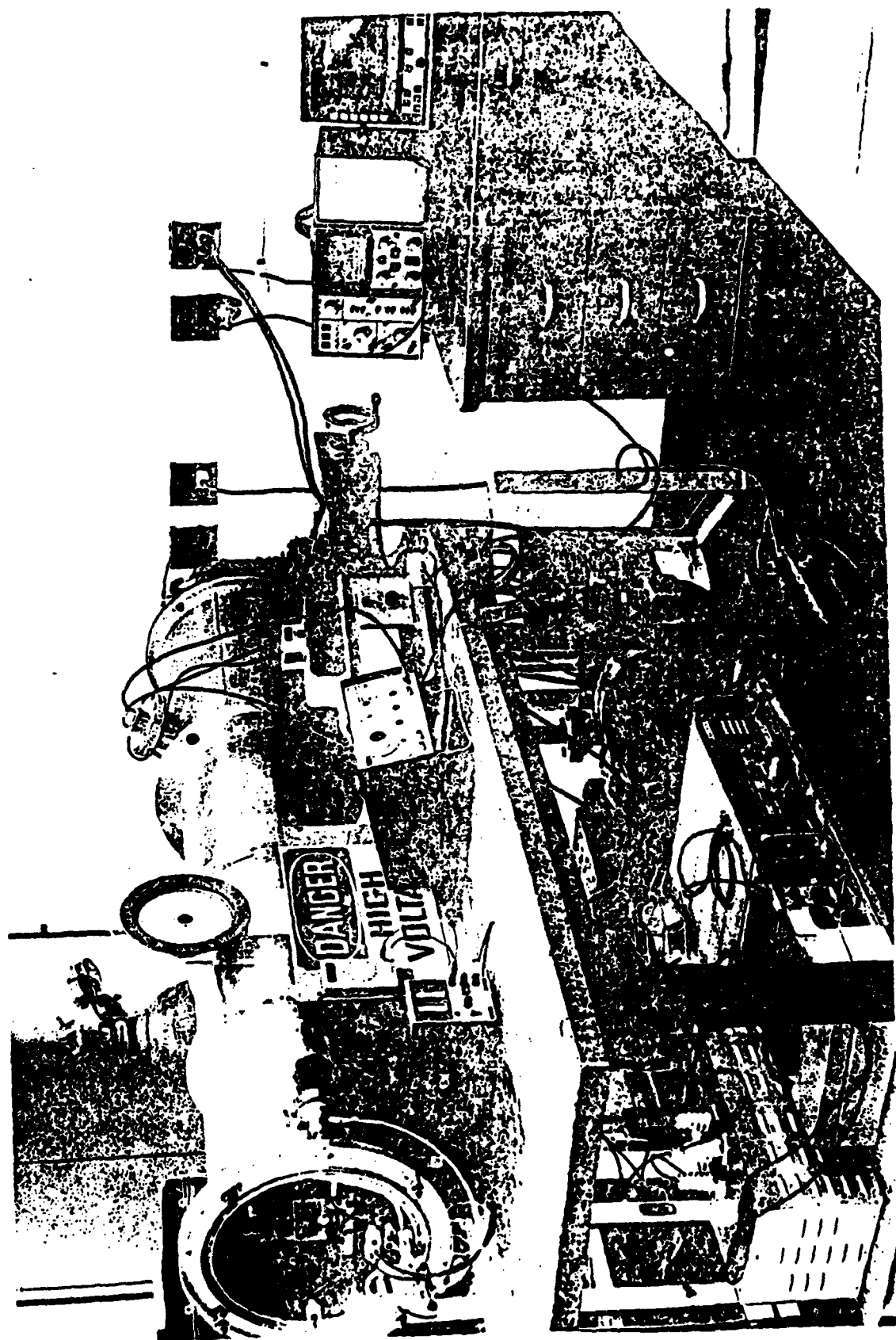


Figure 3.2 Photograph of Facility

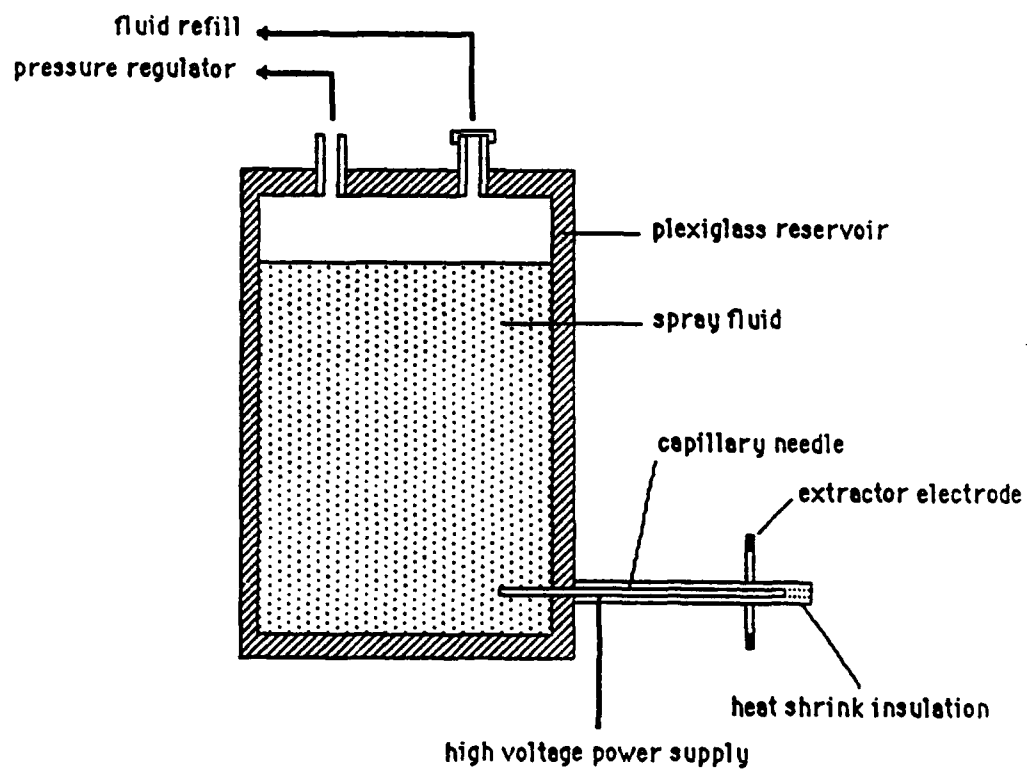


Figure 3.3 Diagram of Reservoir and Sprayer

0.02"(1/2 mm), inserted into a plexiglass reservoir. The flow rate of the sprayer can be controlled by regulating the pressure over the fluid in the reservoir; pressures up to 760 torr can be applied. The capillary needle is connected to a high voltage source capable of voltages up to 20 kV.

To achieve atomization the potential of the needle is raised to 14 kV with a reservoir pressure of 45 torr. Since it is the electric field that is responsible for the atomization, a electrically grounded ring-electrode (also known as an extractor electrode) is positioned coaxially around the needle to provide the required field for spraying. To prevent corona discharge at the needle tip, an insulating jacket made from heat shrink tubing is placed over the entire length of the capillary needle. It is found, through extensive tests, that the sprayer works most satisfactorily if this jacket is extended over the tip of the needle by a millimeter or two. This enables a column of fluid to insulate the needle tip preventing breakdowns. Smooth operation of the sprayer requires careful adjustments of the flow rate (i.e. reservoir pressure) and the charging voltage. If the charging voltage is too high or if the flow rate is too low, breakdown will occur due to the depletion of spray fluid which exposes the sharp needle tip. Breakdowns may also occur in the dielectric fluid if the electric field at the tip is too high. Considerable effort has been devoted to avoiding arcing since it damages the surface of the capillary needle and causes false recordings in the multichannel analyzer.

The charged droplets are accelerated by the extractor electrode toward the quadrupole mass spectrometer. Droplets are typically accelerated to a velocity of 150 - 200 m/s. The 8mm diameter entrance aperture to the quadrupole limits the radial velocity component of the charged droplets thereby ensuring proper filtering in the mass spectrometer^{34,35}.

3.2 Quadrupole Mass Spectrometer

Two pieces of information are required to characterize a single charged droplet, namely its charge and size. From these data, other quantities such as mass, surface electron density, electrostatic stress, and surface energy can be derived. Early versions of electrostatic spray experiment utilize

time of flight method to deduce these quantities⁹. This method is admissible when the charge on the droplet is relatively large because at low charge levels the measurements have very small signal-to-noise ratios. Since the droplets of engineering interest have low charge and charge-to-mass ratios, other means of measurement must be used to obtain accurate data.

An alternative is to use a quadrupole mass spectrometer. By using the quadrupole as a mass filter only droplets with the selected charge-to-mass ratio are filtered from the droplet beam. If the charge of these droplets are subsequently measured, other information can be computed (e.g. droplet size and surface energy). Since the quadrupole can be operated continuously, less time is required to obtain a meaningful charge distribution than the time of flight instrument. Detailed operating principles and design criterion of the quadrupole mass spectrometer/power supply used in this research is described in Appendix C.

3.3 Charge Detection Assembly

The charge analysis system consists of an electrometer-amplifier combination manufactured by Amptek Inc. (model number A-225 and A-206 respectively). The electrometer has a charge sensitivity threshold of 280 electrons. For each charged droplet analyzed, a voltage pulse is generated with a characteristic pulse width of 10 μ sec and a rise time of 2.5 μ sec. The pulse height is proportional to the amount of charge detected in the droplet. The output voltage pulses are recorded on a multichannel analyzer (MCA) which then displays a population versus droplet charge distribution. Since a minimum threshold voltage is required on the MCA; therefore, small signals from the electrometer must be amplified. This unfortunately also amplifies the noise in the system.

While the droplet detection plate is being partially shielded from the quadrupole as shown in Figure 3.1, it is not sufficient to eliminate completely its noise pickup from the quadrupole's r.f. field. Because the applied frequency to the quadrupole rods is known, a filter is built to remove this "noise" contribution. Other random noise in the system cannot be completely eliminated. This problem is particularly serious at high gain settings on the amplifier. This

difficulty prohibits the collection of data at charge levels below 8000 electrons. Under this restriction, the smallest droplet size detectable is about one micron. Fortunately, this is still within the range of interest.

3.4 Experimental Procedure

In a typical experiment, the quadrupole voltage signals are calibrated first. This involves balancing the two a.c. voltage amplitudes and verifying their phase difference. A variable resistor is used to balance their amplitudes. The required d.c. bias voltages are computed from the program "MCAHP_SM" and fed in with the a.c. signals. These voltages are verified from a digital oscilloscope. Due to the bit resolution on the oscilloscope, an error between 1 to 3 % is usually associated with these signals.

Upon completing the voltage verification, the sprayer's fluid reservoir is pressurized to approximately 40 torr. This provides a positive flow rate through the 10 mil (i.d.) capillary needle. The needle charging voltage is increased slowly in small increments to permit equilibration. The quadrupole is de-activated during this initial stabilization process to evaluate the charge detector count rate, which provides a qualitative measure of the sprayer output.

Past experience indicates spraying in vacuum starts at approximately 13 kV. For this sprayer-extractor electrode configuration, voltages beyond 14 kV produces arcing, which if sustained can damage the capillary needle and the electronics of the MCA.

In a typical run, the sprayer is allowed to stabilize for a few minutes before the mass spectrometer is turned on. The droplet detection rate usually drops by a factor of ten when the mass spectrometer is activated because unwanted droplets are being filtered off. Approximately 1000 droplets are required to produce a useful distribution, this usually requires 3 to 5 hours of experiment time.

Chapter IV

Data Analysis and Discussion

4.1 Introduction

The size distribution of the spray is experimentally determined at various charge-to-mass ratios. Figure 4.1 shows the capability of the experiment in obtaining such data. The scanning charge-to-mass ratio of the quadrupole mass spectrometer is set at a value and bandpass ratio. The resultant MCA spectrum would then correspond to a narrow horizontal band extending rightward from the detector sensitivity limit in Figure 4.1. Plotted in Figure 4.1 also are the theoretical results of equation (2.1). The first order phase-transition behavior can be seen when the equation transits from single to multiple solutions.

For Octoil, the transition occurs approximately at 3.4 C/kg. Since we cannot, at the moment, examine charge-to-mass ratios greater than 2.9 C/kg we should therefore anticipate seeing multimodal-type size distributions. It is important to realize that the curves of Figure 4.1 represents the behavior of mean droplet size, thus, the observed MCA spectra should consist of more than one distribution centered on each these means.

4.2 Experimental Data

A typical spectrum taken from the MCA is shown in Figure 4.2 where the y-axis is the population number and the x-axis is proportional to the amount of charge detected from the incoming droplet. Droplets of low charge levels usually have a large population. It then drops off rather rapidly at higher charge levels. The number of data channels defining the peak of the distribution is small in comparison with the total number of channels in the distribution. This implies that the distributions have rather sharp peaks and is in contrast with the rather broad and smooth size distributions seen in uncharged sprays. These spectra also indicate required improvements to be made on low charge level data acquisition.

At higher charge-to-mass ratios, typically near the present limiting charge-to-mass ratio of

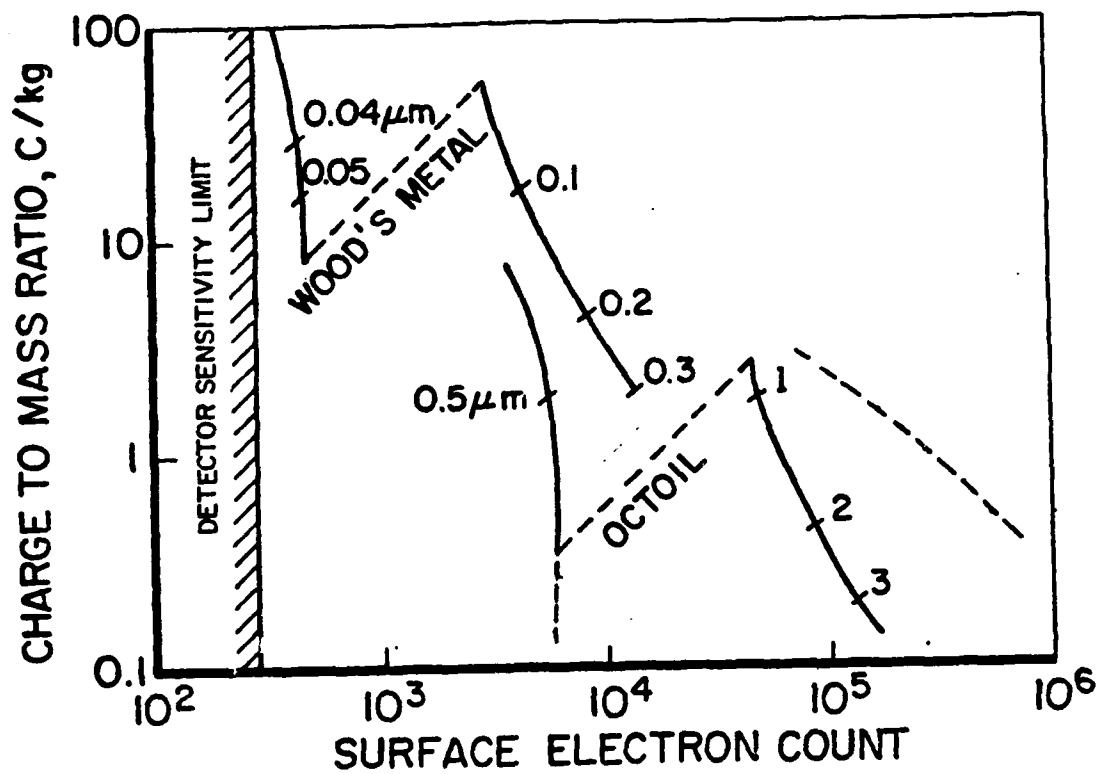


Figure 4.1 Capability of Experiment

Raw Data from MCA
(Octoil Data at 1.23 C/kg)

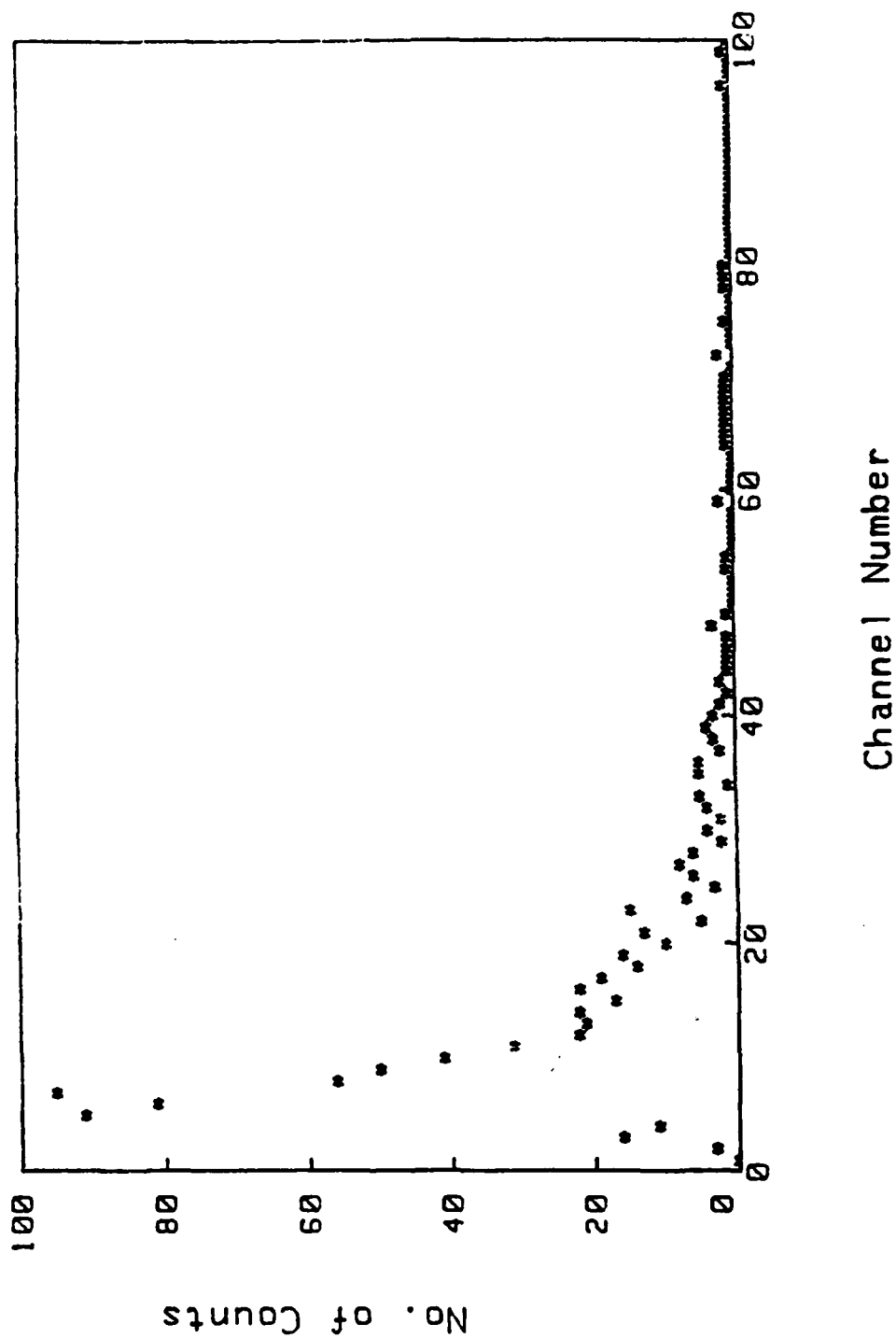


Figure 4.2 Raw Data from Multichannel Analyzer (MCA)

2.9 C/kg, some detected droplets were found to possess charging levels well in excess of the Rayleigh limit determined by the quadrupole charge-to-mass setting. This suggests that a portion of the droplets have not been effectively filtered by the quadrupole field. However, this phenomenon is only seen when the quadrupole is operating at its upper limit. Through more stable power supply, this deficiency can be eliminated. The small number of droplets having anomalous charging levels has no impact on the proper interpretation of the data as they are usually small in population and are not statistically influential.

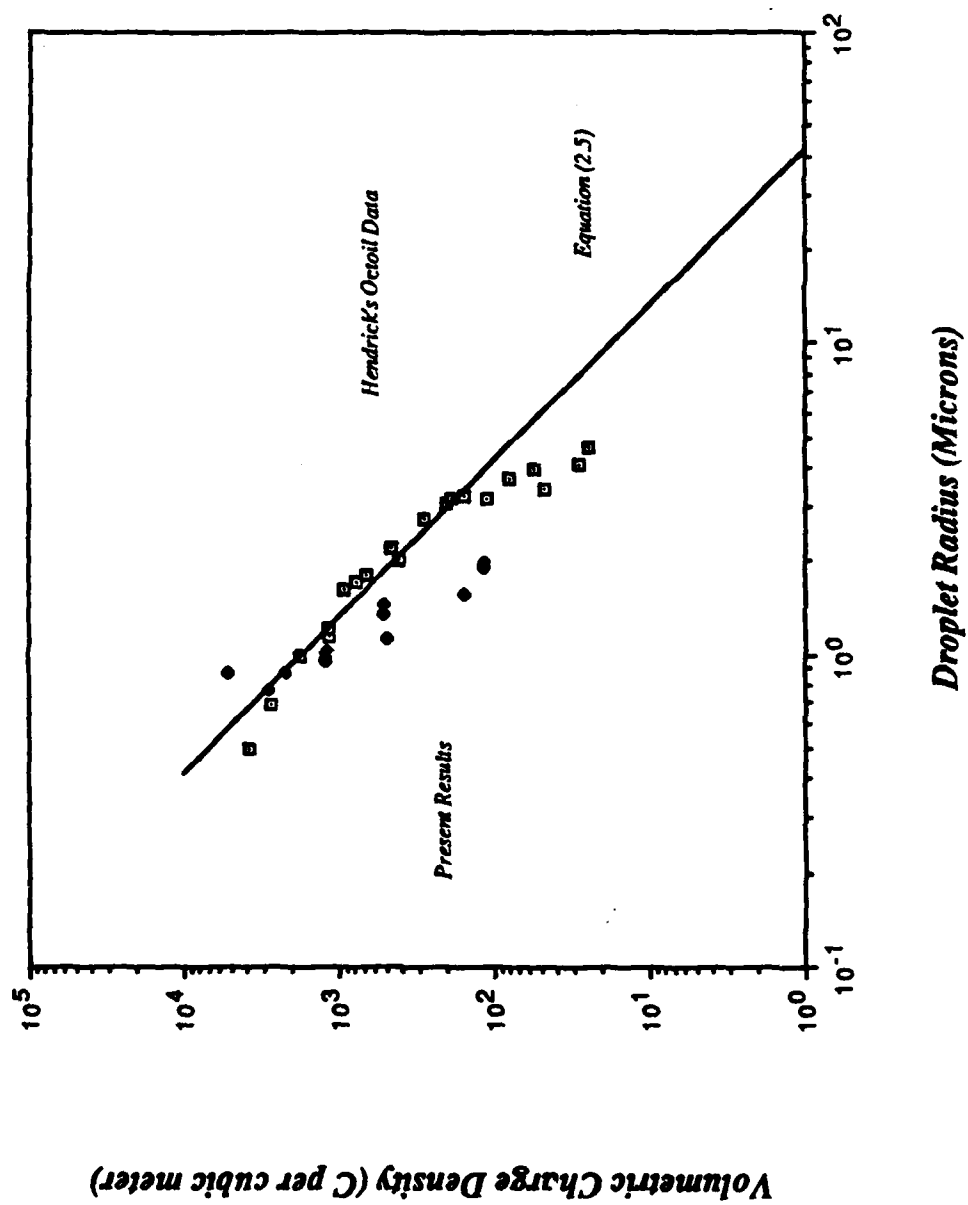
4.3 Comparison with Published Work

Collected from the experiment is a set of size distribution at various charge-to-mass ratios. As a first test of the experiment's consistency, the MCA spectrum data were simply averaged in accordance with the procedure used by Hendricks to represent his manually recorded data. Figure 4.3 shows a comforting level of agreement of the initial results with Hendrick's pioneering work. This provides confidence that the experiment is operating in an appropriately consistent manner.

A slight deviation between the two data set is apparent at low charge-to-mass ratios. Analysis of these data indicate that this deviation may be explained by the finite conductivity of Octoil which prevents the proper measurement of droplet charge within the electrometer response time of .002 msec. It is computed that only a fraction of the total charge can be transferred if the charge density of the droplet is low resulting in low electrical conductivity. As a result of the false measurement of charge, the computed size would be in error since the size of the droplet is computed from the knowledge of the charge-to-mass ratio and measured total charge of the droplet. In section 4.8, a method of correction will be discussed.

New data (shown in Figure 4.3) is checked with the charging equation (2.1) derived from the maximum entropy formalism. Again, of the three solutions predicted, the B branch was found to have the closest correlation with the data. The simplified form of the charging equation on this branch is given by equation (2.5). Using regression analysis the constant ($-\alpha'/\beta'$) is

Figure 4.3 Comparison with Published Data



re-evaluated. The value deduced using the new data is -53.7 eV which is approximately 15% from Kelly's earlier value. The relatively large difference from Kelly's value arises because equation (2.5) is not very sensitive to values of the ratio $(-\alpha'/\beta')$. Furthermore, there are probable errors inherent in the original Hendricks data which could account for the difference.

4.4 Size Distribution

The size distribution model was not validated due to the lack of size distribution data in the literature. With the experimental charge distribution data, it is possible to deduce the size distribution since the charge-to-mass ratio at which the charge distribution is obtained is known.

The size distribution model is specified through equation (2.2). However, we recall that from the solution of the charging equation, the size distribution should be multimodal. This is to say that the observed size distribution should be a convolution of three smaller distributions. The actual size distribution model is then a summation of three equations each with the form of equation (2.2):

$$N = \sum_A^C N_d = \sum_A^C \exp \left[\alpha' Z + \beta' \frac{\gamma q}{\epsilon_0 E_s} (1 + 2Z) r^{1/2} + \delta \left(\frac{4 \rho \gamma q}{3 \epsilon_0 E_s} \right) r^{3/2} \right] r^{3/2} \quad (4.1)$$

the summation represents the sum of the three branches A, B, and C. Using equation (4.1) and a standard non-linear regression routine, the size distribution model is tested with the data. The regression routine is supplied by SAS Institute Inc. and implemented on the Princeton University IBM 370 mainframe computer. The routine uses a non-linear Gauss-Newton Least Square method in its analysis.

Equation (4.1) is a function of the charging parameter Z and the normalized radius. The variable Z can be eliminated by relating it to the charge-to-mass ratio of the droplets. By writing the charge-to-mass ratio as:

$$\frac{Q}{M} = \frac{3}{4} \frac{Nq}{\pi r^3 \rho} \quad (4.2)$$

The charging parameter may then be introduced by dividing the numerator and denominator of the right-hand-side by N_{ray} , which is the number of electrons a droplet contains at the Rayleigh Limit at a given radius. Equation (4.2) thus becomes:

$$Z = \left(\frac{4}{3}\right) \left(\frac{Q}{M}\right)^{3/2} \frac{\gamma \rho}{\epsilon_0^2 E_s^3} \quad (4.3)$$

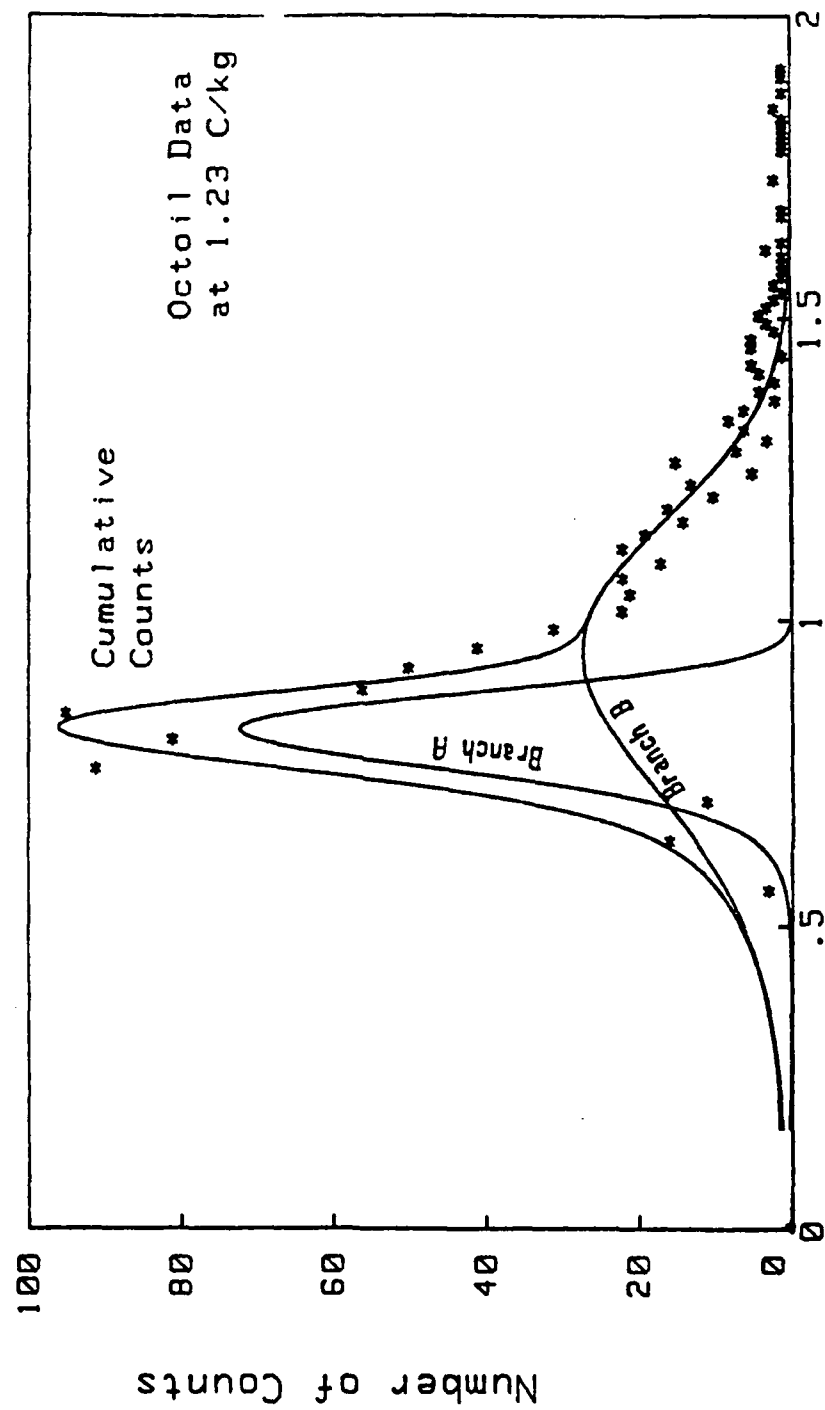
The advantage of using the above expression is therefore apparent because the experimental data have fixed charge-to-mass ratios. Using equation (4.3) it is then possible to eliminate one of the independent variables in the size distribution model. In this case, the size distribution becomes a function of the normalized radius only. The new model equation therefore becomes:

$$N = \sum_A^C N_d = \sum_A^C \exp \left[\alpha' \left(\frac{4\gamma q}{3\epsilon_0^2 E_s^3} \right) \left(\frac{Q}{M} \right) r^3 + \beta' \left(\frac{\gamma q}{\epsilon_0 E_s} \right) \left(1 + \frac{32}{9} \left(\frac{\gamma q}{\epsilon_0^2 E_s^3} \right)^2 \left(\frac{Q}{M} \right)^2 r^3 \right)^2 + \delta' \left(\frac{4\gamma q}{3\epsilon_0^2 E_s^3} \right) r^3 \right] \quad (4.4)$$

4.5 Regression Analysis Results

The regression analysis program uses equation (4.4) as an input model to examine its degree of correlation with the observed size data. All the MCA spectra examined indicate the absence of the C Branch. In other words, the experimental data could only be resolved into two individual distributions. These distributions, when compared to the theoretical results were identified to be the A and B Branch respectively. While it is unclear why the C Branch is absent, it is possible that the C Branch population is too low to be resolved by the analysis routine.

Figure 4.4 depicts the regression result of one of the observed size distributions. Three



Radius (Microns)

Figure 4.1 Multimodal Size Distribution

curves are generated in each of these analyses. The curves labeled A and B are the respective branches, while the third curve is the sum of the previous two. The correlation in general is very good as indicated by four statistical indicators for measuring the goodness-of-fit of the theoretical model.

The four indicators are the correlation coefficient, the sum of errors, the residual plot and the standard errors of the estimated model coefficients. Aside from two cases, all the size spectra examined yield correlation coefficients well over 0.9. This shows that over 90% of the data may be accounted for by the proposed model. The effectiveness of the model is further ensured by good behavior in other statistical indicators.

These results concluded that the observed spray size distribution is indeed multimodal. The possibility of a monomodal size distribution is being ruled out through a direct comparison of such a model with experimental data. Figure 4.5 shows that this model is incapable of reproducing the data. In fact, the monomodal model has a correlation coefficient of about 0.7 with the data. This result reaffirms the multimodal property of the size distribution.

4.6 Multiple Charging Characteristics

From the statistically resolved A and B branch, it is now possible to compare the experimental charging characteristics to the theoretically predicted ones. This is done in Figure 4.6 and 4.7. Discrepancies were observed in both figures. The data cannot be predicted completely from the model equations. Close scrutiny of the discrepancies reviewed that the deviation between theory and data were not constant but dependent on the charge-to-mass ratio. Such behavior was also observed in the comparison with Hendrick's data in the earlier section. In the branch A characteristic, the theory tends to underpredict the data while the opposite occurs for the branch B characteristic.

The differences between theory and data may be a result of the varying electrical conductivity of Octoil at different charge-to-mass ratios. This idea is examined through the assumption that the electrical conductivity of Octoil consists of two components. One of which

Size Distribution Computed from Model
DQM90 (Charge to Mass Ratio = 1.23 C/kg)

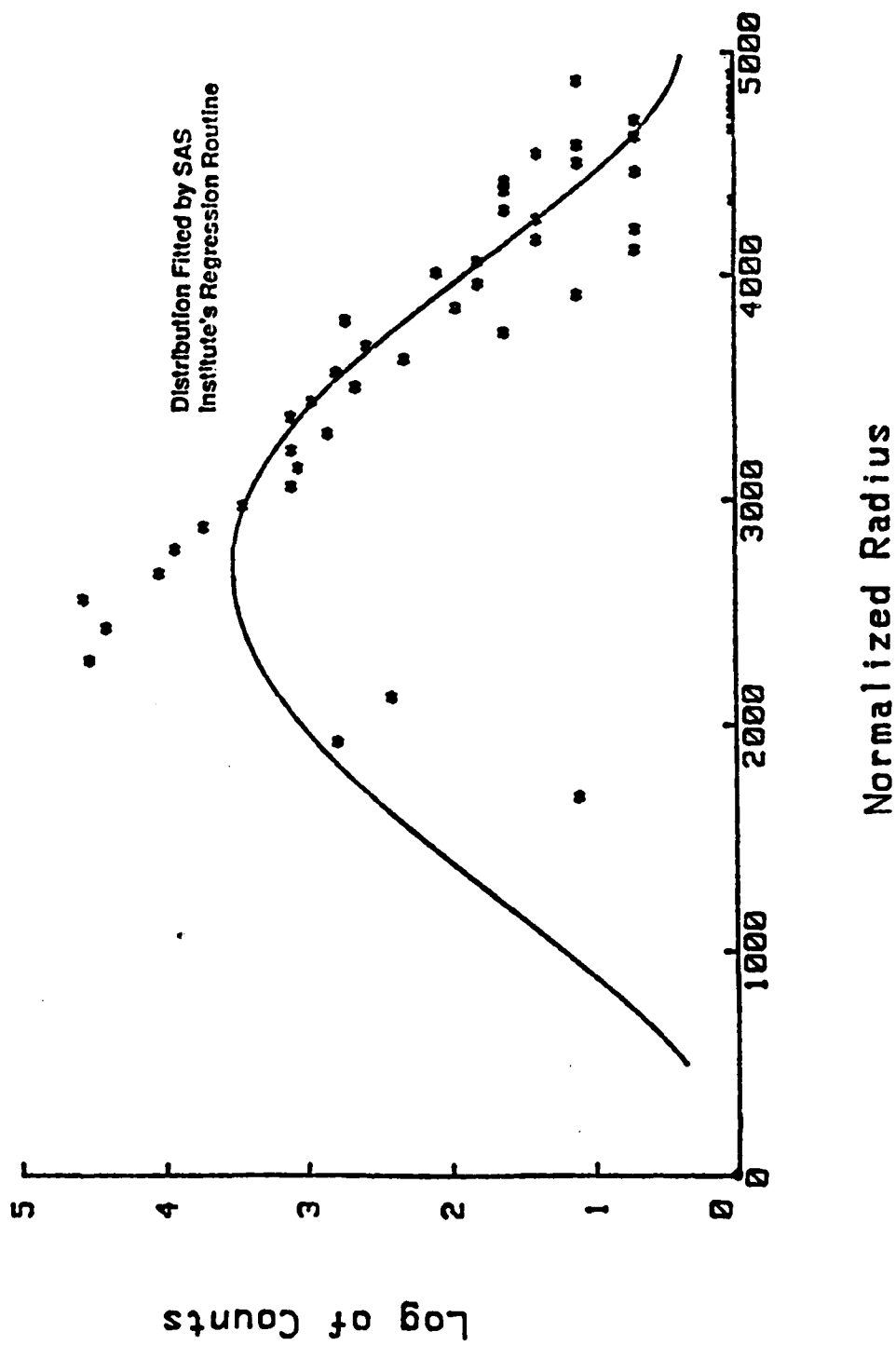


Figure 4.5 Monomodal Regression Result

is the residual conductivity of pure Octoil and the other contributed by the presence of excess charge carriers (i.e. free electrons). As noted in section 4.3, this idea could explain the deviation of the data which is charge-to-mass ratio dependent. A conductivity effect correction is then introduced to the experimental charging characteristics in Figure 4.6 and 4.7 to check the assumption.

The results of this correction are plotted in Figure 4.8 and 4.9. For both experimental characteristics, the correction has improved the correlation with the model. Aside from a biased shift, both the theoretical and experimental charging characteristics have the same dependence on the droplet radius. The question which remains is the cause of the biased shift that resulted in the non-overlapping of the experiment and theoretical charging characteristics. This could be resolved by using different values for E_s in the solution of the charging equation. It may be recalled that to solve the charging equation, several constants must be known and they are the two Lagrange multipliers and E_s , the limiting surface emission field strength. The Lagrange multipliers were evaluated by making comparison to the Hendrick's data while the value for E_s is an estimated quantity.

The value of E_s is difficult to obtain because surface emission depends on a variety of parameters such as surface conditions, ambient gas properties, and geometry of the surface concerned. Experiments conducted to determine its value is usually difficult to duplicate and the values fluctuate from test to test because it is not possible to control experimental conditions precisely. A study was performed to analyze the effect of E_s on the charging characteristics. This is accomplished by changing the value of E_s and solving for the charging characteristic for each of the values³². These calculation indicated that if a smaller value of E_s is assumed, the resulting charging characteristic will be shifted to higher radius; the opposite will occur if a larger value of E_s is used. Therefore, the discrepancies observed in Figure 4.8 and 4.9 could be a result of incorrect values of E_s used in solving the charging equation.

Since the value of E_s should be a constant for a given surface characteristic, difference in E_s could mean that droplets on the branches are exhibiting different surface properties. In

Figure 4.6 Branch A Charging Characteristic

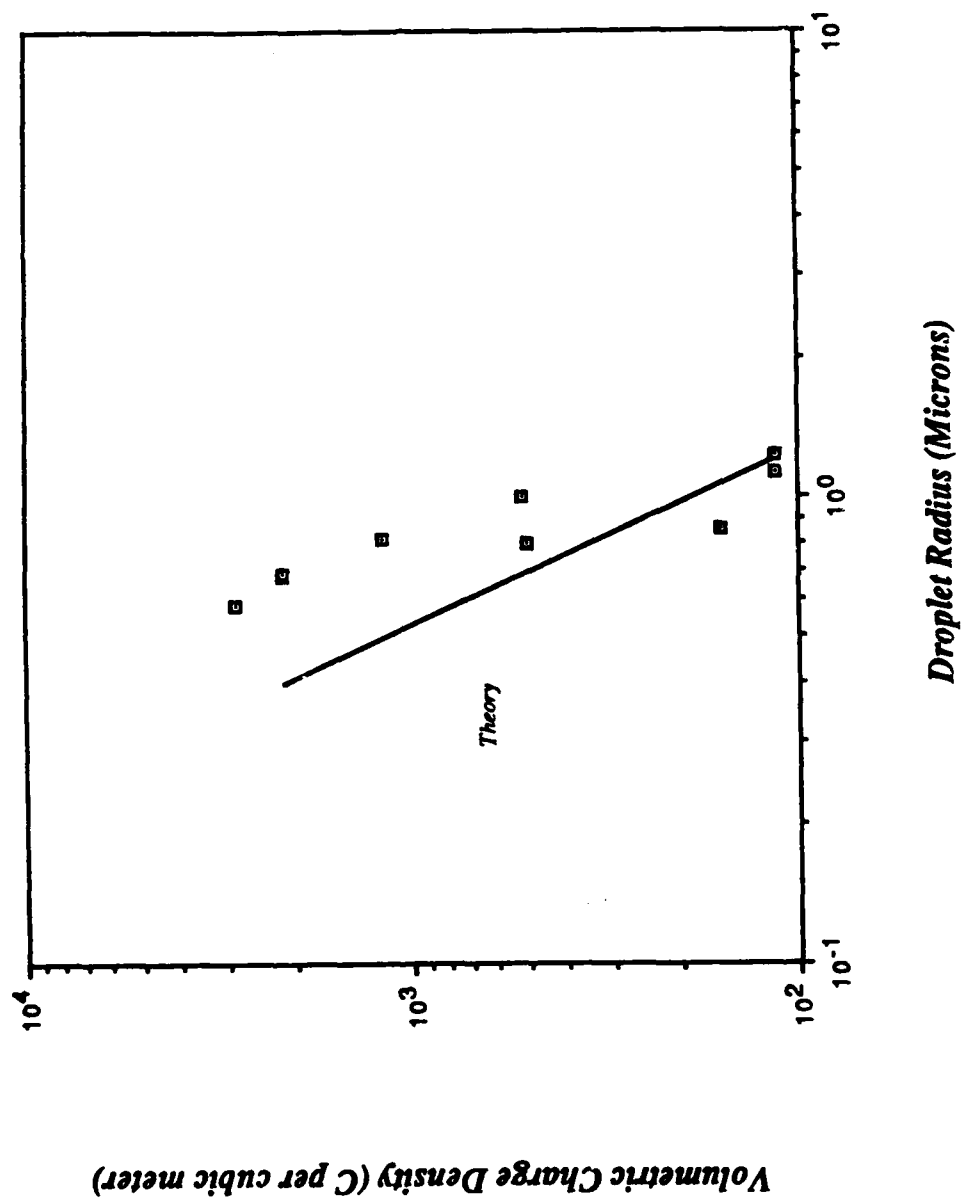


Figure 4.7 Branch B Charging Characteristic

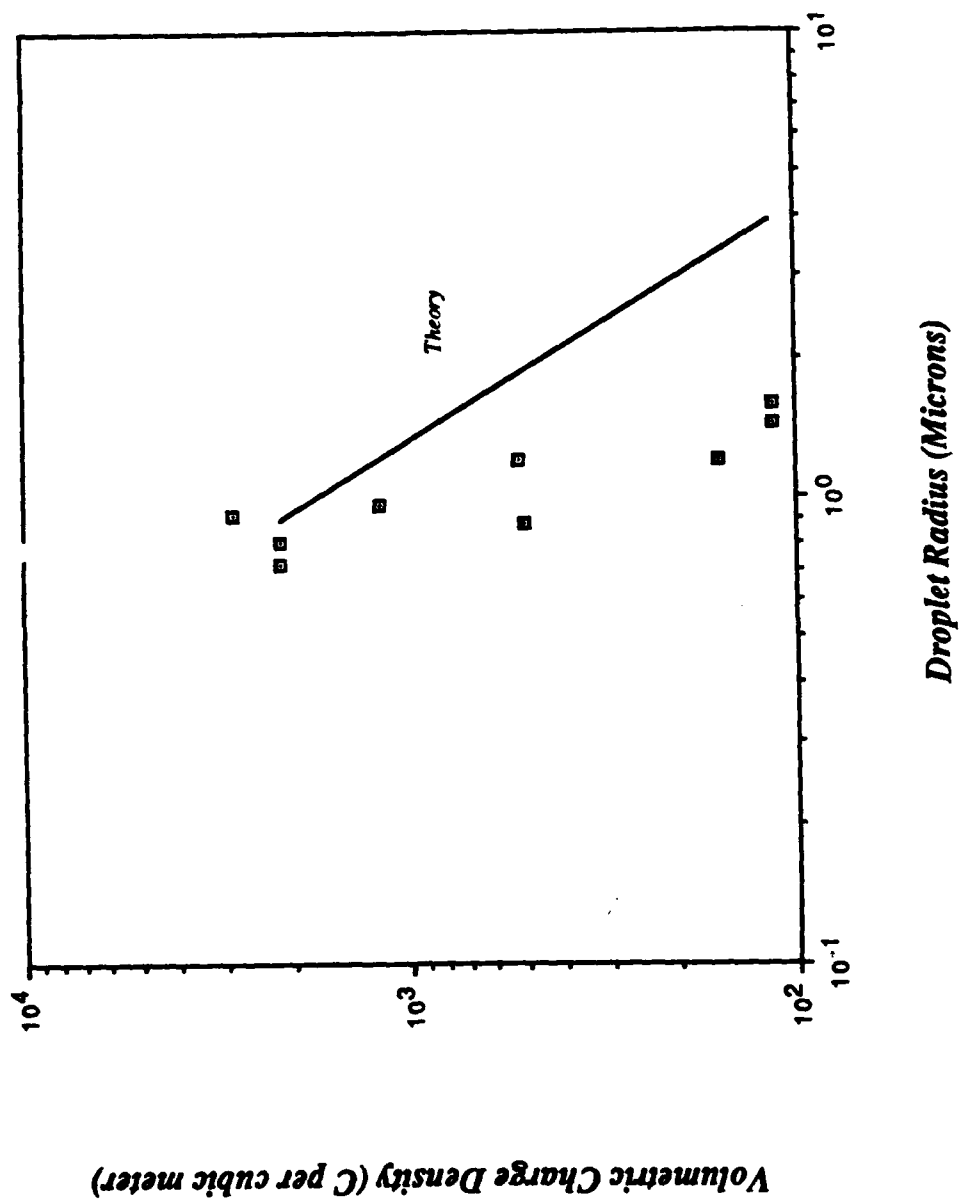


Figure 4.8 Corrected Branch A Charging Characteristic

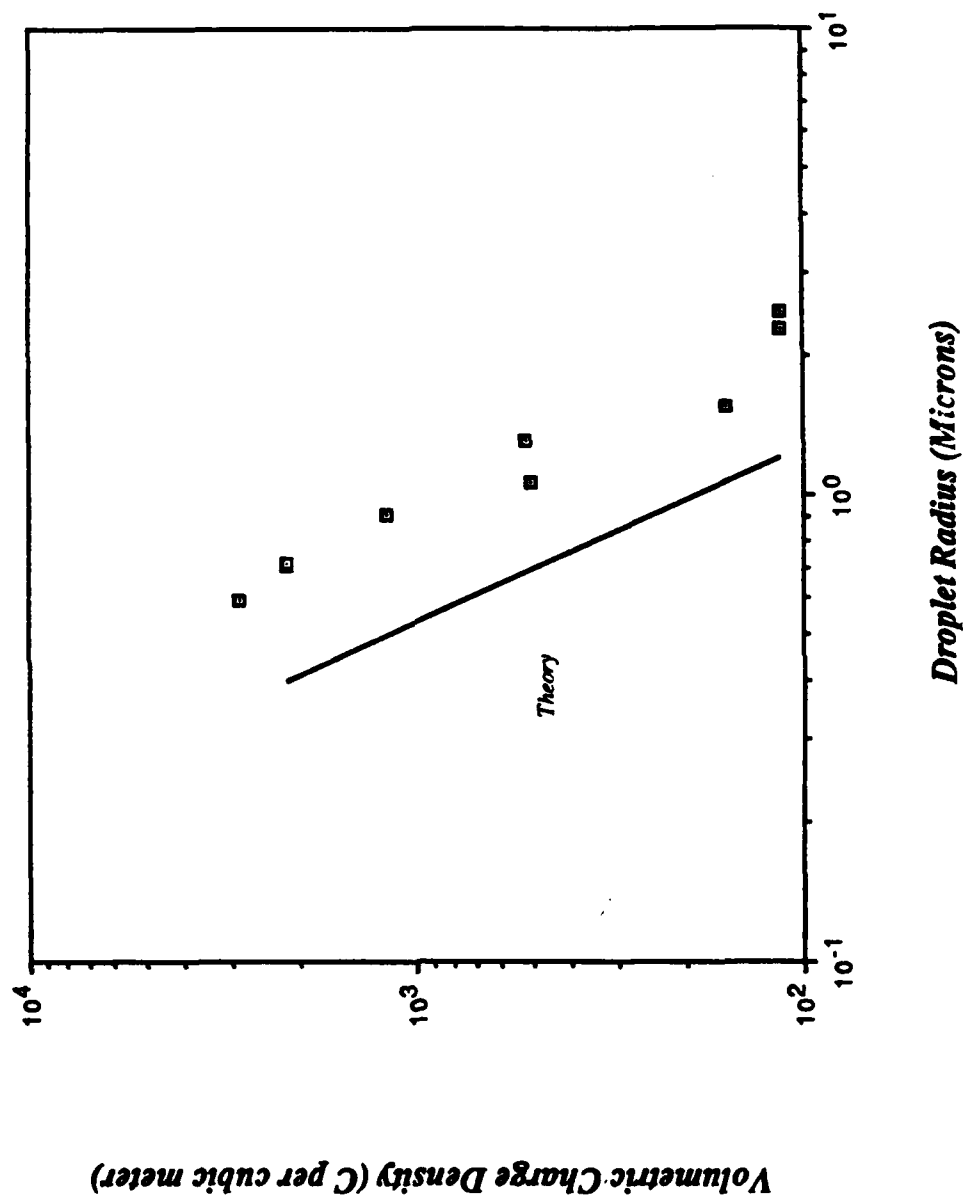
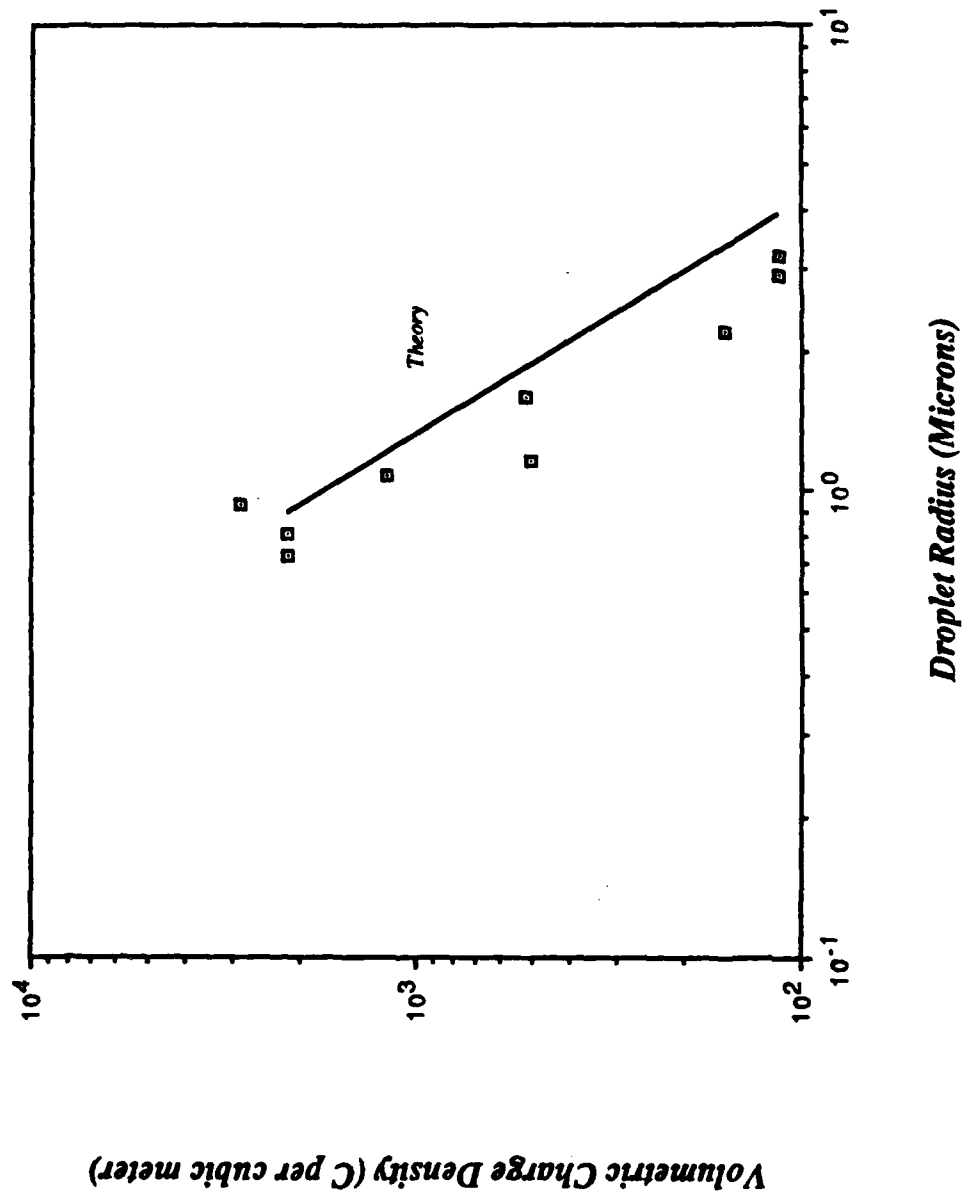


Figure 4.9 Corrected Branch B Charging Characteristic



particular, a difference in dielectric constant would account for the observed change in the value of E_g .

Since the size distributions have been resolved into two separate distributions, it is now possible to estimate the Lagrange multipliers for each of these individual distributions. This provides a check to the values evaluated from the averaged data in the earlier section. Using the two charging characteristics and equation (2.2), a regression analysis routine allows us to deduce α' and β' for branch A and branch B.

<u>Branch</u>	<u>α'</u>	<u>β'</u>	<u>$-\alpha'/\beta'$ (eV)</u>
A	-9.75×10^{-5}	1.75×10^{13}	34.8
B	-4.29×10^{-5}	4.92×10^{12}	54.4

The ratio α'/β' for the B Branch is very close to the value 53.7 eV determined from the averaged data point in Section 4.3. The reason for this is a result of the dominant population of the B branch droplets compared to the A branch.

4.7 Regression Coefficients

The size distribution equation is given by equation (4.4). However, for the purpose of regression analysis, the coefficients are lumped into a single number for ease of analysis. The mathematical form of the model used in the computer analysis is then given by,

$$N = \sum_A^C N_d = \sum_A^C \exp \{ Z_2^{\wedge 2} r + Z_3^{\wedge 3} r + Z_5^{\wedge 5} r \} \quad (4.5)$$

where the Z's are the lumped coefficients. The regression routine then determines the values of these coefficients that provide the best fit of the model to the data. Knowing the values of these

coefficients, it is therefore possible to determine some parameters still unknown in the model, for example the δ' Lagrange multiplier. Comparing equation (4.5) and equation (4.4), we can show that the Z coefficients have the following forms,

$$Z_2 = \beta' \left(\frac{\gamma q}{\epsilon_0 E_s} \right) \quad (4.6)$$

$$Z_3 = \left(\frac{4}{3} \right) \left(\frac{\rho \gamma q}{\epsilon_0^2 E_s^3} \right) \left[\left(\frac{\alpha'}{q} \right) \left(\frac{Q}{M} \right) + \delta' \right] \quad (4.7)$$

$$Z_5 = \left(\frac{32}{9} \right) \beta' \left(\frac{\gamma^3 \rho^2 q}{\epsilon_0^5 E_s^7} \right) \left(\frac{Q}{M} \right) \quad (4.8)$$

Knowing the values of the Z coefficients and equation (4.6), (4.7) and (4.8), all three Lagrange multipliers and the value of E_s can be calculated. Since we are able to determine two of the Lagrange multipliers from the charging equation, this evaluation should provide a check on the accuracy of the multipliers and the consistency of the model equations. The value of the third Lagrange multiplier δ' in the Kelly model is evaluated for the first time using the present data. Through manipulation of the equations, values for E_s can be deduced independently. At the present stage of the theory, there are no analytical forms for these Lagrange multipliers. Therefore, their numerical values on the different branches are valuable to the further understanding of the model.

Taking the ratio Z_2 to Z_5 , the following expression for E_s may be obtained,

$$E_s^6 = \left(\frac{Z_2}{Z_5} \right) \left(\frac{32}{9} \right) \left(\frac{\gamma^2 \rho^2}{\epsilon_0^4} \right) \left(\frac{Q}{M} \right)^2 \quad (4.9)$$

This quantity should be a constant. However, calculation from equation (4.9) indicated that its value is distinctively larger for the B branch. This is consistent with the result of the previous

section where we could only find close correlation with the model if the E_s is larger on the B branch. As pointed out in the previous section a different surface condition such as a difference in dielectric constant could possibly change the value of E_s . Thus, the calculated value for E_s might be viewed as an "effective" limiting surface electron field emission field strength.

Knowing the value of E_s , it is then possible to deduce the value of β' from either equation (4.6) or (4.8). Equation (4.8) is chosen in this study. For each size distribution, two values of β' can be evaluated corresponding to the two branches of droplets. Figure 4.10 shows that there is considerable scatter in the A branch values while the B branch increases steadily. Since β' has dimensions of inverse energy, increasing values of β' on the B branch indicates a decrease in "characteristic energy" of the spray. The precise implication of this energy decrease can only be studied when an analytic form for β' is available.

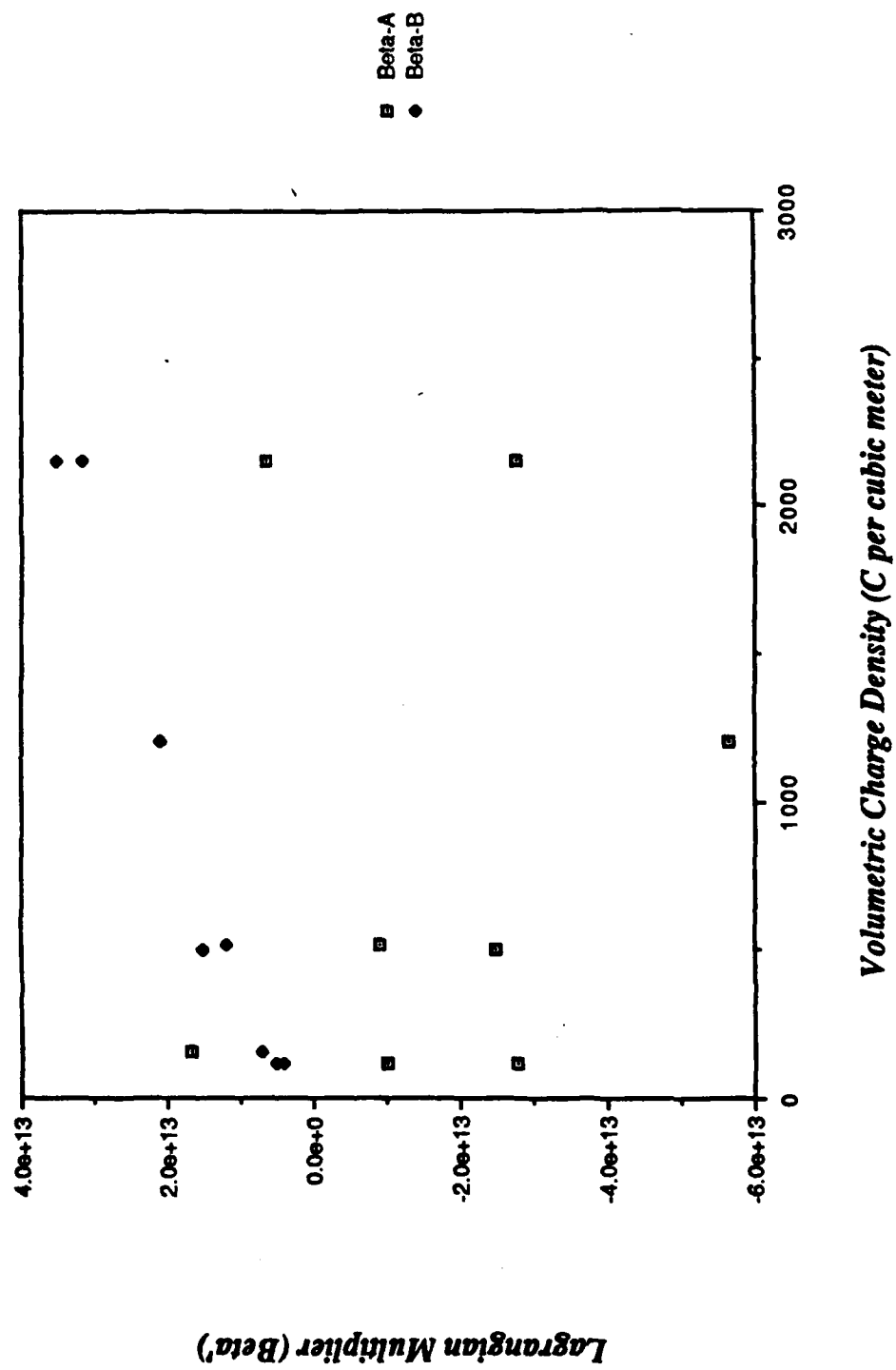
Equation (4.7) is a coupled equation for α' and δ' . Therefore it is not possible to deduce individual values of α' and δ' for each charge-to-mass ratio. However, a single value for α' and δ' could be deduced statistically from the behavior of Z_3 . α' is found to have a value of 2.97×10^{-4} for branch A and -4.46×10^{-4} for branch B. These values are three to five times larger than the previously established value of -0.82×10^{-4} . The value for δ' is however quite constant for both branches having the values 5.02×10^{14} for branch A and 3.47×10^{14} for branch B.

The results of this section draw us to the following conclusion: In the Kelly model it is assumed that an electrostatic spray can be considered an isolated system in thermodynamic equilibrium. From which a state of maximum entropy must be attained. The soundness of this assumption has been ascertained from the various analysis performed on the model against measured data. The model equations have showed consistency and good correlation with the Octoil data. The maximum entropy formalism is therefore a valid approach to electrostatic spray modelling.

4.8 Correction Term For Finite Electrical Conductivity

Examination of Hendrick's and the present data set showed discrepancies that are dependent on

Figure 4.10 Variation of Lagrangian Multiplier Beta'



the charge-to-mass ratio. The deviation between the two is particularly prominent at low values of the charge-to-mass ratios. Experimentally, the two experiments differ primarily in their charge detection devices. In Hendrick's case, an open Faraday cage is used. Charge on the detected droplet are inferred from a cathode follower's induced voltage while in the present experiment, an electrometer is used. In this case, charge is measured directly when they are transferred to the electrometer. This poses no problem when the electrical conductivity of the Octoil droplet is high however it is not the case for low charge-to-mass ratio droplets because the electrical conductivity of the Octoil is largely responsible by the presence of free electrons. When conductivity becomes very small at small values of charge-to-mass ratios, the charge transfer process is slowed down. Because the electrometer allows only a specific time for charge transfer, errors are introduced if the charge relaxation time is comparable to the charge transfer time.

A correction factor is introduced in this section to account for the finite charge relaxation time in Octoil. The amount of correction is charge-to-mass ratio dependent and is negligible at high charge-to-mass ratios. This is consistent with the fact that the observed deviation from Hendrick's data is only seen at small values of charge-to-mass ratios. In this respect, it is assumed that Hendrick's setup is not affected by the finite electrical conductivity because the measurement is inductive rather than direct.

Consider a charged droplet having a total charge Q_0 and electrical conductivity σ . Upon contact with the stopping copper plate, charges will begin transferring to the electrometer. The amount of free charge remains after time, t , is given by the expression,

$$Q(t) = Q_0 e^{-\sigma t / \epsilon} \quad (4.10)$$

where ϵ is the permittivity of the media. Since most dielectric fluids have a dielectric constant of about two, we will approximate ϵ by $2\epsilon_0$ where ϵ_0 is the permittivity of free space.

The conductivity consists of two components; one due to the residual conductivity σ_0 , the other due to the presence of excess charge carriers given by $\mu_0 \rho_e$ which is the product of the

mobility and charge density of the electrons in the media. The conductivity is then expressed as,

$$\sigma = \sigma_0 + \mu_0 \rho_e \quad (4.11)$$

For hydrocarbons, the values of σ_0 are usually very small, typically of the order 10^{-13} mho/m. The mobility of electron in Octoil is approximately 10^{-8} mho/C. In this experiment, typical charge densities for the droplets are between 10 and 10^5 C/m³. Thus, we may approximate equation (4.11) by,

$$\sigma \approx \mu_0 \rho_e \quad (4.12)$$

The fractional charge lost after time, t , can be written as,

$$f = (1 - e^{-t/\tau}) \quad (4.13)$$

where $\tau = \epsilon / \sigma$, is the time constant for charge relaxation. If t_0 is the time allowed for charge transfer, the fractional charge lost in time t_0 is given by,

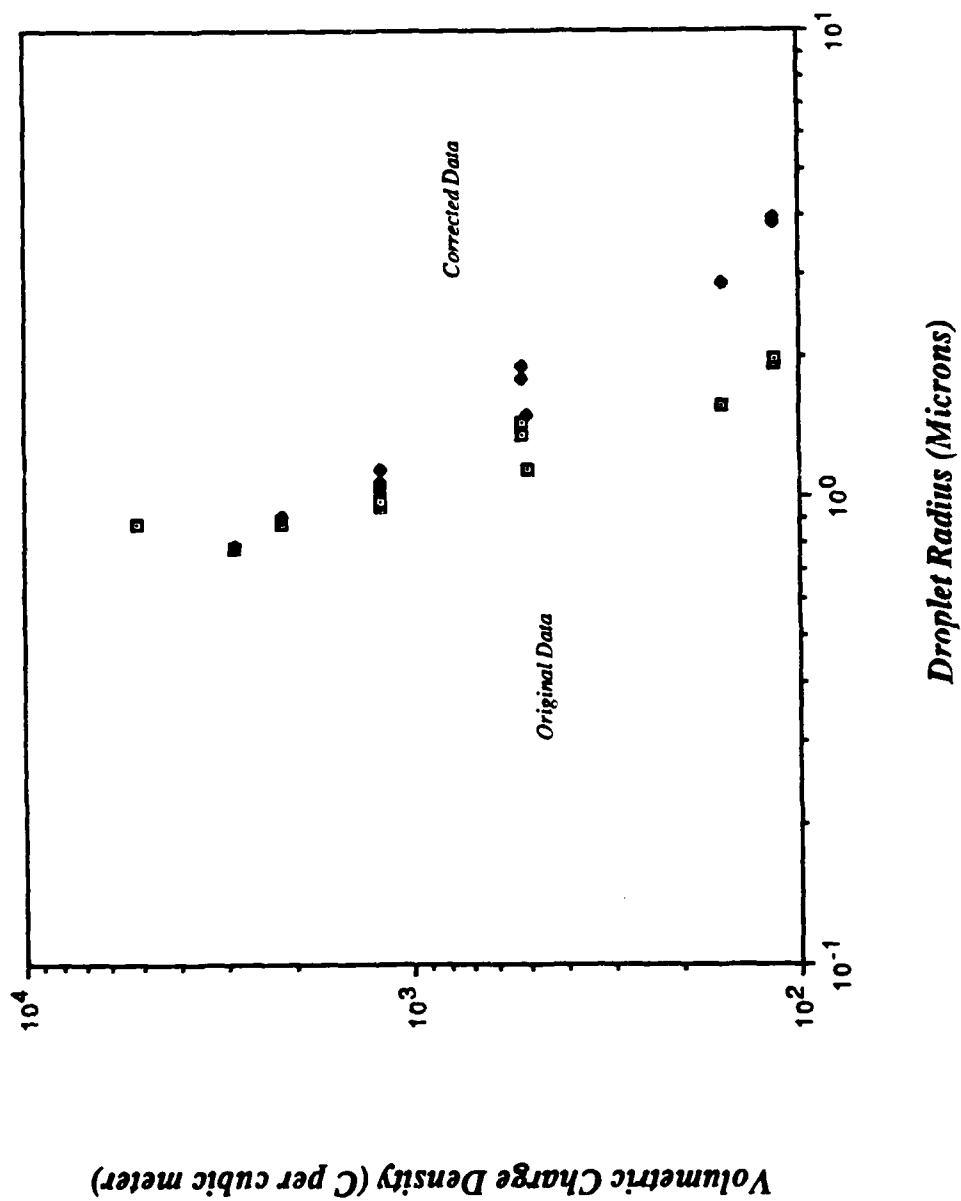
$$f_t = (1 - e^{-t_0/\tau}) \quad (4.14)$$

the actual size of the droplet, r_a can then be calculated from the measured radius, r_m , using the relationship⁴⁹,

$$r_a = (f_t)^{-1/3} r_m \quad (4.15)$$

The correction factor $(f_t)^{-1/3}$ is a function of the volumetric charge density (and therefore a function of the charge-to-mass ratio) of the droplets. Figure 4.11 shows the correction to the

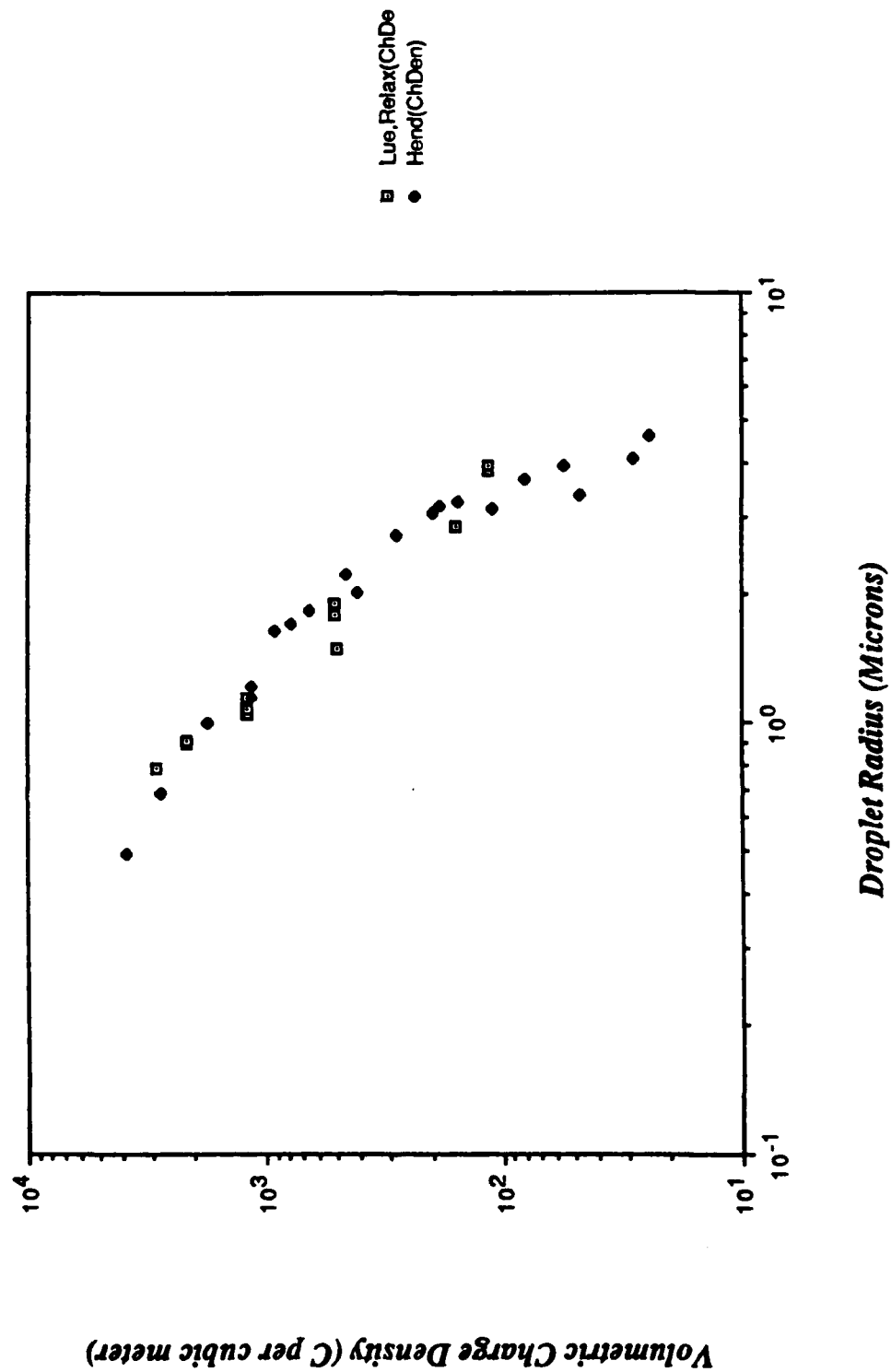
Figure 4.1.1 Effect of Finite Conductivity on Octoil



measured radius due to charge relaxation. The correction is negligible at charge densities higher than 10^3 C/m^3 .

These corrected data showed excellent correlation to Hendrick's data (Figure 4.12). Since the Hendrick's data are not affected by the finite electrical conductivity, they are used as a standard to check the feasibility of the conductivity argument. Figure 4.12 shows that the conductivity assumption offers a plausible explanation for the deviation observed. It would also be worthwhile in future tests to enhance the conductivity through additives. This should eliminate the need for the correction term discussed in this section.

Figure 4.12 Comparison of Corrected Data with Hendrick's



Chapter V

Summary

Theoretical modeling indicates that droplet charging in electrostatic sprays will exhibit phase-transition like behavior. A test facility has been constructed to verify this. A low charge-to-mass ratio quadrupole mass spectrometer/high speed electrometer apparatus is used to determine the droplet size and charge distribution of charged droplet sprays. These data are the first of their kind to be obtained from electrostatic sprays. Comparison with data published by Hendrick's has shown good correlation.

Necessary software has been developed to enable evaluation of various spray models with the data. The maximum entropy model is compared with the Octoil data as an initial test of the facility. Several predictions of the model are confirmed through this analysis. The phase-transition like behavior which manifests itself as a multimodal size distribution is confirmed at low charge-to-mass ratios. Droplets at very large radius are shown to be describable by a universal law (the asymptotic B branch). This branch has the special property of being independent of the fluid properties.

All Lagrange multipliers introduced in the maximum entropy model are now numerically defined through an extension of the model equations.

The effective surface electron emission field strength is found to be larger on the asymptotic B branch compared to the smaller droplets on the A branch. This result can also be independently obtained from comparison of the theoretical and measured charging characteristics of the spray. This probably indicates a difference in surface condition for the two spray branches.

Charge relaxation due to finite electrical conductivity of Octoil at low charge densities was found to cause underestimation of the droplet size. A correction factor is derived and the corrected data show very good agreement with the previous data and the model.

Bibliography

1. C.D.Hendricks Jr., Charged droplet experiments, Journal of Colloid Science, 17, 1962.
2. A.J.Kelly, Electrostatic metallic spray theory, J. Appl. Phys. 47(12), Dec 76.
3. A.J.Kelly, Electrostatic spray theory, J. Appl. Phys. 49(5), May 78.
4. A. G. Bailey, The Theory and Practice of Electrostatic Spray, Atomization and Spray Technology 2(1986) 95 - 134.
5. Zeleny. J, On the conditions of instabilities of electricified drops with applications to the electrical discharge from points, Proc. Cambridge Phil. Soc., 18, 71 (1915).
6. Zeleny. J, Stability of electrified surfaces, Phys. Rev. 10, 1917.
7. Drozin, V.D, The electrical dispersion of liquid aerosols, J. Colloid Sci., 10, 158 (1955).
8. J.M.Schneider, N.R.Lindblad, C.D.Hendricks' Jr and J.M.Crowley, Stability of an electrified liquid jet, J. Appl. Phys., 38, 6, 2599, 1967.
9. C.D.Hendricks, Jr., Charged droplet experiments, Journal of Colloid Science 17, 249-259 (1962).
10. W.A.Macky, Some investigation on the deformation and breaking of water drops in strong electric fields, Proc. Roy. Soc., A, Vol. 133, 1931.
11. Lord Rayleigh, Phil. Mag. 14, 184, 1882.
12. G.I.Taylor, Disintegration of water droplets in an electric field, Proc. Roy. A, Vol 280.
13. C.T.R.Wilson and G.I.Taylor, the bursting of soap bubbles in a uniform electric field, Phil. Soc. Proc. Vol.XXII.
14. A.Neukermans, Stability criteria of an electricified liquid jet, J. Appl. Phys., Vol.44, No. 10, 1973.
15. J.R.Melcher, Field-Coupled Surface Waves - a comparative study of surface-coupled electrohydrodynamic and magnetohydrodynamic systems, MIT Press, 1963.
16. B.Vonnegut and R.L.Neubauer, Production of monodisperse liquid particles by electrical atomization, 1952, SQ700.045.v7.
17. R.J.Pfeifer and C.D.Hendricks's Jr, Parameter studies of electrohydrodynamic spraying, AIAA Journal, Vol. 16, No. 3, 1968.
18. V.E.Krohn, Electrohydrodynamic capillary source of ions and charged droplets, J. Appl. Phys., Vol. 45, No. 3, Mar 1974.
19. V.E.Krohn, Glycerol droplets for electrostatic propulsion, Am. Rocket Soc., Electric Propulsion Conf., Mar 62, 8937-6006-RU-000.
20. J.J.Hogan and C.D.Hendricks', Investigation of the charge to mass ratio of electrically

sprayed liquid particles, AIAA Journal, Vol. 3, Feb 1965.

21. R.W.Sellen and T.A.Brzustowski, A prediction of the drop size distribution in a spray from first principle, Atomization and Spray Technology 1 (1985) 84-102.
22. Davidson, Statistical Mechanics, McGraw Hill.
23. H.C.Simmons and A.J.Kelly, Electrostatic spraying of oil-based agricultural products, Pesticide Formulation and Application Systems: Fifth Volume. ASTM STP915, L.D.Spicer and T.M.Kaneko, Eds., American Society for Testing and Materials, 1986.
24. Amptek Specification Sheet (to be checked).
25. SAS Institute Basic User Manuel.
26. SAS Institute Economic Time Series (ETS) User Manuel.
27. K-M.Lue, Electric Propulsion Lab Monthly Progress (Mar 87).
28. Chatterjee and Price, Regression Analysis by Examples, John Wiley.
29. K-M.Lue, Electric Propulsion Lab Monthly Progress (Apr 87).
30. A.J.Kelly, Low charge density electrostatic atomization, IEEE Transactions on Industry Applications, Vol. 1A-20, No. 2, Mar-Apr 1984, p267.
31. A.J.Kelly, Pattern Number 4294105.
32. K-M Lue, Electric Propulsion Lab, Monthly Progress Report, (Jan 87).
33. W. Paul and M. Raether, Das Elecktrische Massenfilter, Zeitschrift Physik, Bd. 140, S262 - 273 (1955).
34. C.T.Norgren, D.S.Goldin, D.J.Connely, Colloid Thruster Beam Analysis: Design and operation of a suitable quadrupole mass filter, NASA TND-3086, Oct 1965.
35. M.Moshrrafa and H.J.Oskam, Design and Construction of a Mass Spectrometer for the Study of Basic Process in Plasma Physics, Jul 1961, NP-11459.
36. P.H.Dawson and N.R.Whetten, Mass spectroscopy using RF Quadrupole Fields, Adv. in Electronics and Electron Physics, Vol, 1969.
37. W.M.Brubaker and J.Tuul, Performance Studies of a Quadrupole Mass Filter, The Review of Scientific Instruments, Vol 35, No 8, Aug 1964.
38. A.R.Fairbairn, A Simple Quadrupole Mass Spectrometer, Sep 68, Rev. Sci. Instrm.
39. A.E.Holm, W.J.Thatcher and J.H.Leck, An Investigation of the Factors Determing Maximum Resolution in a Quadrupole Mass Spectrometer. J. of Physics E. Scientific Instruments 1972, Vol 5.
40. R.F.Lever, Computation of Ion Trajectories in the Monopole Mass Spectrometer by Numerical Integration of Mathieu's Equation, IBM Journal Jan 66.
41. N.W.McLachlan, Theory and applications of Mathieu's Function, Oxford University Press, 1951.
42. W.M.Brubaker, The Quadrupole Mass Filter, Instruments and measurements(I),

82009.493.05.

43. W.M.Brubaker and W.S.Chamberlin, Theoretical and Experimental Comparisons of Quadrupole Mass Analyzers with Round and Hyperbolic Field Forming Surfaces, Recent Developments in Mass Spectroscopy.
44. K.Maeda, M.Sakimura and A.Fukuda, Resolution of Mass Filter, Recent developments in mass spectroscopy.
45. K.Maeda, M.Sakimura and A.Fukuda, A General Expression of Ion Motion in Quadrupole Field, Recent developments in mass spectroscopy.
46. T.Kondo, S.Taya, I.Omura, Simulation of Ion Trajectory in a Quadrupole Mass Filter, Recent developments in mass spectroscopy.
47. Ulf Von Zahn, Monopole Spectrometer - A New Electric Field Mass Spectrometer, The Review of Scientific Instruments, Vol 34, No 1, Jan 63.
48. Moore, Applications of Electrostatics, John Wiley.
49. K-M Lue, Electric Propulsion Lab, Monthly Progress Report, Jun 87.
50. K-M Lue, A.J.Kelly, Quadrupole Mass Spectrometer Measurements of Electrostatic Sprays, IAP Electrostatic 87 Conference, Oxford, England.

Appendix A: Minimum Energy Model

The minimum energy model proposed by Vonnegut and Neubauer¹⁶ considers a volume of liquid V and total charge Q undergoing breakup. The final state of the breakup process is a group of smaller droplets of equal size each containing equal amount of charge q . The final droplet radius and the total number of droplets in the end state are then determined from the condition of minimum energy, i.e., the final state must have equal or less energy than the initial state.

The minimum energy condition then requires the setting of the derivative of the combined surface energy and electrostatic potential energy with respect to radius to zero. From this condition, an expression for the final radius of the droplet can be obtained.

The condition of equal final droplet size and charge makes the derivation very restrictive. In fact, the theory applies only to monodisperse sprays. In Hogen's paper, the derivation is carried further to give the charge-to-mass ratio as a function of radius,

$$\frac{Q}{M} = \frac{\sqrt{27\epsilon_0\gamma}}{\rho r^{3/2}} \quad (A.1)$$

where ϵ_0 is the permittivity of free space, γ is the surface tension of the fluid and ρ is the density of the fluid.

Equation (A.1) shows that the charge-to-mass ratio scales inversely as the three-half power of the radius. This describes Octoil and glycerine spray data fairly well. However, the correlation with data for Wood's metal is not very good.

Observations of electrostatic sprays¹, have indicated that the droplets produced are far from uniform in size. Furthermore, the charge-to-mass ratios of the droplets are not always equal as assumed by Vonnegut. The conditions for the monodisperse spraying are highly sensitive to flow rate, charging voltage, and fluid properties. Therefore, the validity of the model will depend on

these controlling factors. Failure of the model to describe Hendrick's data could be a violation of these basic assumptions of the model.

Appendix B: Electrohydrodynamic Model

Physical insight is the motivation for this model. It's been observed that a charged liquid meniscus forms Taylor cones^{12,13} when acted upon by an electric field. At the apex of these cones, liquid is drawn out into filaments due to electric field concentration. These electrified liquid filaments are unstable to perturbations; thus they are prone to develop instabilities where they eventually breakup into droplets.

Based on the work of Melcher¹⁵ on field-coupled surface waves, Schneider⁸ developed a model, which was later improved by Neukermans¹⁴. The model relates the charge-to-mass ratio of a droplet to the charging voltage on the fluid meniscus and the geometry of the charging electrode. The expression for charge-to-mass ratio is given by,

$$\frac{Q}{M} = \frac{2\epsilon_0 V_a}{a^2 \eta \ln\left(\frac{b}{a}\right)} \quad (B.1)$$

where a is the radius of the liquid jet before instability sets in, b is the radius of the cylindrical charging electrode, η is the density of the fluid and V_a is the charging voltage with respect to ground.

The radius of the droplet after breakup can be expressed as $r_d = (3a^2 v_j / 4f)^{1/3}$, where f is the frequency of breakup and v_j is the velocity of the liquid jet. In this case, the charge-to-mass ratio is not strictly a pure function of the radius of the droplet but is a function of the charging voltage, and jet velocity as well.

In this formulation, the Rayleigh limit is not built into the model. One could have droplets exceeding the Rayleigh limit, thus, rendering the model unrealistic. This model, similar to the minimum energy model, does not model the size distribution of the spray.

Studies on the breakup process can only yield expressions for the average charge-to-mass ratio on the basis of some amplified disturbances in the fluid jet. The problem of size distribution

of the electrostatic spray has not been addressed by other authors. To model the size distribution, a different approach must be taken. The approach that has been used is based on the maximum entropy formalism. Kelly² had used this formalism to derive a size distribution for the electrostatic spray. A similar derivation by Swellen and Brzustowski²¹ exists also for droplet size distribution in uncharged sprays. These models are referred to as first principle models because they utilize the basic conservation equations for mass, momentum, energy, and charge.

Appendix C: Operation Principles of the Quadrupole Mass Spectrometer

Designed in 1958 by Paul³³ for fusion fuel separation, the mass spectrometer selects charged droplets of given charge-to-mass ratio from the incoming droplet beam. These droplets follow stable trajectories through the spectrometer and are then picked up by a charge detection assembly situated at the quadrupole exit. Droplets with the incorrect charge-to-mass ratio will not be focused and their trajectories will diverge, eventually colliding with the quadrupole rods.

The quadrupole does not operate with a magnetic field, therefore it is lighter in weight. The attractive features of the device consist of variable resolution at all charge-to-mass ratios, low power consumption and high sensitivity. Such devices can easily scan charge-to-mass ratios over several orders of magnitude. The instrument developed for this electrostatic spray experiment has a four order of magnitude range from 0.01 to 10 C/kg.

A schematic of the mass spectrometer is shown in Figure 3.1. It consists of four stainless steel rods each 1.43 meter long mounted in a square array. The original device conceived by Paul requires the use of hyperbolic electrode surfaces. However, the manufacturing of such surfaces are far more difficult than circular ones. The best approximate field achievable is obtained when circular rods of radius 16% smaller than the field radius^{34,35,36} is used. Studies shown that devices with these specifications can provide pole fields that are accurate to within a percent of the field generated by hyperbolic rods^{37,43}.

To operate the quadrupole, potentials ϕ_1 and ϕ_2 are applied to the rods in diagonal pairs where,

$$\phi_1 = U + V \cos \omega t \quad (C.1)$$

$$\phi_2 = -(U + V \cos \omega t) \quad (C.2)$$

The ϕ 's represent two d.c. biased oscillating voltage signals. Each of the a.c. components are 180 degrees out of phase from each other and they are d.c. biased in the opposite

direction by equal magnitudes.

Given these potentials, a time varying potential is set up in the region surrounded by the rods. The potential in this field has the form,

$$\Phi = (U + V\cos\omega t) \frac{(x^2 - y^2)}{r^2} \quad (C.3)$$

Charged droplets entering this time varying field will be set into oscillatory motions, but only those with bounded oscillations will exit the filter at the detector.

The governing equations for the quadrupole do not take drag due to air friction into account. Thus, it is necessary to operate the quadrupole under vacuum. Gravitational force is found to be small compared to the electrostatic forces experienced by the charged droplets and can be neglected.

To derive the equations of motion for a charged droplet in a quadrupole field, we take the gradient of the potential to obtain the time varying electric field. Assuming a droplet of mass m and charge Q , the equations of motion can be expressed as:

$$mX_{tt} + 2Q(U + V\cos\omega t) \frac{X}{r^2} = 0 \quad (C.4)$$

$$mY_{tt} - 2Q(U + V\cos\omega t) \frac{Y}{r^2} = 0 \quad (C.5)$$

$$mZ_{tt} = 0 \quad (C.6)$$

Equation (C.6) indicates that motion in the axial direction is not affected by the applied field. Equations (C.4) and (C.5) are not in standard canonical form. Transforming the equations with

the introduction of a dimensionless time variable ξ such that $\omega t = 2\xi$, we obtain the equations,

$$X_{\xi\xi} + (a + 2q \cos 2\xi) = 0 \quad (\text{C. 6})$$

$$Y_{\xi\xi} - (a + 2q \cos 2\xi) = 0 \quad (\text{C. 7})$$

where a and q can be expressed as,

$$a = \frac{8QV}{m(r\omega)^2} \quad (\text{C. 8})$$

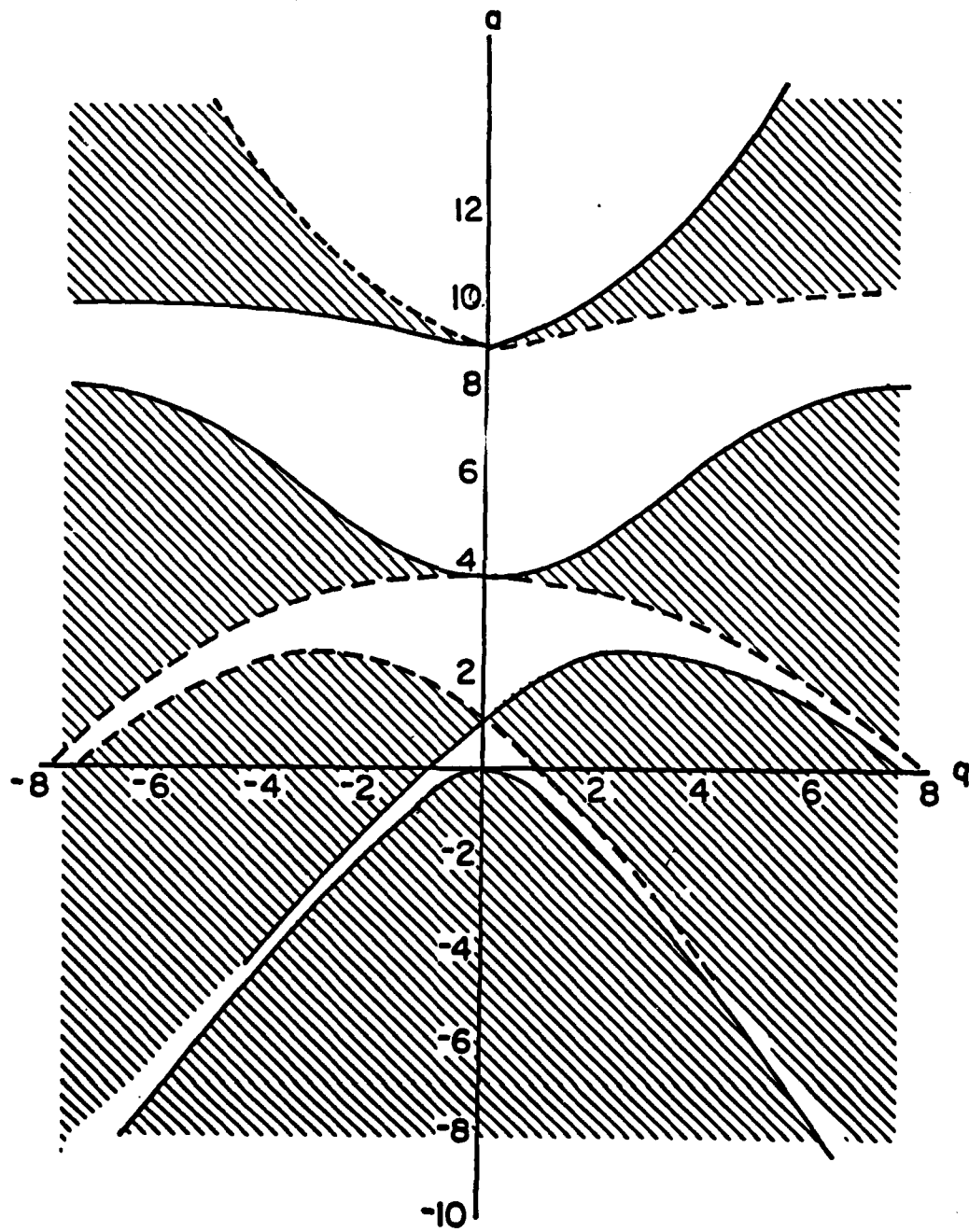
$$q = \frac{4QV}{m(r\omega)^2} \quad (\text{C. 9})$$

In these forms, they are the well known Mathieu's Equations, the solution of which, known as the Mathieu's Function, describes the trajectories of the charged droplets in the quadrupole field. Mathieu's Equations are linear differential equations with periodic coefficients⁴¹. They exhibit bounded stable solutions only for limited values of a and q ^{41,34,35,36} (Note: Stable solution in this case refers to bounded solution, there is no requirement that the solutions be periodic).

Figure C.1 shows the stability region in the a - q space. The clear regions denote the values of a and q in which stable solutions exist, whereas the cross-hatched regions correspond to the values of a and q for unstable solutions. In the quadrupole mass spectrometer, there are two pairs of rods independently connected to different signal sources. This gives two equations of motion (equation C.4 and C.5) for a single charged droplet entering the quadrupole. The motion along the axis of the quadrupole is not influenced by the applied electric field. Equation C.6 indicates that the charged droplet will retain its velocity when it is injected into the quadrupole.

Equation C.6 and C.7 have coefficients that are different in signs causing their stability

Figure C.1 Stability Diagram of Mathieu Equation



regions in the a - q space to be different. For a charged droplet to successfully pass through the quadrupole both solutions to the Mathieu's Equations must be bounded. The stability diagram for the quadrupole therefore consists of the superposition of the two individual stability curves. The intersection of the stable regions are then the stable regions governing the operation of the quadrupole mass spectrometer.

To operate the quadrupole, a point in one of these stable regions of the a - q diagram is chosen as the operating point. From either expression (C.8) or (C.9), the parameter a or q can be related to the charge-to-mass ratio of the droplet and other quantities such as the frequency of the a.c. signal and amplitude of the applied potential. The region closest to the axis is chosen for this device. It is also a common practice among designers of quadrupole devices. Other "higher" stable regions on the stability map could be used, but require higher operating voltages on the quadrupole rods and are usually not practical³⁶.

Figure C.2 shows an enlarged view of the first stable region for the quadrupole. Having chosen the operating point (a, q) , U can be calculated if V is prescribed or vice versa. Dividing equation C.8 by C.9 we obtain, $a / q = 2U/V$. It should be noted that once these voltages are chosen, they do not depend on other parameters of the quadrupole. From the chosen value of a or q , the scanning charge-to-mass ratio can be calculated from equation C.8 or C.9 as a , q and the field radius r are fixed. The charge-to-mass ratio is therefore a function of the applied frequency of the A.C. voltage.

It is possible to operate the quadrupole in two different modes. One of them, described in the previous paragraph requires fixing the quadrupole rod voltage and allowing the variation of the charge-to-mass ratio by changing the A.C. frequency. The alternate operating mode corresponds to fixing the applied quadrupole A.C. frequency while the scanning charge-to-mass ratio is changed by varying the amplitude of the applied potentials. Both modes are equivalent but the actual implementation depends on the capability of the power source available. In the present design, the first mode is used.

Resolution of the instrument is defined as the ratio of the scanning charge-to-mass ratio to

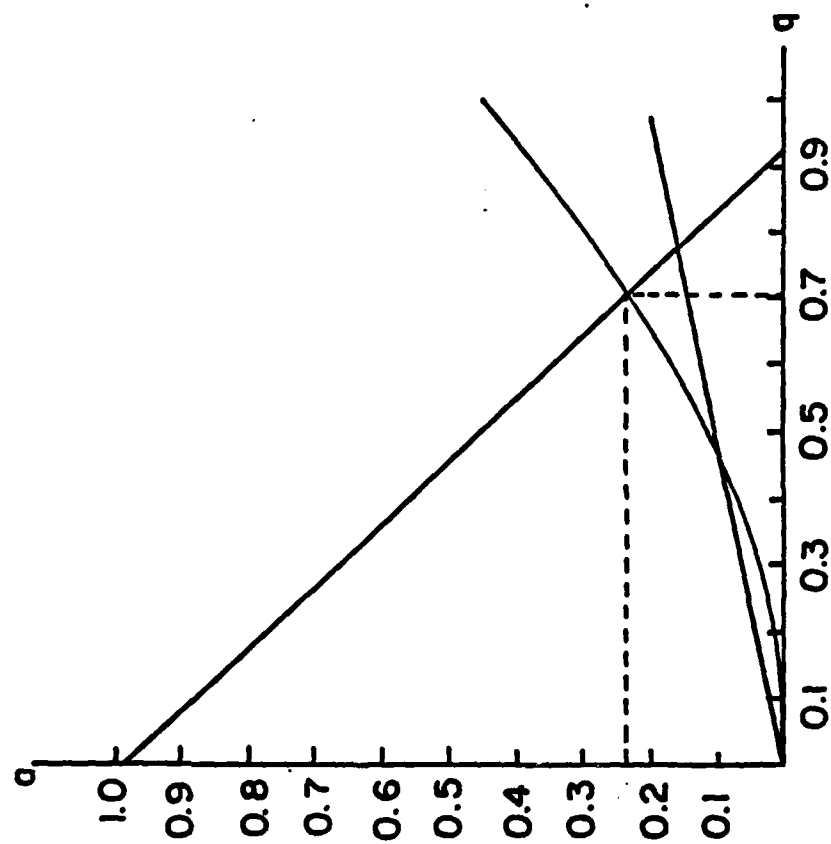


Figure C.2 First Stable Region

its bandwidth at that ratio. In principle, one would like to have infinite resolution. In Figure C.2, the apex of the stability region corresponds to the point of infinite resolution. Operations of the quadrupole at this point would permit no droplet to pass through. Drawing a line from the origin to the chosen operating point, we obtain the mass line. Once the operating point (a, q) is defined, droplets of different charge-to-mass ratio would correspond to different locations on the mass line. On this line the charge-to-mass ratio increases as one moves away from the origin.

Notice that only a small portion of this line is within the stable region. Droplets with charge-to-mass ratios corresponding to the stable portion of the mass line would be selected (Figure C.2). Therefore, the narrower the stable portion of the mass line, the higher the resolution of the quadrupole. In practice, one would like to operate very close to the apex to achieve a high resolution. On the other hand, one should also consider the fact that the higher the resolution, the more restrictive the droplet selection process. It will reduce the quadrupole transmission efficiency (i.e. the amount of droplets to be collected will be reduced). To have a reasonable capture rate of the droplets the resolution should not be too high. The operating point chosen for this device in the a - q plane is (0.223, 0.69). This corresponds to a scanning resolution of 20, which means that if the scanning charge-to-mass ratio is 10 C/kg, droplets with charge-to-mass ratio between 9.5 to 10.5 C/kg will be selected.

To ensure that a specified resolution is attained, the motion of the droplets along the quadrupole axis must be considered. Although the applied fields do not affect the droplets axial motion, their axial velocities are retained and govern the resident time of the droplets in the field. The resident time of the droplets determines the effectiveness of the quadrupole as a filtering device because the quadrupole removes unwanted droplets by causing their trajectories to diverge and these diverging trajectories require finite time to develop.

Therefore, the higher the resolution, the more selective the filtering process and requires the droplets to perform more oscillations for a finer selecting process. Unfortunately, there is no straight forward rule for determining the number of oscillations required. A general rule for the required number of particle oscillations can be obtained from related ion beam research³⁴. It is

entirely empirical and should be use with caution. The number of oscillations, N , a droplet needs to perform during its passage through the quadrupole is expressed in terms of the resolution R where,

$$N \approx (3.5 R)^{1/2} \quad (C.10)$$

For a given resolution, the number of oscillations required for complete removal of unwanted droplets can be determined from equation (C.10). Within the transit time, all droplets must perform at least N oscillations. Insufficient resident time would result in a decrease in effective resolution. Since the extractor electrode is maintained at ground potential, droplets formed will be accelerated by the atomization potential. Assuming that the droplet carries a charge Q and mass M then energy conservation gives,

$$Q V = 0.5 M v^2 \quad (C.11)$$

where V is the charging potential with respect to ground potential and v is the final velocity of the droplet.

The above expression permits the final velocity to be expressed as a function of the charge-to-mass ratio and the atomization potential. The transit time in the quadrupole is then calculated from the length of the quadrupole field. The length of the quadrupole rod is taken to be the length of the field i.e. end effects have been neglected. Multiplying the transit time by the scanning frequency enables us to determine the number of oscillations the droplets perform.

In the preliminary design of the quadrupole, high rod voltages were not possible. As a result, the number of oscillations were insufficient for the designed resolution of 20. Attempts have been made to decelerate the droplets using a deceleration electrode placed at the quadrupole entrance. This method did not work because the velocity of the droplet scales as the square-root of the potential drop. A voltage comparable to the charging potential is required to slow the

droplet sufficiently. The method failed because application of high potential at the deceleration electrode hinders the smooth operation of the atomizer due to their close proximity. This causes frequent arcings across the decelerating electrode which inhibit the smooth operation of the sprayer.

An alternate method was then used to increase the number of oscillations of the droplets during transit through the quadrupole. This is achieved by increasing the scanning frequency of the quadrupole which increases the number of oscillations for the same atomization potential. However, to maintain the same charge-to-mass ratio, higher d.c. and a.c. amplitude must be used in the quadrupole signals. By using transformers to amplify the existing input voltages the operating point can be maintained at higher frequencies (cf. C.8 and C.9). Since these transformers were originally designed to operate at a fixed frequency of 400 Hz, their effective gain changes when other frequencies are applied. The gain on these transformers tend to decrease with increasing operating frequency. As a result, the present quadrupole is only capable of scanning up to 2.9 C/kg.

Quadrupole Power Supply Circuit

The voltage source is a Behlman variable A.C. power supply capable of a maximum RMS value of 270 volts. Calculations show that for our device an A.C. amplitude of approximately 3000 volts is required to maintain a scanning resolution of 20 assuming no deceleration electrode is used. To obtain the high voltages two 1000:1 voltage transformers are used to amplified the quadrupole signals. Figure C.3 is the circuit diagram of the voltage amplifier circuit. The original waveform from the Behlman unit is duplicated; they are made 180° out of phase from the one another and are amplified by the two amplifiers.

The required biased voltage is supplied by a Kepco power supply. In the experiment, it is required to operate the quadrupole at frequencies between 50 to 2000 Hz. Since the gain of the transformers cannot be maintained constant at different frequency and that the transformers have

1. APPROVED BY: [Signature]
 DATE: 10/15/70
 THIS DOCUMENT IS UNCLASSIFIED
 EXCEPT FOR PORTION OF PARAGRAPH 100.12
 EXEMPTION IS GRANTED
 MATTHEW J. KEEFER
 Chief, Technical Information Division

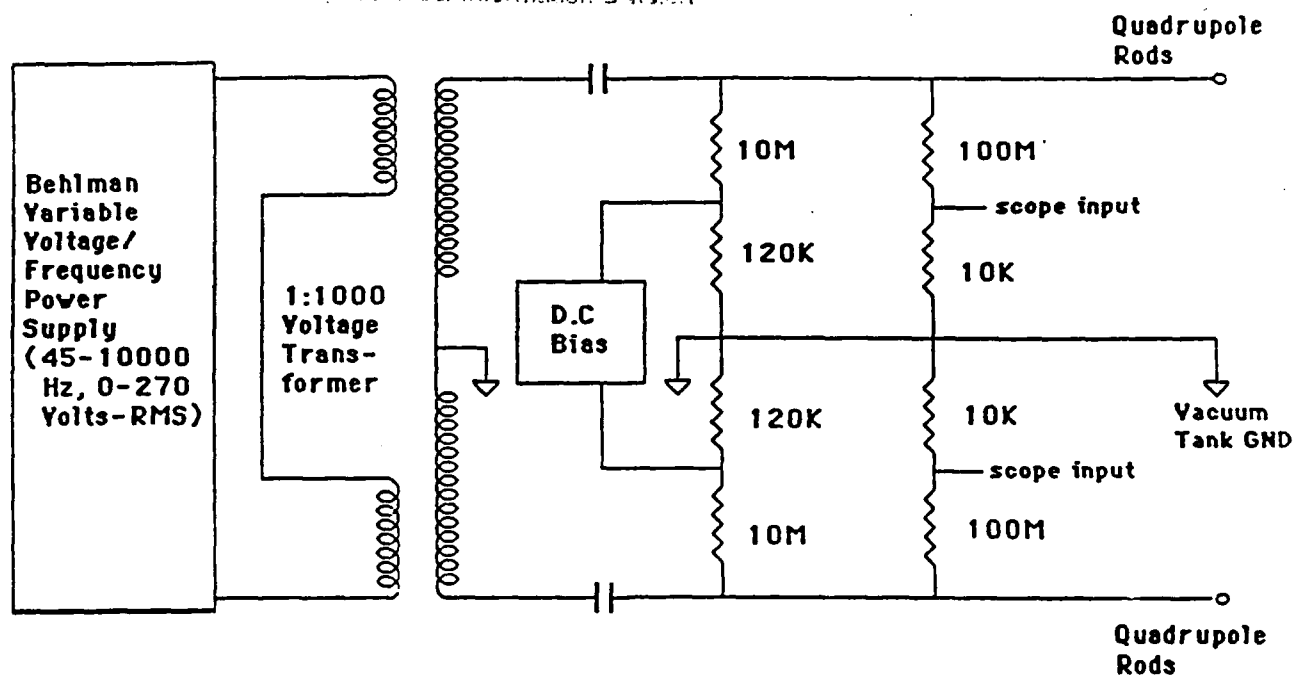


Figure C.3 Circuit Diagram for Voltage Amplifier